Bayesian Inference of Fundamental Physics at Extreme Conditions

by

John J. Ruby IV

Submitted in Partial Fulfillment of the

Requirements for the Degree

Doctor of Philosophy

Supervised by Professor Gilbert W. Collins and Professor J. Ryan Rygg

Department of Physics and Astronomy

School of Arts and Sciences

University of Rochester

Rochester, New York

2021

"If you know the way broadly you see it in all things."

-Miyamoto Musashi

"If all you have is a hammer, everything looks like a nail."

-Law of the instrument

Table of Contents

Biographical Sketch

The author is originally from Lake Ariel, Pennsylvania. He attended Villanova University, and graduated *cum laude* with a Bachelor of Science degree in Astrophysics and Planetary Science. As an undergraduate he worked as a research intern at the National Ignition Facility at Lawrence Livermore National Laboratory under the guidance or Dr. Arthur Pak. He began doctoral studies in Physics at the University of Rochester in 2016. He was supported by the Horton Fellowship at the Laboratory for Laser Energetics and received the Master of Arts degree from the University of Rochester. He pursued his research in High Energy Density Physics under the direction of Professors Gilbert W. Collins and J. Ryan Rygg.

The following publications were a result of work conducted during doctoral study:

First Author Publications

1. **J.J. Ruby**, J.R. Rygg, J.A. Gaffney, B. Bachmann, and G.W. Collins. A boundary condition for Guderley's converging shock problem. *Physics of Fluids*, 31(12), 2019

2. **J.J. Ruby**, J.R. Rygg, D.A. Chin, J.A. Gaffney, P.J. Adrian, D. Bishel, C.J. Forrest, V.Yu. Glebov, N.V. Kabadi, P.M. Nilson, Y. Ping, C. Stoeckl, and G.W. Collins. Constraining physical models at gigabar pressures. *Physical Review E*, 102(5):53210, 2020

3. **J.J. Ruby**, J.R. Rygg, D.A. Chin, J.A. Gaffney, P.J. Adrian, C.J. Forrest, V.Yu. Glebov, N.V. Kabadi, P.M. Nilson, Y. Ping, C. Stoeckl, and G.W. Collins. Energy Flow in Thin Shell Implosions and Explosions. *Physical*

Review Letters, 125(21):215001, 2020

4. **J.J. Ruby**, J.A. Gaffney, J.R. Rygg, Y. Ping, and G.W. Collins. High-energy-density-physics measurements in implosions using Bayesian inference. *Physics of Plasmas*, 032703(28), 2021

Co-Author Publications

1. F.J. Marshall, S.T. Ivancic, C. Mileham, P.M. Nilson, **J.J. Ruby**, C. Stoeckl, B.S. Scheiner, and M.J. Schmitt. High-Resolution X-Ray Radiography with Fresnel Zone Plates on the University of Rochester's OMEGA Laser Systems. *Review of Scientific Instruments*, 033701(92), 2021

2. B.J. Henderson, M.C. Marshall, T.R. Boehly, R. Paul, C.A. McCoy, S.X. Hu, D.N. Polsin, L.E. Crandall, M.F. Huff, D.A. Chin, **J.J. Ruby**, X. Gong, D.E. Fratanduono, J.H. Eggert, J.R. Rygg, and G.W. Collins. Shock-compressed silicon: Hugoniot and sound speed up to 2100 gpa. *Phys. Rev. B*, 103:094115, 2021

3. P. Hatfield, J.A. Gaffney, G.J. Anderson, S. Ali, L. Antonelli, S. Basegmez-du Pree, J. Cintrin, M. Fajardo, P. Knapp, B. Kettle, B. Kostowski, M. Macdonald, D. Mariscal, M. Matin, T. Nagayama, C. Palmer, J.L. Peterson, S. Rose, **J.J. Ruby**, C. Schneider, M. Streeter, W. Trickey, and B. Williams. The data-driven future of high energy density physics. *Nature*, in press, 2021

Acknowledgments

I have had the good fortune to receive unwavering support from a large number of individuals throughout my career to this point. Here I would like to acknowledge a few who stand out in particular but let it be known that there are many others who have had influence over my direction in addition to those named here.

I would like to start by thanking my father, John. J. Ruby III, mother Laura Ruby, and sister Hannah Price who have supported my pursuit of physics from the beginning and helped me navigate the academic system which was foreign to us all.

My research career began at Lawrence Livermore National Laboratory through a stroke of grace that led me to working with Dr. Arthur Pak, who not only introduced me to the field but guided me onto the path that led me to this point. Additionally I would like to thank Dr. Tammy Ma who has been one of my strongest advocates since my first day at Livermore.

In graduate school I have benefited from an abundance of freedom and resources to pursue interesting scientific problems and I owe most credit for that to my advisors Drs. Gilbert (Rip) W. Collins and J. Ryan Rygg both of whom have been overwhelmingly supportive of the directions I chose in my research and at the same time have pushed me to keep asking more of my research through their insightful questions. I would also like to thank the Laboratory for Laser Energetics (LLE) in general for their commitment to training graduate students and the overwhelming support from the laboratory at large. It is difficult to image

a better environment to pursue graduate research in high energy density physics than the LLE.

Within the LLE I have benefited from regular interactions with an excellent group of individuals and in particular I would like to thank Mr. Alex Chin, who always took time to discuss whatever scientific topic was on my mind at the time and helped me manage virtually all of my experimental campaigns, and Dr. Philip Nilson, who was always just as excited as I to push our conversations and work into new and creative directions.

I would also like to thank Drs. Yuan Ping and Jim Gaffney from Lawrence Livermore National Laboratory. Yuan has taken time to engage with me from the start of graduate school and has always supported my work with great fervor. Jim has been an invaluable resource and laid the foundations for much of the work that this thesis describes.

Finally I would like to thank Elizabeth who has been an enthusiastic and vocal supporter and has helped me keep growing as a person within and beyond science.

Abstract

Much of modern physics has been built on studying phenomena in isolated systems. These seemingly simple mechanisms, when applied to larger collection of system, become more complicated. The tools used to understand these systems were developed primarily at conditions relevant to the surface of the Earth and therefore comparison to experiments have been readily available. A similar addition of complexity exists when transitioning to extreme thermodynamic states. In these conditions, temperatures in the tens of thousands to many millions of Kelvin and densities from miligrams per cubic centimeter to kilograms per cubic centimeter, there exists complex collective behaviour that leads a wealth of interesting new phenomena not present in isolated atomic interaction or under standard thermodynamic conditions. These phenomena no doubt are critical to the evolution of astrophysical bodies, such as planets and stars. The modeling efforts have largely outpaced the experimental capabilities with regards to these systems at high energy density (HED, equivalently high pressure) and the laboratory landscape is moving towards measurements that are challenging to analyze independent of advanced modeling techniques. This work aims to present a systematic method for designing, executing, and analyzing HED experiments that enforces a self-consistent picture of the physics present in the system. This is done by creating a Bayesian inference framework, similar to those that exist in other fields of physics, that uses all relevant experimental data to constrain the integrated physicals model used to understand the experiments. The ultimate goal

is to move away from 'benchmarking' techniques and towards proper statistical constraint of the models used to describe physics under extreme conditions.

Contributors and Funding Sources

---

[1]This work was last updated: April 8, 2021

List of Tables

List of Figures

Chapter 1

Introduction

The goal of this thesis is to expand the use of modern statistical techniques in experimental high energy density physics (HEDP). Currently scientific research across many fields is jumping at the opportunity to use tools, which are not necessarily new, currently in vogue within the data science community. These tools, such as artificial neural networks (ANN) and other machine learning algorithms, have benefitted tremendously from the abundance of data available in modern society. Although machine learning tools are powerful, and have already produced some interesting results within HEDP, there is a less heralded but likely more powerful tool that has benefited just as much from the recent emphasis on large datasets.

Bayesian inference, or more broadly Bayesian statistics at large, is an old concept that has been rejuvenated in the last few decades. Bayesian inference techniques often get associated with machine learning techniques, although there is no strict connection between the two, likely due to similar demands with regards to computational power associated with both. Bayesian inference is a cornerstone of some fields of physics, most notable high energy physics (HEP), and provides a powerful framework that emphasizes not only measurements, but uncertainty associated with those measurements.

Measurements in HEDP are often challenging to make, singular in nature, and correlated with other unknown quantities, providing an almost ideal application
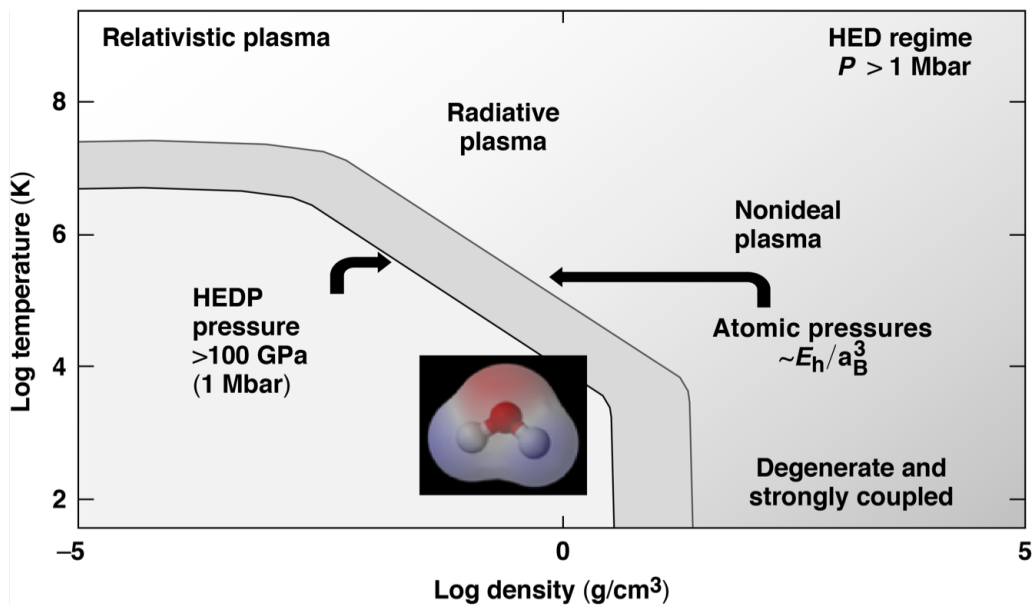
Figure 1.1: A temperature and density plot showing a number of relevant contours for HEDP, calculated for hydrogen, including isobars (black) corresponding to 1 Mbar and 300 Mbar, chemical and atomic energy densities respectively. Regions of temperature and density are subject to different physical phenomena, some of which are labelled here. Inset is a diatomic molecule (H_2O) representing the definition of high-energy-density, when thermal pressure is comparable to the energy density of molecular bonds (around 1 Mbar). Image used from [12].

for Bayesian inference. There are many practical difficulties with implementing the framework outlined within this text, many of which have been or are currently being addressed. Ultimately this work will stand as a starting point that (hopefully) will enable the wide-scale adoption of these methods within HEDP, providing a self-consistent, rigorous, and reproducible method for inferring fundamental physics quantities from HEDP experiments.

1.1   High Energy Density Physics

High energy density physics is defined as the subfield of physics that studies systems whose energy density is greater than 10^{11} J/m^3 such as those with thermal pressures of 10^{11} Pa or 1 Mbar[13]. For context, the energy of the covalent bond between Hydrogen and Oxygen is 462 kJ/mol and the volume of an H_2O molecule

is 3×10^{29} m^{-3}, giving an energy density of about 0.5 Mbar, so the beginning of high energy density physics can broadly be thought of as when the thermal energy pressures are comparable to chemical energy densities. At these conditions chemical changes, such as dissociation[14], and phase changes[15], become important.

At even larger pressures the atomic energy levels can be perturbed leading otherwise forbidden transitions[16] and ionization states that are not well described by the usual tools[17]. The primary focus of this work are systems that extend into and beyond these atomic pressures.

This introduction will provide a brief history of HEDP physics, not intended as an exhaustive overview but rather to present some relevant background for the current state of research, will discuss modern HEDP experimental facilities, how different experimental geometries can be used to access different pressure regimes, and finally a broad overview of analysis techniques in experimental HEDP.

1.1.1 Historical Development of HEDP

The 20th century saw many developments in modern physics that ultimately contributed to the creation of HEDP. The path can be traced to Arthur Eddington who discussed the internal structure of stars[18] in 1920 and made thermodynamic arguments, mostly based on the radiative properties of matter known at the time, to suggest that stars exist at very extreme thermodynamic conditions (much beyond solid density and above 10,000s K ; previously not considered in physics). These arguments were later developed even further by Subrahmanyan Chandrasekhar in his seminal text "An Introduction to the Study of Stellar Structure", originally published in 1939, in which he explicitly states 4 goals of the text[19]:

1. To derive the complete march of physical variables (the density,

ρ; the temperature, T; etc.), on the one hand, and the variation of the chemical composition (the relative abundances of the different elements), on the other, throughout the entire configuration.

2. To describe quantitatively the kind of steady state (radiative, convective, etc.) that exists, eventually as a function of the radius vector, r.

3. To specify the fundamental physics processes that are responsible for the setting-up of the steady states described under (2).

4. To evaluate quantitatively the irreversible processes that must be taking place which should be responsible for the continual loss of energy at the rate L by a star.

These goals necessitated an understanding of physics at extremely high energy densities and the field of stellar astrophysics can likely be considered the origin of thinking about these materials at these conditions.

Coincident with the developments in stellar structure, physicists were making significant progress in understanding nuclear reactions, and Eddington even proposed nuclear fusion as a way of producing the thermal states within a star[18]. In early 1939 Otto Frisch and Lise Meitner published two papers describing a new type of nuclear reaction, which they named nuclear fission[20, 21], based on work by Otto Hahn performed in late 1938. This discovery quickly spread and later in 1939 the possibility of nuclear chain reactions was confirmed with the discovery that Uranium fission produced 3.5 neutrons (later corrected to 2.6) per event[22]. The potential of neutron chain reactions was immediately evident, both for civilian purposes (energy reactors) and military (nuclear weapons).

Ultimately, amongst the backdrop of the second world war, this lead to the Manhattan project, which is well studied historically[23] and will not be recounted here. The most important point here is that during the testing of explosives during

the Manhattan project incredible thermodynamic conditions were created, and the first HEDP experiments were performed, the conditions were such that metals, formerly only considered as incompressible, were compressed causing scientists to reframe how they thought about materials[23]. Eventually the study of materials under extreme conditions lead to one of the primary HEDP sources, the book "Physics of shock waves and high-temperature hydrodynamic phenomena"[24], published in 1967.

Finally the last canonical driver of HEDP research is the pursuit of fusion energy through inertial confinement fusion experiments. In particular laser driven compression of materials for the purpose of fusion research, published in 1972 by John Nuckolls[25], opened to door to the modern landscape of HEDP. Although HEDP will always be tied to its application space in national security and energy research, it is valuable to remember the foundations of the field were laid by interest in fundamental studies of physical phenomena and mechanisms and this motivation holds true for many directions of modern research.

The development of HEDP discussed follows from considerations of the most extreme states, those necessary for thermonuclear fusion either terrestrial or astrophysical in nature, but there is another line of development, equally as important, but less heralded within the mythology of the US nuclear laboratories where much of the HEDP influence lives. These developments start by approaching HEDP conditions from the low end, rather than high end. The field of high pressure physics can be thought of as a precursor to high energy density physics (although the units of the two are the same, the details of the subfields are slightly different), which is its own unique field[26] although the line between HEDP and high pressure physics is increasingly blurry. High pressure physics was generally started by Percy Bridgman, who invented the first apparatus for compressing materials to high pressures and did so under static conditions[27]. These studies generally existed up to 10s of GPa (100s of kbars), short of the definition of HEDP but just

barely (and predating that definition by many decades).

Although some scientists working on the Manhattan project may have been surprised by metals being compressible[28], Bridgman and his students had been compressing metals for some time in his laboratory[27]. One of his students, Francis Birch, became well known for his work on the Manhattan project and then afterwards become even more well known for developing the standard model of Earth's interior[29]. High pressure physics is intimately related to planetary interiors in the same way that HEDP is intimately related to stellar interiors. The two fields overlap in the regime of the largest terrestrial and all manner of gas giants and brown dwarfs, where the condensed matter approach of high pressure physics and the plasma physics approach of HEDP are both used to understand the systems.

This is only a brief summary of historical context important for this thesis, more details can be found in numerous articles including information on more recent developments in HEDP, for example[26, 28].

1.1.2   Experimental Facilites
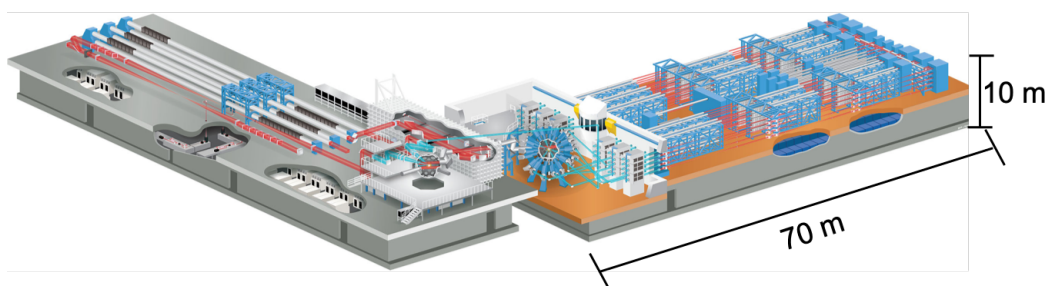
Figure 1.2: A representation of the Omega laser facility which includes the Omega-EP (left) and Omega60 (right) lasers. Omega-EP is built in a linear configuration with 4 beams all entering the target chamber from one side, while Omega60 is spherically symmetric with 60 beams oriented radially around the target chamber. Image used from [8].

The number of facilities exploring HEDP experimentally has grown consider-

ably over the last decade. The facilities range from large scale to tabletop and are too numerous to fully list, but can be placed into broad categories based on the long pulse lasers, that have nanosecond pulses and terawatts of power, short pulse lasers, that primarily using chirped pulse amplification to achieve picosecond or shorter pulses and reach petawatt powers, free electron lasers (FEL), which often are used in combination with a long pulse laser, magnetic compression devices, most well known in the Z-pinch architecture, light gas guns which launch impactors to drive pressure waves, and high explosive hutches which leverage chemical energy to increase the energy density of a subject. These facilities can be located on the university scale to the national laboratory scale and there is an increasing push for mid-scale university based user facilities.

This work will focus exclusively on experimental work performed at long-pulse laser facilities, and in particular at the Laboratory for Laser Energetics (LLE) located at the University of Rochester. The LLE has two large scale laser facilities, the Omega EP Laser[30], capable of both long-pulse and short-pulse operations predominantly in planar geometry, and the spherically configured Omega60 laser[31], a long pulse laser with a maximum of 30 kJ deliverable in ultraviolet light. The work presented here is based on experiments performed on the Omega60 laser.

1.2 Experimetnal Geometries

The Omega EP laser and Omega 60 laser both have unique advantages for performing HED experiments. As shown in Fig. 1.2 (left), Omega EP is oriented with each of the 4 laser beams approach the target from one-side of the target chamber giving preference to targets that have a planar geometry, that is targets with a flat edge where the laser is incident. Planar experiments are the most widely used within HED physics[15, 32, 33], due to the steadiness of pressure profiles able to
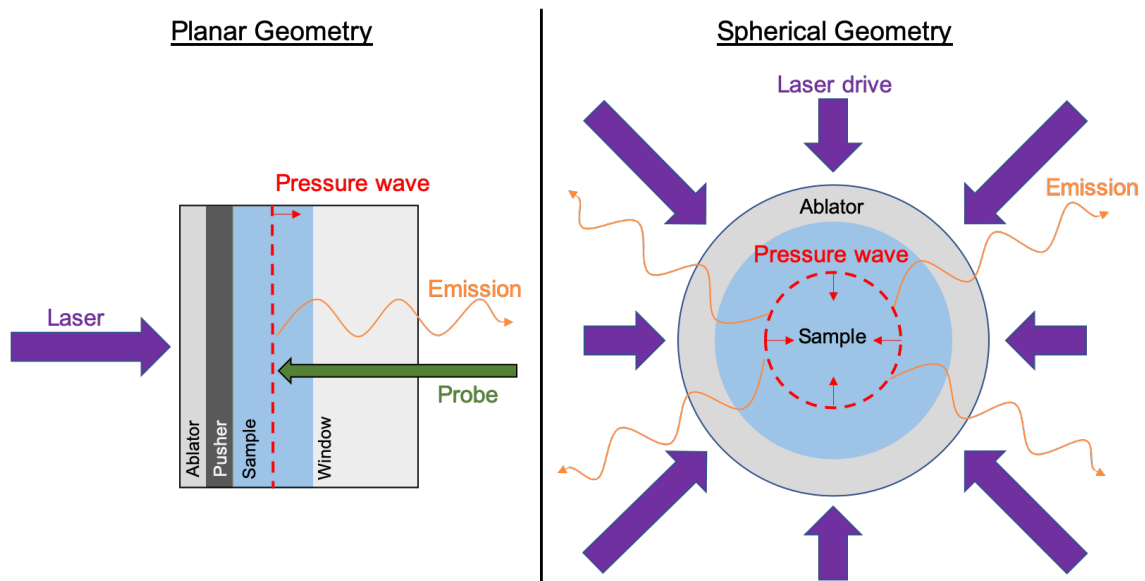
Figure 1.3: Sketches of a typical planar HED target (left) and a typical spherical HED target (right) for laser driven experiments. Within the planar target compressed material can be accessed through ambient material, but in the spherical target there is no point of access preventing the use of common probes.

be produced and the diagnostic access available.

The Omega60 laser, shown in Fig. 1.2 (right), has 60 laser beams oriented in a spherically symmetric geometry, primarily designed for performing ICF implosions. Spherical geometry allows for the highest energy densities to be produced by not only coupling energy to the target but also by decreasing the volume of the target. The trade-off for reaching higher pressures is the presence of gradients in both space and time within converging experiments along with diagnostic access since the states of interest exist within a plume of plasma, as will be discussed in Sec. 3.

Figure 1.3 shows a cartoon picture of planar (left) and spherical (right) laser driven targets, typical of HED experiments on the Omega laser system. Common factors between both targets are an ablator, which the laser is incident on, ejecting mass and launching a pressure wave, and the sample, which is the material that is under study. The planar target has two additional components, a 'pusher' that helps with matching impedance between the target and the ablator, and a

'window' which inertially tamps the sample material and also is able to transmit radiation for measurement (generally visible spectrum). An important aspect of planar targets is that the measurements occur through uncompressed material. Material that is at HED conditions is generally very difficult to probe, due to unknown optical properties and states that do not transmit visible light. In the planar case this is not a concern because the measured probe and/or emission only travels through well-characterized ambient material, while in the spherical case any measured emission necessarily must travel through already compressed material, with unknown properties, in order to escape the target. Additionally, common probes are unable to access the interior of the spherical target preventing the same measurement techniques from being applied.

Spherical HED targets, the focus of this thesis, require a unique approach for making quantitative physics measurements.

1.3 Common Diagnostics

There are a wide variety of diagnostics used in HED experiments, with some key differences between planar and spherical configurations. Planar experiments make great use of optical diagnostics, in particular the velocity interferometer for any reflector (VISAR)[34] and streaked optical pyrometers (SOP)[35]. These two diagnostics are used to measure pressure waves launched in planar targets, VISAR through a probe laser that reflects off the target and is able to measure velocities (green arrow in Fig. 1.3), and SOP by collecting the thermal emission coming from the pressure wave (usually a shock wave). Both diagnostics are streaked in time and provide 1-D spatial resolution.

Optical diagnostics have much less utility in diagnosing the compressed inner material in the spherical case where the measurement techniques are much closer to those found in observational astronomy[36]. The spherical targets usually hot-

ter and denser than the planar case and the primary quantities that are measured are self-emission in the form of x-ray emission (because less energetic emission is unable to escape the target) and energetic particles that are the result of thermonuclear reactions. There are a wide variety of diagnostics commonly used in these experiments[37], but are usually design to measure either particles or x-rays. Within each of these categories there are diagnostics that discriminate spectrally, spatially, and temporally, or some combination of the three. For example, a commonly used diagnostic in this work is an x-ray pinhole camera, which is simply a pinhole, usually around 10 μm in size, drilled into an opaque (to x-rays) substrate, such as Tantalum, that is able to image the x-ray self-emission from the target. This emission is collected on either an image plate, x-ray film, or using an x-ray framing camera[38] that provides temporal gating.

Techniques and diagnostics common to both astronomy[36] and HED[37] diagnostics include x-ray crystal spectrometers, x-ray optics such as Fresnel Zone plates and Kirkpatrick Baez microscopes, micro-channel plates, and scintillators. When considering measurements and analysis techniques in HEDP it is valuable to remember this connection to observation astronomy to benefit from progress in instrumentation and software from across the fields.

1.4   Analysis Methods

HEDP is a broad field, with many different measurements and analysis techniques. Here measurements are categorized into 3 distinct groups given as subsections herein. The primary motivation for this work stems from the complexity of HEDP experiments and the quality of instruments often outpacing the developments in the analysis techniques of these measurements, which often lead to inconsistent conclusions and under-predicted uncertainty. There is a richness of information within HEDP measurements waiting to be accessed through analysis techniques.

1.4.1   Direct Measurement

The most obvious, and likely most satisfying, measurement that can be made is a direct measurement of a quantity of interest (QOI), for example if the temperature of some system is of interest in most cases a thermometer can be used to directly measure it but the spatial scales, of order tens of microns, and temporal scales, of order tens of picoseconds, in combination with the extreme temperatures and densities preclude the use most common instruments designed to measure physical properties[1].

Despite the extreme states and scales present there are a number of instruments that routinely measure a QOI directly (or as directly as possible i.e. through a well vetted and tested model). Usually these measurements happen in planar geometry due to the access available through ambient material. The instrument likely most well-known and commonly used in planar HED studies is known as a velocity interferometer for any reflector (VISAR)[34] which uses a probe laser (532nm at the Omega Laser Facility) to set up an interferogram where one leg reflects off of a surface in the target. The result is a series of fringes, which are streaked in time, that move in response to changes in position (velocity). The surfaces that are measured are either a shock wave or some reflective surface in the target such as a metallic layer which in turn result in measurements of shock velocity or a particle velocity within the driven material, both of which are a QOI when considering the material studies as they relate to the equation of state through the Hugoniot equations.

Another example commonly used in planar HED experiments is x-ray diffraction for the determination of crystal structure[39]. In this case a sample material is

---

[1]Clearly, a thermometer doesn't directly measure temperature but rather depends on other physical processes that couple to the temperature in a system in a known way, for example via the expansion of mercury. The point here is that thermometers are well calibrated, verified and give consistent, reproducible, and unambiguous answers. These traits are exceedingly rare when dealing with systems at extremes.

compressed and another laser is used to produce a bright x-ray source, by hitting a metal foil and exciting atomic transitions, which passes through the target and is diffracted according to Bragg's law resulting in a unique pattern when they are recorded that can be used to determine the crystallographic nature of the sample.

These are likely the two best examples of direct measurements of QOI in HEDP and in combination have lead to many high profile results (for example [15, 40]). This work focuses solely on spherical geometry, and in regimes where these diagnostics are not typically appropriate, but they are discussed here for context with regards to the measurements possible within the range of HEDP experiments.

1.4.2   Inversion

Inverse problems are a way to think about scientific measurements and analysis and is generally in tune with intuition. The measurements described in Sec. 1.4.1 can technically be characterized as inverse problems at their core, but have been established to not suffer from the issues inherent in inverse problems and therefore have been accepted as direct measurements of QOI.

The example of a thermometer can be used to demonstrate the form of an inversion problem that is well defined. Thermometers consist of a rigid tube (generally glass) with a fixed volume that contains some liquid (such as mercury) with well characterized properties. In particular the way the volume of the liquid increases as a function of temperature, the volumetric expansion coefficient (α_V), must be known. Assuming that α_V does not change as a function of temperature (in the range of temperatures that are of interest), the equation relating the change of volume and change in temperature can be written as

$$\frac{\Delta V}{V} = \alpha_V \Delta T \tag{1.1}$$

where V is the volume, ΔV is the change in Volume, and ΔT is the change in

temperature.

The thermometer really measures changes in Volume, but the QOI is temperature, resulting in an inverse problem. In this case the problem is trivial, inverting Eq. 1.1 is simple algebra to get

$$\Delta T = \alpha_V^{-1} \frac{\Delta V}{V} \tag{1.2}$$

and it is seen that the temperature changes linearly with the fractional change in volume with the inverse of α_V being the rate at which it changes. This result (along with α_V being independent of T) allows the temperature lines on a glass liquid-metal thermometer to be drawn at regular intervals, a seemingly simple result but one that has deep consequences for measurements.

The most important part of this is that there is a one-to-one mapping between temperature and change in volume, likewise similar mappings exist for the measurements described in Sec. 1.4.1, such as between a diffraction pattern and a crystal orientation or between VISAR fringe shifts and magnitude of velocity [2]. In this case dealing with uncertainty is very straight forward and the classical error propagation methods taught in introductory courses is sufficient.

Now consider the case where there is a more complicated relationship between volume and temperature, in particular the case where $\alpha_V = \alpha_V(T)$. In this case the differential form of Eq. 1.1 must be considered

$$\frac{dV}{V} = \frac{\alpha_V}{dT} \tag{1.3}$$

---

[2]There are exceptions to these statements and ambiguity can occur in both measurements, but in general there are regimes where both x-ray diffraction and VISAR measurements have been demonstrated to consistently reproduce un-ambiguous measurements.

which, integrating both sides, gives the equation

$$\ln\left(1 + \frac{\Delta V}{V}\right) = \int_{T_i}^{T_f} \alpha_V(T) dT. \tag{1.4}$$

Solving for the temperature given the change in volume (assuming a known α_V) now requires inverting an integral equation and very quickly numerical methods or simplifying assumptions must be used to find the temperature, depending on the complexity of the form of $\alpha_V(T)$, the range of temperatures under study, and the accuracy with which $\alpha_V(T)$ is known. As problems increase in complexity the assumptions that must be made to accommodate inversion become cumbersome and often lead to a severe under-prediction of uncertainties [41], not to mention that when inverting multiple quantities from an experiment it is not always trivial to evaluate the self-consistency of the assumptions that went into the analysis.

Inverse problems are well studied in many fields of science and applied mathematics, for example the field of tomography has a rich literature discussing these issues [42]. Tomographic reconstrucitons are also of interest in HEDP since x-ray radiographs are a way to probe convergent HEDP systems. Modern research has given preference to forward modeling techniques for radiographic reconstructions, in [43, 44] and out [42, 45] of HEDP . Forward modeling in general is discussed in the following Sec. 1.4.3.

1.4.3   Forward Modeling

Forward modeling describes a general way of solving inference problems, such as the thermometer example in Sec. 1.4.2 where temperature is inferred from a change in volume. Rather than inverting Eq. 1.1 to solve for the temperature, a forward modeling technique would be to guess a temperature, calculate what the change in volume would be for that temperature, compare it to the observed change in volume, and iterate, changing the guess temperature, until a temperature is

found that matches the observed change in volume. In this simple example making use of forward modeling is superfluous, but without much added complexity the power of the technique becomes obvious.

Consider the inference of temperature from Eq. 1.4, where the expansion coefficient is a function of temperature. In this case solving by inversion involves dealing with an integral operator, which may not be invertible at all depending on the form of $\alpha_V(T)$, but a forward modeling technique would simply guess values of T_f (assuming a known starting temperature, T_i) and perform the integral, likely numerically, resulting in a value for the change in volume. Again, this process repeats until the value of T_f is found. This process has many advantages, including 1) explicit statement of the model being used to infer quantities from the system and 2) it is much more robust against noisy measurements, especially when dealing with integral operators.
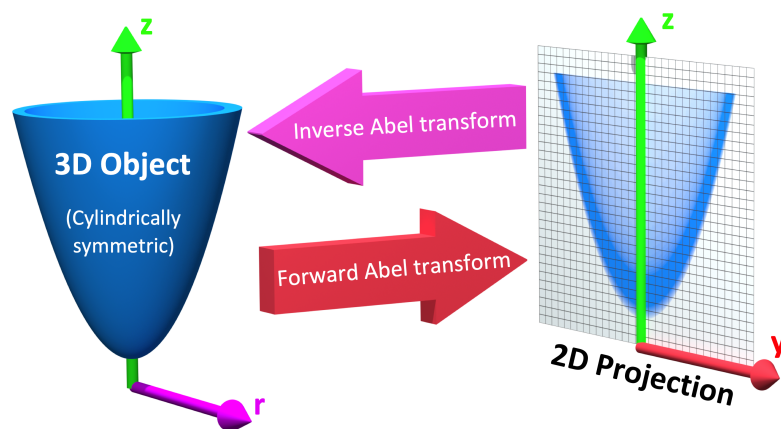
Figure 1.4: An example of a tomographic projection. A 3-D object is projected onto a 2-D plane, and in the case of radially symmetric objects this process is described mathematically by the forward and inverse Abel transforms. Image used from the documentation of the PyAbel package[9]

Returning to the example of tomographic measurements, Fig. 1.4 shows an example of a typical tomographic measurement. The left-hand side shows a 3-D distribution in space which is projected onto a 2-D space, this analogous to what occurs when an x-ray image is taken where x-rays travel through an object, such as

a limb, are partially absorbed, for example by bone, and then are imaged onto a flat detector, resulting in a 2-D projection of the object. In the example of Fig. 1.4 the 3-D object is radially symmetric, so projection can be described mathematically by an Abel transform, which is an integral operator that is invertible via the inverse Able transform. If the 2-D projection is measured but information is desired about the 3-D object, the inverse Abel transform can be applied, or forward modeling can be used to guess at the 3-D distribution, forward Abel transform it, and check against the observed 2-D projection.

In principle inverting the 2-D projection would be preferable but is subject to practical limitations. The Abel transform assumes radial symmetry, so the inverted distribution will always be radially symmetric with no way to test validity, i.e. the inversion technique will give a (likely reasonable) answer regardless of whether the assumption is appropriate or not. Additionally, in the presence of noise the inverse transform compounds the noisy signal leading to many artifacts in the inverted distribution [46].

Forward modeling does not suffer from these two short comings. In the event that the real 3-D distribution is not radially symmetric, forward modeling symmetric distributions will result in 2-D projections that are unable to reproduce the observed projection, which indicates a model with great complexity should be used. Additionally, forward modeling avoids the issue of operating on noisy data and even allows noise to be explicitly modeled.

Forward modeling techniques have long been present in the physical sciences but their widespread use can be traced back to the advent of information theory [10] that also coincided with the development of numerical solving machines that eventually would turn into computers. Figure 1.5 (a) is a reproduction from Shannon's paper that spawned the field of information theory, and presents a simple forward model for understanding how signals are produced. The key problem was: how can a sent message be reconstructed from a received message that is subject
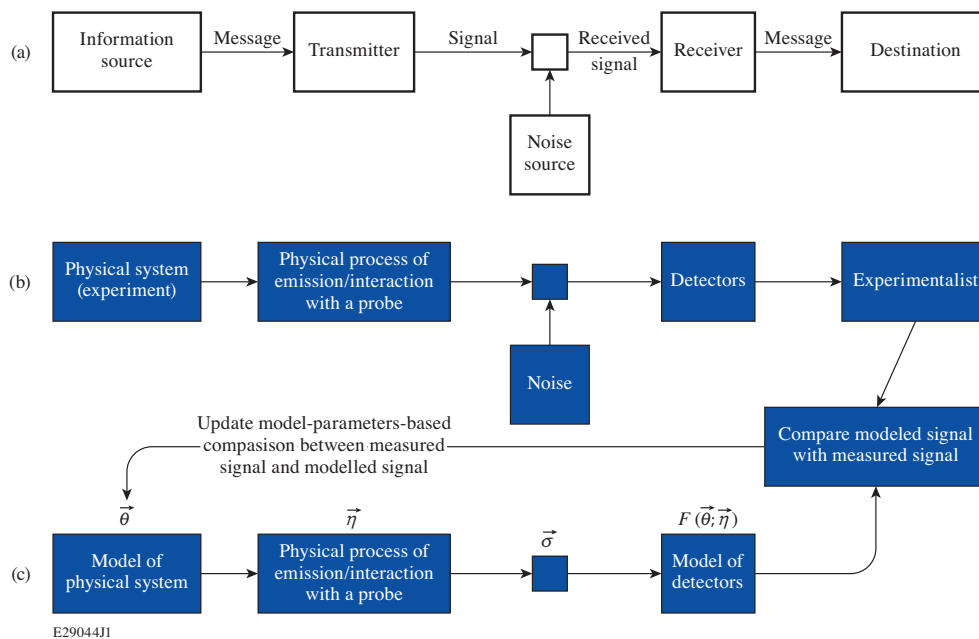
Figure 1.5: A reproduction of a figure from Shannon's paper on information theory[10] (a), a recasting of this into the context of experimental physics (b), and how forward modelling can be used to reconstruct a message(c). Discussed more in the text and in Ref. [2].

to both transmitter and receiver distortion and an external noise source. This can be recast to a system of physical measurement, as shown in Fig. 1.5 (b) where the information source is a physical system and the received signal is a detector observation. Figure 1.5 (c) demonstrates how a forward technique can be used to reconstruct the details of the physical system.

There are many benefits to forward modeling, but there are challenges inherent, the most obvious of which is how to properly iterate on guesses. This poses an optimization problem that is potentially high dimensional and therefore potentially computationally intensive, depending on what the model looks like, and is still a topic of modern research. The remaining part of this thesis will address the practical implications of using a forward modeling scheme to understand the HEDP experiments and in particular how the combination of forward modeling and Bayesian inference (the topic of Ch. 2) is a powerful tool for understanding HEDP systems.

Chapter 2

Bayesian Inference Background

Bayesian methods in statistics is a well developed field, which is often covered in advanced analysis and statistics classes. Despite this, there are practical limitations to implementation that have prevented its use in many areas of physics, including high energy density physics (HEDP). While some fields of physics have fully embraced Bayesian methods [47], such as high energy physics and cosmology [48], the historical inertia of other methods likely limits usage within HEDP. This chapter provides an introduction to Bayesian methods and particular examples with a discussion surrounding their use within HEDP. More general introduction to the concepts can be found in many textbooks, in particular a very useful practitioners guide by Sivia [49] and an extremely thorough derivation of the field by Jaynes [50].

This chapter will introduce some terminology and notations, discuss some different kind of Monte Carlo sampling methods, and present some comments on the practical implementation of Bayesian methods in HEDP.

2.1 Basic Bayesian terminology

Bayesian statistics has a few key concepts that are critical to applying it to HEDP experiments, and many concepts that are actively studied and under development; This work is not a conclusive overview nor will it answer all outstanding questions.

Table 2.1: Common terms and definitions found in Bayesian inference. $p(X|Y)$ represents the probability density distribution of X given that Y is true.

Term	Mathematical Formulation	Description
Model	M or F	Model of physical system
Data	D or $\vec{Y}$	Observed data
Model Parameter	$\vec{\theta}$	Parameters in the model
Parameter Posterior Distribution	$p(\vec{\theta}|D, M) = \frac{p(D|\vec{\theta},M)p(\vec{\theta}|M)}{p(D|M)}$ $p(\theta_i|D, M) = \int d\theta_{j \neq i} \; p(\vec{\theta}|D, M)$	Probability density distribution of parameters given data
Likelihood	$p(D|\theta_i, M)$ or L	Probability density of observed data given a model and set of parameters
Parameter Prior Distribution	$p(\theta_i|M)$	Represents initial information about the parameter
Model Posterior	$p(M_1|D) = \frac{p(D|M_1)p(M_1)}{p(D)}$ given observed data	Probability density of model
Marginal Likelihood	$p(D|M_k) = \int d\vec{\theta} \; p(D|\vec{\theta}, M_k) \; p(\vec{\theta}|M_k)$	Probability of observed data given a model integrating over parameter distributions
Bayes Factor	$B = \frac{p(D|M_1)}{p(D|M_2)}$	Model comparison metric Assumes $p(M_1) = p(M_2)$

This work is a gateway into the rich literature of Bayesian statistics and to provide a starting point for scientists, and specifically experimentalists, working in HEDP to start using the these tools.

A critical first step is establishing the language and definitions used within this work and the Bayesian community at large. A set of quantities, definitions, and common variables used to describe these quantities is given in table 2.1. In Bayesian statistics all quantities are treated as random variables with probability distributions that become more narrow as certainty increases. In the limit of total knowledge about a parameter the probability distribution will converge to a delta-function. In practice there is always some range of certainty over which a quantity is known and this is called a credible-interval. Within this work if a credible interval is given as, for example, 75% the interpretation should be that if an identical measurement were made there is an expectation that 75% of the

time it would fall within the given interval. This should be contrasted with the confidence intervals of classical statistics which are interpreted as there being a 75% chance that the true value of the parameter is within the interval. Within Bayesian statistics the concept of a true value is not considered but rather what degree of belief was gained through a measurement, i.e. what information was gained by making the measurement.

The primary equation of interest is Bayes' theorem, given as

$$p(\vec{\theta}|\vec{Y}, F) = \frac{p(\vec{Y}|\vec{\theta}, F)p(\vec{\theta}|F)}{p(\vec{Y}|F)} \tag{2.1}$$

where $p(X|Y)$ notation represents the probability density distribution[1] of X given that Y is true, $\vec{\theta}$ is a set of parameters, $\vec{Y}$ is a set of observations, and F is a model. It is important to understand this equation in terms of Fig. 1.5 and the discussion of forward modeling in Sec. 1.4.3. This framework requires a model, F, that takes the parameters of interest $\vec{\theta}$ and returns a prediction for observed quantities, $\vec{Y}$,

$$F(\vec{\theta}) = \vec{Y}_{model} \tag{2.2}$$

which can then be compared to the observed data $\vec{Y}_{obs}$, meaning that Bayesian inference inherently requires problems to be formulated in a forward modeling way.

Ultimately the desired quantity from Eq. 2.1 is $p(\vec{\theta}|\vec{Y}_{obs}, F)$ which is called the posterior probability distribution of $\vec{\theta}$, known simply as the posterior. This quantity describes the probability of the parameters in $\vec{\theta}$ being certain values, based on the chosen model and the observed data. According to Eq. 2.1 the posterior depends on 3 quantities, the likelihood function, $p(\vec{Y}_{obs}|\vec{\theta}, F)$, the prior

---

[1] The quantites of interest in HEDP are general continuous variables, as opposed to discrete, meaning that the formulation of Bayes' theorem includes probability densities rather than strictly probabilities. An implication of this is that there is an integral implied on the right-hand side of Eq. 2.1 in the denominator over all parameters.

parameter distributions, $p(\vec{\theta}|F)$, known as priors, and the marginal-likelihood or evidence, $p(\vec{Y}_{obs}|F)$.

The likelihood function is related to the probability of measuring the observed data, assuming the model, F, and parameter values $\vec{\theta}$. This function can take many forms that generally depends on the nature of the errors associated with measurements. As an example, imagine the thermometer example from Sec. 1.4 and Eq. 1.1 which gives the change in volume as a function of change in temperature and the volumetric expansion coefficient. In this case the model, F, is Eq. 1.1, the parameters are $\vec{\theta} = [\alpha_V, \Delta T]$, and the observation is $\vec{Y}_{obs} = \frac{\Delta V}{V}$. So given a measurement of $\frac{\Delta V}{V}$ with some error the likelihood of that measurement can be calculated[2] assuming fixed values for α_V and ΔT. Assume that the fractional change in volume was measured to be $\frac{\Delta V}{V}_{obs} = 0.020 \pm 0.001$ where the error on the measurement is normally distributed and has a standard deviation of 0.001. Now assume that $\Delta T = 100K$ and $\alpha_V = 1.8 \times 10^{-4} K^{-1}$ which, using Eq. 1.1, would give $\frac{\Delta V}{V}_{model} = 0.018$. In order to evaluate the likelihood of the measurement, given the model, we consider the distribution implied by the measurement, a Gaussian random variable with mean 0.02 and standard deviation 0.001, and evaluate

$$
p\left(\frac{\Delta V}{V}_{obs} = 0.020 \pm 0.001 | \Delta T = 100K, \alpha_V = 1.8 \times 10^{-4} K^{-1}; Eq.1.1\right) =
$$
$$
L = \frac{1}{0.001\sqrt{(2\pi)}} e^{-\frac{(0.020-0.018)^2}{2(0.001)^2}} = 54.0.
$$
(2.3)

The likelihood function is not very intuitive but can be used to construct the posterior, using Eq. 2.1, requiring sampling the likelihood over a range of parameter values, and is usually done numerically as discussed in Sec. 2.2

---

[2] Note that this 'feels' backwards, the quantity of interest is change in temperature but we are calculating the likelihood of change in volume. This is common in Bayesian inference because the evaluation is of the likelihood of seeing a particular observation, assuming the model is correct. In this case the model is Eq. 1.1 and values for α_V and ΔT which give an expectation for what $\frac{\Delta V}{V}$ is, if this expectation is wildly off from what was observed the model must be updated, likely by changing the values of either ΔT or α_V.

The next term in Bayes' theorem, the prior, is a way to leverage previous, or prior, knowledge about the parameters of the model. The priors are probability density distributions and can take any form. Using the change in temperature as an example perhaps it is known that the temperature being measured increased so $\Delta T > 0$. To leverage this information the prior on the variable ΔT would be a uniform distribution on the range $[0, T_{max}]$, where T_{max} is some large value that bounds the upper end of physically reasonable temperatures[3]. The more information about a parameter that exists, the more peaked the prior distribution. Imagine there are well known measurements for α_V that give its value to be $\alpha_V = 1.80 \times 10^{-4} \pm 1.0 \times 10^{-6} K^{-1}$; an appropriate prior in this case would be a normal distribution with mean 1.80×10^{-4} and standard deviation 1.0×10^{-6}. The effect of this is basically fixing α_V to that value, unless there is overwhelming evidence from the measurements to the contrary. In the case of the thermometer the ΔT is unknown and α_V is highly informed, so the data will predominantly inform what the value of ΔT is. The use of priors in Bayesian inference is sometimes a point of contention, due to the effect they have on the results on an analysis but prior information is leveraged no matter the form of analysis, Bayesian inference makes it quantitative and explicit which should be seen as an advantage not a disadvantage. Additionally, by using appropriate priors, systems that are otherwise ill-constrained, i.e. models with more parameters than there are measurements, can potentially be constrained using relevant prior information.

Finally the last term in Bayes' theorem is the marginal likelihood, which appears as a normalization constant within the equation to ensure the posterior is properly normalized (probability density distributions must integrate to unity). Beyond this the marginal likelihood is useful for model comparisons but is generally difficult to calculate [49]. The majority of this work focuses on parameter

---

[3]It is important that priors are on closed intervals (or atleast the integral over the prior converges) because they must be integrable to satisfy the mathematical derivations that go into Bayes' theorem.

estimation, which does not explicitly require the computation of the marginal likelihood, so it will not be discussed in too much depth.

2.2 Solving Bayes' Theorem

The primary concern of this thesis revolves around parameter inference, which means constructing the posterior distributions for all parameters of a given model. This is precisely what Bayes' theorem, as presented in Eq. 2.1, is designed for, but when only the parameter inference is desired the marginal likelihood does not need to be constructed because it is the shape of the distributions that are of interest and they do not necessarily need to be normalized.

In principle if the likelihood is known and the priors are known the posterior is a simple multiplication of the two distributions but in practice the likelihood is an N-dimensional (where N is the number of model parameters) surface that has some complicated shape. Once more than 2 or 3 parameters are introduced it becomes computationally prohibitive to construct most likelihoods so more sophisticated techniques are necessary. This is where the use of Monte Carlo methods are introduced into Bayesian inference as a way to construct the likelihood (and therefore the posterior) by sampling the surface only in areas of high probability density to ensure important regions are well resolved and computational time is not wasted on unimportant parts of parameter space.

This section will demonstrate the direct calculation of a posterior as an example and will then discuss two different Monte Carlo sampling algorithms, the set of Markov Chain Monte Carlo techniques which are by far the most common, and Sequential Monte Carlo techniques (also known as particle filters) which are uniquely suited to many of the problems faced in HEDP.

2.2.1 Direct Calculation
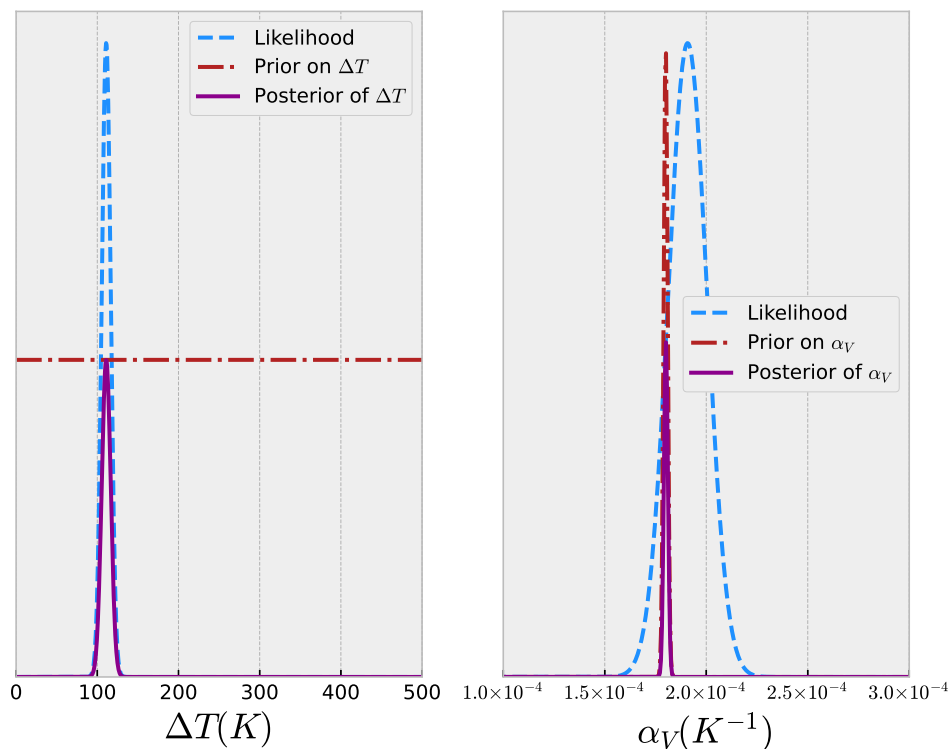
Figure 2.1: The likelihood (blue dashed line), prior (red dotted-dashed line) and posterior (purple solid line) for the 1-D inference examples of a fixed α_V (left) and fixed ΔT (right). The posterior is the product of the likelihood and the prior.

The direct calculation of the (unnormalized) posterior is as simple as multiplying the likelihood function by the priors along each dimension (determined by the parameters of the model). Although this is simple, it has limited utility since the distributions are not often analytic, though, the next simplest opportunity is a brute force numerical calculation.

Practically, a direct calculation is the simplest numerical way to perform Bayesian inference and compute the posterior of model parameters. This involves numerically constructing the likelihood and prior distributions gridded finely enough to capture their true shapes. Using the thermometer example from previous sections, if only one parameter is a variable and the other is fixed at some value the prior on the free variable, likelihood, and posterior are all 1-D and can be

easily compared, shown in Fig. 2.1. On the left the case with a variable temperature is shown and on the right the case with a variable expansion coefficient. A Gaussian likelihood (blue dashed line) is used, $L \propto exp(\frac{-(Y_{obs}-\Delta T \alpha_V)^2}{2\sigma_{obs}^2})$, as evident in the figure. Two different prior distributions (red dotted-dashed line) are shown, in the case of the variable temperature a uniform prior over 0 to 500 Kelvin is used and in the case of the variable expansion coefficient a narrow Gaussian prior is used with $\mu = 1.18 \times 10^{-4} \mathrm{K}^{-1}$ and $\sigma = 1.0 \times 10^{-6} \mathrm{K}^{-1}$. Calculating the posterior (purple solid line) requires sampling the likelihood and priors over the same values and multiplying them together, for example in python using numpy arrays this looks like:

```
"""
Example code for direct calculation of
posterior in the fixed expansion coefficient case.
"""
from numpy import linspace,exp,ones_like
#Set the value of the expansion coefficient
alpha_V = 1.18E-4
#Make grid of temperature values to calculate over
delta_T = linspace(0,500,500)
#Set values of observed change in Volume and the error on measuement
Y_obs = 0.02
sigma = 0.001
#Construct the Gaussian likelihood using the temperature array
likelihood = exp(-(Y_obs - alpha_V*delta_T)**2/(2*sigma**2))
#Uniform prior on T has same value over whole interval
prior_T = ones_like(delta_T)
#Calculate the posterior by multiplying prior and likelihood
unnormalized_posterior_T = likelihood*prior_T
```

Now consider the case where both ΔT and α_V are random variables, with the same priors given in Fig. 2.1[4]. In this situation the likelihood is now a 2-D distribution that depends on both variables, the calcuations are not much different other than handling the likelihood as an [N x M] matrix where N and M are the number of points ΔT and α_V are sampled at, respectively.

Figure 2.2 shows the likelihood function (left) that results from measured values given above but now across both variables. Since the change in volume is given

---

[4]All distributions shown in figures are unnormalized so the height on the vertical axis is not meaningful. Normalization follows from ensuring the probability density distributions integrate to unity.
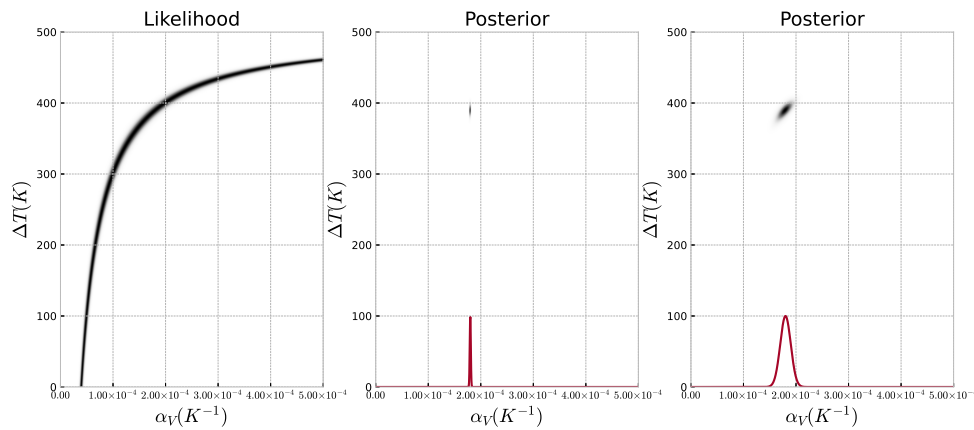
Figure 2.2: The 2-D likelihood (left) and posteriors for different priors on α_V (middle and right). The priors for α_V (red solid lines) are shown on with the posteriors. The dark shading corresponds to regions of high probability density.

by the product of ΔT and α_V there are many combinations that give values in agreement with the observations (shown by the dark band Fig. 2.2). This is where prior information becomes necessary to infer distributions for the variables. In the middle panel of Fig. 2.2 the posterior that results from multiplying the likelihood by the priors given in Fig. 2.1 (with the α_V prior shown for reference) is shown. The dark color in this case corresponds to regions of high probability density and is isolated to a very narrow set of α_V values, set by the prior, which also establishes a narrow range of ΔT values that still agree with the measurements.

The right-most column in Fig. 2.2 shows the same process but now with a prior on α_V that is 10 times larger than the other example. This produces a posterior with a larger range of acceptable values and the correlation between the two parameters is clear by observing the slope of the ellipse that is created. Increased uncertainty in α_V leads to increased uncertainty in ΔT, as expected.

Since the distribution of ΔT is the quantity of interest the effects of α_V can be marginalized to produce 1-D posterior distributions for ΔT. This process is simply integrating the 2-D posterior along the α_V axis and the results are shown in Fig. 2.3 for the 2 priors on α_V given above and compares the results to the 1-D inference with a fixed value for α_V. In the case of the narrow prior (Fig. 2.3
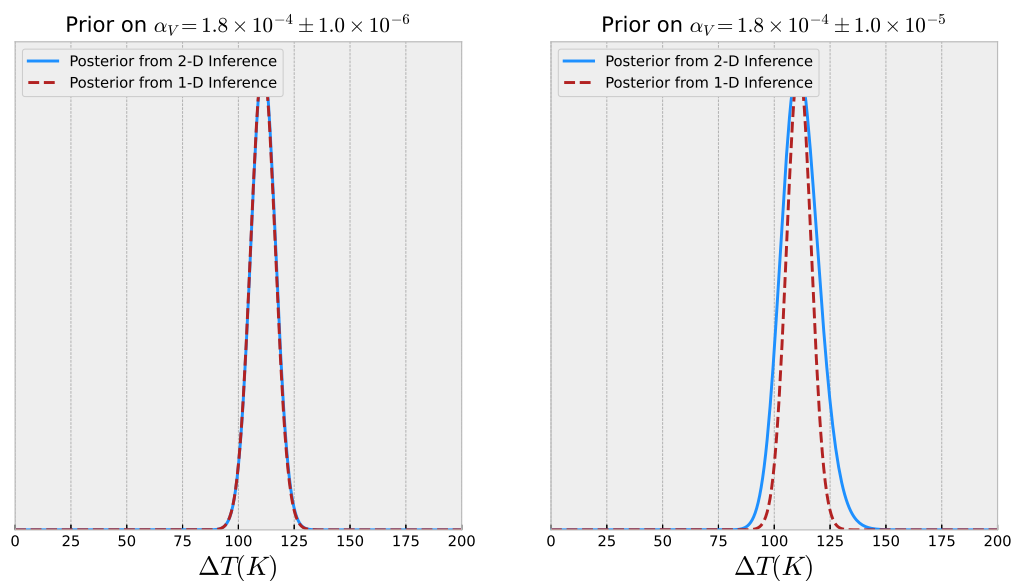
Figure 2.3: The marginalized 2-D posterior distributions for ΔT (blue solid lines) compared to the 1-D posteriors with a fixed value for α_V (red dashed lines) for the case of a narrow (left) and broad (right) prior on α_V

left) the 1-D and 2-D inference give virtually identical posteriors for ΔT but when the uncertainty in α_V is larger (Fig. 2.3 right) it leads to a broader posterior distribution in the temperature.

The fact that uncertainty in one parameter of a model leads to increased uncertainty in another correlated parameter is far from novel and is clearly not unique to Bayesian inference, but, despite its seemingly obvious nature, the effect is often over-looked in HEDP analysis due to the complexity of the models used to evaluate observations. Often parameters that should be treated as random variables are over-looked leading to over-confidence in inferred quantities. Bayesian inference helps to solve this problem by forcing the user to explicitly state the model and prior assumptions on the parameters. The python code example of how to do the direct calculation in the 2-D case is as follows:

```python
"""
Example code for direct calculation of
posterior in the 2-D case with narrow alpha prior.
"""
from numpy import linspace,exp,ones_like,meshgrid,expand_dims
#Make grid of temperature and alpha values to calculate over
delta_T = linspace(0,500,500)
alpha_V = linspace(0,5E-4,1000)
#Set values of observed change in Volume and the error on measurement
Y_obs = 0.02
sigma = 0.001
#Set prior mean and std for alpha
mu_alpha=1.18E-4
std_alpha=1.0E-6
#Create a meshgrid of temperature and alpha values
alpha_mesh, delta_T_mesh = meshgrid(alpha,delta_T)
#Construct the Gaussian likelihood using the mesh
likelihood = exp(-(Y_obs - alpha_mesh*delta_T_mesh)**2/(2*sigma**2))
#Uniform prior on T and Normal prior on alpha
prior_T = ones_like(delta_T)
prior_alpha = exp(-(mu_alpha - alpha_V)**2/(2*std_alpha**2))
#Calculate the posterior by multiplying prior and likelihood
unnormalized_posterior_2d = likelihood*prior_alpha*expand_dims(prior_T,axis=-1)
```

An important point to note is now the likelihood is a [500x1000] array containing $500 \times 1000 = 5 \times 10^5$ values. In the case of modern computer architecture this is easy to compute but now consider a model that requires more parameters, the size of the likelihood scales as the product of the size of each parameter, very quickly becoming infeasible to perform direct calculations, especially in cases where the likelihood function is not well-behaved. In general the shape of the likelihood is unknown *a priori* so the number of samples along each dimension is also unknown. The solution for this is to use more sophisticated sampling techniques rather than the brute force method for constructing the posterior.

2.2.2 Markov Chain Monte Carlo

Markov Chain Monte Carlo (MCMC) techniques are the most common method for constructing the posterior distribution from the likelihood and priors. A markov chain is a general term describing a sequence of events where the current event only depends on the previous event. In general Monte Carlo techniques are processes that have probabilistic components. There are many versions of MCMC sampling

techniques but the earliest, which is still used today, is the Metropolis-Hastings algorithm.

This algorithm is able to sample from a probability distribution, $P(x)$, under the condition that there is a known function, $f(x)$, that is proportional to the desired distribution. In the case of Bayesian inference $P(x)$ is the posterior distribution and $f(x)$ is the product of the likelihood and the priors.

The algorithm starts with a selection of an initial point, x_i, which can be arbitrary, and choose a probability distribution, $g(x_{i+1}|x_i)$, that suggests the next point x_{i+1}, which can be any symmetric probability distribution; a common choice for this distribution is a Gaussian centered on x_i. Then a random number is drawn according to the distribution $g(x_{i+1}|x_i)$ resulting in a value for x_{i+1} which is then used to calculate the acceptance ratio, $\alpha = f(x_{i+1})/f(x_i)$, which determines whether the new value is accepted or rejected. Finally a random number, u, is generated on the closed interval $[0,1]$ and compared to α. If $\alpha \geq u$ the move is accepted and $x_{i+1} \rightarrow x_i$ and if $\alpha < u$ the move is rejected and the value of x_i is unchanged. This process guarantees that if $\alpha > 1$ the move will be accepted, meaning that regions of high probability will always be explored preferentially, but it also gives a non-zero chance of accepting moves to lower probability locations in the space to try to search for global features.

Metropolis-Hastings MCMC sampling is very simple to implement but has some shortcomings that need to be noted. Firstly it is inefficient since it only uses information from the previous step to inform the next step and because of this the samples are correlated so care must be taken to ensure enough samples are drawn that the final distribution is representative of the true distribution. Generally an accepted practice is to discard the some portion of the initial samples (of order thousands) known as a 'burn-in' to allow the sampler to settle into a reasonable estimate of the true distribution with finite steps.

There are more sophisticated sampling algorithms with the domain of MCMC
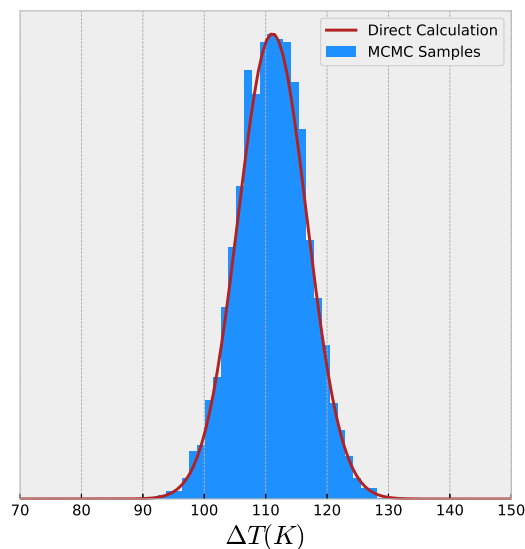
Figure 2.4: Comparison of the posterior for ΔT generated using the Metropolis-Hastings MCMC algorithm, with 10,000 samples, (blue histogram) and the posterior calculated directly (red line).

techniques, such as Hamiltonian Monte Carlo (HMC) algorithms which avoid the 'random-walk' aspect of Metropolis-Hastings by making use of the gradient of $f(x)$, the sampling distribution. This is a powerful method, but requires that $f(x)$ be differentiable and that the gradient is known, which is not necessarily true in the case of complex models. In particular within the models presented here neither of these conditions is met so it limits the utility of HMC methods.

The major benefit of using MCMC methods is that, unlike the direct calculation 'brute force' method, as the number of parameters increases the number of function evaluations scales favorably. There is not a precise scaling for the necessary number of samples but in general these methods are appropriate for sample models with even hundreds or thousands [48] parameters.

An python script of a Metropolis-Hastings Sampler is give here with the results shown in Fig. 2.4.

```python
"""
Example code of sampling a probability density P
using a Metropolis-Hastings MCMC sampler.

This example uses the 1-D case with fixed expansion coefficient
from the section on direct computation.
'''
"""
from numpy import random, empty, exp

#Set values of observed change in Volume and the error on measurement,
#expansion coefficient, and prior of the change in temperature, which
#is uniform so it is a constant for all values of T in its domain.
Y_obs = 0.02
sigma = 0.001
alpha_V = 1.18E-4
def prior(T):
  if T>=0 and T<=500:
    return 1
  else:
    return 0
#Define the function f(x), which is proportional to P(x)
def f(x):
  likelihood=exp(-(Y_obs-alpha_V*x)**2/(2*sigma**2))
  return likelihood*prior(x)
#Set the initial sampling point, which is arbitrary.
x0=200
#Make array for sampled values
mcmc_samples=empty(0)
#Define a number of samples to take
N_sample=1E5
#Define a burn_in period
N_burn=1000
#Here is the actual Metropolis-Hastings algorithm
for i in range(int(N_sample)):
  #This uses a Gaussian with std 100 for g(x1|x0) to determine x1.
  x1=random.normal(loc=x0,scale=100)
  alpha_mcmc=f(x1)/f(x0)
  if alpha_mcmc >= random.uniform():
    x0=x1
  mcmc_samples=append(mcmc_samples,x0)
```

2.2.3   Sequential Monte Carlo (Particle Filters)

Sequential Monte Carlo (SMC) sampling techniques[51], also known as particle filters, are an alternative to samplers that use Markov Chains and have a different set of advantages and disadvantages. In particular SMC samplers are designed to deal with distributions that have multiple peaks or have complex structure and that have a moderate dimensionality. The work presented in this thesis modeling HEDP systems falls comfortably into this category where the models usually have

about 10-15 parameters and form a complex likelihood surface, and therefore SMC sampling is used throughout. The downfall of SMC samplers is that they do not scale as well as other sampling techniques, in particular HMC samplers, so as the dimensionality of the problem grows the sampling efficiency will decrease and the posterior will take much longer to construct. In general when this occurs depends on the specifics of the models but once tens of parameters (roughly $> 20\text{-}25$) are introduced SMC samplers may begin to have challenges. A final advantage is that SMC samplers do not require gradient information, another critical aspect for models used within this work.

SMC algorithms can vary in detail, but the the principle involves sampling from a tempered posterior distribution by using a 'temperature' parameter, β, such as in simulated annealing, which smooths the likelihood surface in order to better capture all of contours present. The posterior that is sampled is given by

$$p(\vec{\theta}|\vec{Y}) \propto p(\vec{Y}|\vec{\theta})^\beta p(\vec{\theta}|F) \tag{2.4}$$

where β starts at 0, initially sampling only from the priors, and is slowly increased until eventually it reaches $\beta = 1$ and the posterior is being sampled. Along the way regions of high probability density are discovered and given weights based on Metropolis-Hastings Markov Chains that are run.

The algorithm used within this work is implemented within the python package PYMC3 [52] and takes the following steps[5]:

1) Start with $\beta = 0$ and take N samples, S_β, from the prior distribution.

2) Increase β until the effective sample size is equal to some value, usually $\approx 0.5N$ (with weighting based on the tempered likelihood).

3) Calculate N importance weights W, computed as the ratio of the tempered likelihoods between stage i and $i + 1$.

---

[5]This is adapted from PYMC3 documentation found at https://docs.pymc.io/notebooks/SMC2_gaussians.html.

4) Take N weighted samples, S_W, according to W.

5) Use S_W to create a Gaussian proposal distribution [$g(x_1|x_0)$ from Sec. 2.2.2].

6) Use the acceptance rate to scale the proposal distribution and calculate the number of step, m, used in the next sampling.

7) Run N Metropolis-Hastings MCMC chains, each with length m, each starting from a different sample in S_W.

8) Repeat steps 2-7 until $\beta \geq 1$, and if $\beta > 1$ set $\beta = 1$.

the final result of this process is a collection of N samples from the posterior.

Ultimately the SMC sampling borrows methods from a number of other statistical concepts, in particular importance sampling, tempering, and the use of a proposal distribution like in MCMC methods. Additionally, the stage based methodology where the samples are assigned weights and used to generate future samples can be thought of in the same vein as genetic algorithms.

2.3 Bayesian Inference in HEDP

Bayesian inference addresses many of the common issues found in analyzing experimental data from highly integrated HEDP measurements. Perhaps the most important advantage comes from the full construction of the posterior probability distributions, which not only give insight into the uncertainties on any given parameter, but also captures multiple explanations for the observed phenomena. This is critically important because in these systems there is no guarantee that the observations are sufficient to uniquely infer the parameters and this knowledge would be lost when using a point estimate technique. Additionally, Bayesian inference includes the use of prior distributions allowing previous measurements, physical constraints, and any other relevant information to be used to constrain a model that would otherwise be under-described by a single measurement.

There are a wide range of physical models used in HEDP ranging from simple

empirical models to full integrated 3-D radiation hydrodynamics codes. The most complex codes are often used to design experiments and interpret experimental data but their application to data analysis is challenging due to the extremely large number of parameters involved and the layers of different computations, such as equation of state calculation and atomic physics calculations, upon which the codes are built and often the codes are 'tuned' to match experimental data in a particular region of parameter space. This practice is unsatisfactory for the goals of this work so a different approach is used, in particular this thesis depends on constructing reduced physics models to describe experimental systems. These reduced physics models seek to isolate the key physical mechanisms that determine the observations from an experiment and in doing so reduce the parameter space of the models from many tens to hundreds, in the case of the full hydrodynamics codes, to approximately 10 in most cases.

This work intends to quantitatively determine meaningful measurements from experimental data. This end requires that whatever model used is parameterized by physically meaningful quantities so when a fit of these parameters is made to experimental data the results are able to be abstracted beyond the model. There is no guarantee of uniqueness when constructing a model. When faced with multiple models that adequately explain the observations preference is given based on Ockham's Razor, that is the simpler of the models is preferred. This can be evaluated quantitatively in multiple ways [47], for example by making use of Bayes factors [53] or other information criteria [54]. Additionally, it is desirable for the model to be computationally efficient enough to be sampled for Bayesian inversion, especially if there are multiple candidate models that need to be compared. This is not always possible, and depends on the specific requirements and complexities of the system; even when not possible directly there is potential for a surrogate model [55, 56] to be used in order to regain the computational efficiency needed to sample the model with an MCMC.

This does not eliminate the utility of the full physics codes, to the contrary they are an important and necessary tool in the flow of Bayesian inference in HEDP. In general it is critical to use the full physics codes to support the efficacy of the reduced physics models, since at a minimum the reduced physics models should be able to reproduce the quantities from the code with the region of parameter space the experiment is expected to reside, otherwise the inferred quantities from the reduced model are have ambiguity to their interpretation.

There are three key details that determine the efficacy of Bayesian inference in HEDP: (1) The full-physics model being used is believed to reasonably represent the experimental system; (2) The reduced-physics model accurately represents quantities of interest from the full physics model; and (3) the reduced-physics model can be constrained by the available measurements.

The first point is likely the most challenging to be fully convinced of and requires additional effort beyond what is presented here. The full-physics model need not be predictive of experiments but it must contain the essential physics of the experiment. For example, if there was significant asymmetry observed in an experiment, it is obvious that a 1-D model will not be sufficient to describe the system and a 2-D or 3-D simulation would be more appropriate along with a more sophisticated reduced model. The benefit of the reduced model over the full physics models is that they recast the full simulation parameter space, which has some large dimensionality dependent on the detailed physics in the model, into the reduced model parameter space that is less flexible in general but sufficient to describe an experiment that exists with a particular region of parameter space. The second point is addressed by seeing if there are a set of reduced model parameters that are able to reproduce profiles from the full simulation. The third point is addressed through the use of Bayesian inference [2], assuming that the system under consideration is well described by the full-physics model (first point), and the reduced-physics model adequately represents the pertinent quantities from the

full model (second point), the question remains as to whether the reduced model can be constrained by observations that are readily available or, if not, what measurements are required to constrain the model.

Ultimately, this process can be done with or without experimental data in hand. In the event the analysis is occurring after the experiment Bayesian inference can be used to figure out how much information about the physical system can be extracted from the data and, in the preferred case of performing this process before experimentation, the inference can inform what is able to be constrained through measurement and which measurement, or likely combination of measurements, are necessary to constrain the quantities of interest.

2.4 Practical Implementation

Implementing Bayesian inference tools is becoming increasingly easy given the growing support system surrounding these techniques and the efforts put into open source computational tools. Some of the most common tools exist natively within the statistical programming languages R and Stan and many packages exist within both Python and Matlab, commonly used in physics. The work in this thesis was done completely within Python, favored for its flexibility and large support for open-source software. Standard scientific and mathematical packages are used for data analysis, such as Scipy and Numpy, and the statistical package used for Bayesian inference is PYMC3 [52], which is a powerful tool for model specification and Bayesian inference. Since PYMC3 is actively developed there will not be many code examples given within this thesis, as they would likely be out of date fairly quickly. Rather general practices will be discussed which can be implemented with any number of tools in any of the widely available statistical packages or built from scratch. Nothing presented within this work is unique to any particular implementation and is reproducible in any framework.

The goal of this section is to provide some generally useful insight that may aide in implementing Bayesian inference in an HEDP setting and help in diagnosing problems that may occur.

2.4.1 Useful Heuristics

The models used in HEDP are likely fairly complicated relative to most examples that are available and include solving differential equations, numerical integration, convolutions, and other complex operations. This often requires troubleshooting difficult code that interfaces with some external packages that are not fully transparent. There are a number of simple checks that can be performed to ease the burden of this troubleshooting.

The first rule to keep in mind has been called the "folk theorem of statistical computing" by statistician Andrew Gelman[6] and says that when computational problems occur, it is usually due to a problem with the model being used. This is important to keep in mind because it is often tempting to think the sampling algorithm is at fault or the computational package being used but the sampling algorithms, as shown in Sec. 2.2.2, are not overly complicated and the statistical programs are widely used and tested by experts. This is not to say that bugs in the software do not happen but it is prudent to first look inward and confirm the model is well described and appropriate and if a bug is still suspected then reproduce it in as simple an example as possible and submit it to the developers of the relevant package.

When testing if a model is working properly there are a few basic quantities to check first. When doing Bayesian inference using a statistical programming package there are usually a few key pieces as laid out in the following pseudo code, which should be referenced along with Sec. 1.4.3 and table 2.1:

---

[6]https://statmodeling.stat.columbia.edu/2008/05/13/the_folk_theore/

```python
"""
Psuedo code describing the general form of
Bayesian inference codes

Here:
Y_data = Measurements
F = the model funciton that generates predictions of data
theta = the vector of parameters of the model
L = the likelihood function
"""
import necessary_function from necessary_packages
#Read in the experimental data and uncertainties from a file.
Y_data,sigma = load_data('data_file')
#Define some complicated function F(theta) that returns a vector in the
#same shape as Y_data
def F(theta):
  ...
  return Y_model
#Define a function that calculates the likelihood, here Gaussian
def L(theta,F):
  Y_model = F(theta)
  return exp(-(Y_data-Y_obs)**2/(2*sigma**2))
#define prior distributions, this can happen within a
#a model enviornment (like PYMC3) or not how these are
#defined depends on the library used for sampling.
priors = ...
#pass the priors and likelihood into the sampler which results in a posterior
posterior = statistical_package.sampler(likelihood,priors)
```

In the flow of this framework there are a few simple checks to administer if sampling is either going unusually slow (indicative of something wrong) or giving poor results. First it should be confirmed that the model function, F, is giving the expected results over the domain of parameter space under consideration. Often times some combination of parameters unexpectedly yields a 'Not a Number' (NaN), which will break the samplers, due to an unforeseen issue. Once F is confirmed to be working properly the likelihood function, L, should be confirmed to be giving reasonable results by checking values for reasonable estimates of the parameters involved. Thankfully in HEDP our models are often built on physical intuition so a reasonable range of parameters are known, such as temperatures, densities, etc. so some L can be confirmed to give larger numbers for more reasonable parameters and smaller numbers for less reasonable parameters. Ultimately the vectors Y_{data} and Y_{obs} should be plotted against each other and checked, in addition to the error σ, and checked against the relevant likelihood values to confirm

all of the calculations are correct.

Once the basic checks above are made, if the sampling is still slow, it is possible that the model is technically well specified (i.e. calculates correctly) but is poorly specified statistically. In particular it is good practice to make the expected values of the input parameters of order unity [7], since the kernel of the MCMC, $g(X_0|x_1)$ is usually a multidimensional Normal distribution and some sampler implementations have trouble dealing with very different scales across different dimensions. The easiest way to accomplish this is simply by changing units of parameters in the model, for example if there is a length parameter rather than using 10^{-6} meters it would be prudent to use 1 micron instead.

Another issue that can cause problems when sampling is if the model parameters are highly correlated. In general some correlation is no problem and likely cannot be simply avoided, but if there are highly correlated variables, especially with a large dimensional problem, the sampler may struggle to properly map the likelihood surface. In this case it is appropriate to re-parameterize the model to eliminate correlations. Within HEDP this is often possible through physical relationships such as equation of state where some problems are best served by using particular state variables as the parameters.

Finally a common issue in HEDP models is a multimodal posterior. It is good practice to run multiple chains, whether they be MCMC or SMC chains, to ensure the resulting posterior is stable. Sometimes the sampler will be stuck in a local extremum and not explore the whole space but different chains starting at different locations have a better chance of mapping this. This is a reason to use SMC samplers since they are more robust with respect to multimodal distributions.

Often many issues can be identified by plotting a few quantities including the full posteriors for each variable, the posterior predictions for the observations,

---

[7]Actually best practice is to scale all variable to mean 0 and variance 1 if possible, but this sometimes requires onerous transformations.

and the pairwise posteriors for the parameters. The posteriors in an individual variable should be free of high frequency features which are usually an indication of an under-sampled distribution. The posterior predictions, which are the posterior distributions for $\vec{\theta}$ passed through F to get $Y_{posterior}$ should be compared to Y_{obs}. If the range of $Y_{posterior}$ is either too big or too small as compared the observations and errors that indicates a problem. Finally in the pairwise posterior plots correlations can demonstrate which parameters are correlated and if oddly shaped contours exist it can be confirmed that enough samples exist in those regions of parameter space.

2.5   Areas of active research

There are two areas that require comment as actively being researched, both of which are important for Bayesian inference in HEDP settings and require significant research. These areas potentially depend on the details of the specific models being used and systems being studied as well.

2.5.1   Combining disparate datasets

HEDP experiments have a number of different modalities of measurement including spectral measurements, images, scalar numbers, and others. If all measurements are to be used simultaneously (as they should be) there must be a method for combining their contributions to the likelihood. The simplest method is to simple sum the likelihoods from each separately calculated measurement; a valid procedure if the measurements are uncorrelated. Summing the likelihoods implicitly asserts a weight to each measurement, but it is unclear whether they should be equally weighted or not. Does one scalar measurement have the same information content as a spectrum? Should each pixel in the image count individually or the entire image as one? Very quickly there is a set of questions that arise with no

clear answers. This issue is present in other areas of physics and in particular cosmology has faced this issue by adding weights to each likelihood component as parameters in the model and marginalizing over them [48]. This approach has yet to be tested on HEDP systems.

2.5.2 Choice of likelihood function

Another area of research includes the choice of likelihood function in a Bayesian inference analysis. In this thesis the default choice is a Gaussian likelihood, as described in Sec. 2.1. This choice is common because it is appropriate for normally distributed and uncorrelated errors and is a common choice in classical statistical methods but it is not necessarily always the best choice. As described in the supplemental material of Ref. [41] there are disadvantages to using this likelihood in particular for some of the data types common in HEDP. In particular data that is correlated such as spectra and images with finite resolution elements can lead to wildly under-predicted errors from using Gaussian likelihoods. This underscores the importance of carefully examining the results from a sampling to ensure that the resulting posteriors give predictions that are physically reasonable. It is likely there is not a single most appropriate likelihood for HEDP but rather each model and dataset will benefit from careful consideration and comparison across multiple choices.

Chapter 3

Convergent HED Experiments

Portions of this chapter are reproduced from [**J.J. Ruby**, J.A. Gaffney, J.R. Rygg, Y. Ping, and G.W. Collins. High-energy-density-physics measurements in implosions using Bayesian inference. *Physics of Plasmas*, 032703(28), 2021], with the permission of AIP Publishing.

Convergent geometries are suited for reaching the most extreme thermodynamic states as discussed in Sec. 1.2, and these systems have been used as a means achieving thermonuclear fusion since the Manhattan project. The study of convergent HED systems is dominated by increasing the efficacy of fusion platforms, either with the goal of achieving thermonuclear ignition on the laboratory scale[25, 57] or for the development of novel particle[58, 59] or x-ray sources[60–65] useful for other applications, but recently a new series of experimental platforms have been developed that capitalize on the unique conditions generated in implosion experiments to study the fundamental properties of matter[2, 3, 46, 66–68].

Designing implosion experiments with fundamental inquiry in mind, rather than application, necessitates working in a different region of design parameter space. This section will detail important design considerations for these experiments and give some examples of currently possible measurements and the information potentially available from such measurements.

3.1 Design of a convergent HED experiment

The design space of laser-driven implosions is expansive, consisting of target materials, layer thicknesses, laser pulse designs and target scales, that even when accounting for engineering constraints becomes effectively infinite. Even the subspace of "hot-spot ignition" [57, 69] targets that (broadly) consist of a hydrocarbon plastic outer shell layer, a solid deuterium-tritium (DT) ice layer, and DT gas, there are enough design parameters[1] to make optimization for a particular metric, such as neutron yield, difficult [55, 56, 70], a well-studied issue in the ICF community. In this work a narrow subspace is used as an example of how design changes can move experiments between different physical regimes. A list of common design parameters includes both laser drive conditions, such as total energy, pulse shape, and beam spot size, and target design, such as shell material, diameter, aspect ratio (shell thickness), fill material, and fill pressure, along with design differences that differ between direct-drive [69] and indirect-drive experiments [57] such as choice of hohlraum material and shape. Here direct drive experiments are considered with super-Gaussian spatial and temporal laser profiles, and targets that consist of plastic (CH or CD) and deuterium fill (where appropriate) with a fixed outer diameter. The target parameter that is varied is the thickness of the shell or the aspect ratio between the inner cavity and the shell, which moves the experiment through different regimes of energy transport.

The targets considered here can be broadly split into two defining groups, described by the mechanism of energy transport that dominates the implosion. The first group are shock-dominated targets in which the energy transport is dictated by the transit of a single spherical shock. Here the shock initially converges, compressing the target material that begins to flow inwards, upon reaching the target center, it rebounds, re-shocking the inflowing material. A key characteristic of

---

[1]In addition to the vastness of the design parameter space there is uncertainty in the proper values of underlying physics parameters that can effect the designs of experiments as well.
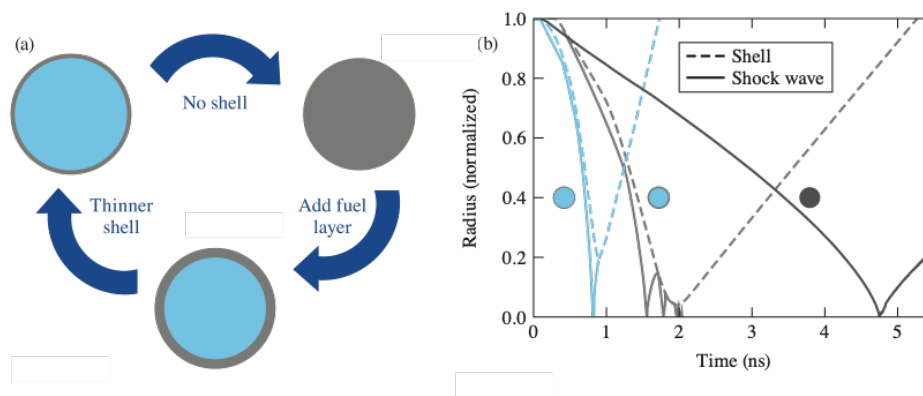
Figure 3.1: (a) A representation of the different implosion targets discussed within this work, (top-left) a gas filled thin shell, the subject of chapter 4, (top-right) a solid density sphere, and (bottom) a gas filled thick shell, the subject of chapter 5. Changing the thickness of the shell material moves the experiment between the compressive regime (thick-shell) and the shock dominated regime (others). (b) The shock trajectory (solid lines) and inner shell surface trajectory (dashed lines) for the targets shown in (a). Target thin-shell is shown in blue where the shock moves in, rebounds, hits the shell and reverses the shell trajectory, while the shock in target the thick-shell, shown in grey, reverberates off the converging shell and undergoes multiple passes through the gas leading to an isobaric hot spot. The solid sphere, shown in dark grey, has the same dynamics as the thin-shell, a single converging shock wave, but does not feature any shell since it is a single material target. Each trajectory is labelled with the corresponding representation from (a). Originally published in reference [4].

these systems is that after the shock rebounds and passes back through the material the flow of material is outwards leading to decompression. These targets have strong gradients in both space and time. The gradients in temperature, for example, result in temporally peaked x-ray emission. There is a self-similar semi-analytic model developed by Guderley that can be used to describe these types of implosions [1, 71].

The second group of targets are compression-dominated targets in which the energy transport is dictated by a massive shell that compresses and inertially confines an inner fuel. These systems also feature a strong converging shock wave that rebounds at the center of the target but when the rebound shock wave interacts with the massive converging shell of mass, this shell continues inwards leading to shock reverberations and further compression of the fuel. Standard ICF targets

fall into this category and there are a number of reduced models developed to describe the behavior [72–74] such as those characterized by a fuel with no spatial pressure gradients (isobaric).

Figure 3.1 shows examples of the targets that will be discussed in this work, including two shock dominated systems, solid density spheres and thin-shelled gas filled targets, and a compression dominated system consisting of a thick-shelled gas filled target. Figure 3.1 (b) shows a radius-time plot of trajectories for these different targets where the solid line is the shock-wave trajectory and the dashed lines are the shell trajectories (for the targets with shells). These trajectories are derived from the output of a 1-D radiation hydrodynamics code called *Lilac*[75]. This figure shows that for the solid target and thin-shelled target the shockwave simply converges inwards, rebounds, and diverges (reversing the trajectory of the shell in the thin-shell case). The thick-shell target shows the shockwave reflecting off the shell after rebound and undergoing multiple rebounds leading to the isobaric compressive hot-spot. This occurs because the shell has enough inertia that the shock wave is unable to reverse its direction on the initial interaction.

The dynamics of energy transfer, primarily driven by the hydrodynamics in the system, play a crucial role in when measurable emission is emitted and the nature of that emission. Diagnostic choices are a critical aspect of experimental design and the following section will discuss the types of measurements commonly made in convergent HED experiments.

3.2 Self emission measurements in HED experiments

Self-emission[2] in an HED context broadly falls into two categories, electro-magnetic (EM) emission (light) and particle emission. Within each of these categories there are a number of processes that give rise to different types of emission. EM emission in HEDP is predominately focused on the visible and x-ray parts of the spectrum, mostly for practical reasons. Laser facilities use either visible or near visible light, 351 nm in the case of the Omega60 Laser, so absorbed and scattered light can be diagnosed by observing these wavelengths and many systems reach temperatures where the black-body emission produces significant visible light which is relatively easy to measure[35] and therefore capitalized upon.

In spherical geometry, other than scattered light measurements diagnosing coupled laser energy and laser-plasma interactions, only limited parts of the spectrum are able to escape the system due to the absorption by highly compressed matter the emission needs to transit. X-rays with energy in the keV range ($\approx$ 1nm) are able to penetrate this compressed matter, escaping the target, and are therefore most commonly measured.

3.2.1 X-ray Emission

There are a number of processes that can produce photons with keV energies, most of which are interactions between a free or bound electron with an ion. These processes can broadly be categorized in terms of the initial and final state of the electron and include free-free emission (also known as bremsstrahlung), free-bound emission (also known as recombination), and bound-bound (also known as line emission). Considering an electron ion system, free-free emission refers to a

---

[2]Here self emission describes a process internal to the target of interest that generates observed radiation which can be contrasted with backlighting or probing techniques which use an external source to generate emission that interacts with the target.

free electron that interacts with an ion and remains free afterwards, free-bound emission refers to a free electron that enters a bound state with an ion releasing a photon in the process, and bound-bound refers to a bound state electron that transitions to another bound state releasing a photon in the process.

Similarly there are corresponding processes that determine the opacity of a material, the propensity of a material to absorb photons. Whether a photon is emitted or absorbed depends on energy conservation of the system, so in free-free processes the electron can interact with the ion and lose energy, emitting a photon, or the electron can absorb a photon in a 3-body interaction mediated by the ion and gain energy. Likewise with bound states an electron can transition from a higher energy state (or a free state) to a low energy state and release a photon or absorb a photon and be promoted from a low energy state to a high energy state, sometimes even to a free state (photoionization). Understanding the x-ray emission from an experiment requires a detailed accounting of these processes.

There is a rich study of atomic physics within HEDP plasmas [76–79] trying to understand the detailed processes of these atomic transitions. In this work primarily low atomic number (low Z) materials are used, such as hydrogen and carbon, and the temperatures are high enough to consider all of the electrons liberated from their respective nuclei and the dominant form of emission to be from free-free interactions.

The free-free spectral emission coefficient (emissivity) is derived by considering the Coulomb interaction between 2 free particles and integrating over all of the possible paths of approach. This derivation can be found in multiple sources [24, 80, 81]. The resulting emission coefficient is given by

$$J_\nu = \frac{\sqrt{2^{11}\pi^3}}{3} \frac{(\frac{e^2}{4\pi\epsilon_0})^3 \bar{Z}^2 n_e^2}{m_e^2 c^3 \bar{Z}\sqrt{3kT_e/m_e}} e^{-\frac{h\nu}{kT_e}} \quad \left[Js^{-1}m^{-3}Hz^{-1}\right] \quad (3.1)$$

where e, ϵ_0, m_e, c, k, and h, are the usual fundamental physical constants, A is

the total number of protons and neutrons in the ions, $\bar{Z}$ and $\bar{Z}^2$, are the average ionization state and average squared ionization state, T_e is the electron temperature, n_e is the electron density, and ν is the frequency of emitted photon. All quantities are in S.I. units and J_ν has the units of joules per second per meter^3 per hertz. Note that a closely related quantity is $\eta_\nu = J_\nu/4\pi$ which is the emissivity per steradian.

The propagation of radiation is given by the radiative transfer equation[24, 80, 82]

$$\frac{1}{c}\frac{\partial I_\nu}{\partial t} + \vec{\Omega} \cdot \nabla I_\nu = \rho\tilde{\eta}_\nu\left(1 + \frac{c^2}{2h\nu^3}I_\nu\right) - \rho\kappa_\nu I_\nu \tag{3.2}$$

where I_ν is the spectral intensity, which can be thought of as a photon distribution function [80], $\vec{\Omega}$ is the direction vector, ρ is the mass density, $\tilde{\eta}_\nu$ is the specific spectral emissivity or spectral emission coefficient per unit mass^3 (η_ν/ρ) and κ_ν is the mass absorption coefficient, also known as the opacity.

In this work emission is considered under the conditions of local thermodynamic equilibrium (LTE), meaning that individual populations of particles have had sufficient time to relax into Boltzmann distributions meaning a temperature can be prescribed. This does not require that different species, i.e. electrons and ions, have the same temperature nor does is it taken to mean that the particles are in equilibrium with the radiation field.

When the radiation field is in equilibrium the photon distribution takes the form a Planckian, or black body, given by

$$I_{BB} = \frac{2h\nu^3}{c^2}\frac{1}{e^{h\nu/kT} - 1} \tag{3.3}$$

---

^{3}Note the difference from Eq. 3.1. Terminology in many texts is confused but for dimensional consistency the spectral emission coefficient that appears in the radiation transfer equation must be per unit mass, although this distinction is often omitted.

and this can be inserted into Eq. 3.2 to obtain Kirchhoff's law

$$\frac{\tilde{\eta}_\nu}{\kappa_\nu} = \frac{\eta_\nu}{\rho\kappa_\nu} = \left(\frac{2h\nu^3}{c^2}\right) e^{-h\nu/kT} \tag{3.4}$$

which relates the emissivity of a material to its opacity. Kichhoff's law, despite using radiative equilibrium to derive it, holds in general under LTE conditions meaning Eq. 3.2 can be recast to

$$\frac{1}{c}\frac{\partial I_\nu}{\partial t} + \vec{\Omega} \cdot \nabla I_\nu = \rho\kappa_\nu' \left(I_{BB} - I_\nu\right) \tag{3.5}$$

where the explicit dependence is only on the opacity through the modified expression

$$\kappa_\nu' = \kappa_\nu \left(1 - e^{-h\nu/kT}\right). \tag{3.6}$$

Using Eqs. 3.1 and 3.4 we can get an expression for the free-free opacity

$$\rho\kappa_\nu = \alpha_\nu = \frac{4\sqrt{2\pi}}{3\sqrt{3}} \frac{\left(\frac{e^2}{4\pi\epsilon_0}\right)^3 \bar{Z}^2 n_e^2}{m_e^{3/2} hc\nu^3 \bar{Z}\sqrt{kT_e}} \quad \left[m^{-1}\right] \tag{3.7}$$

where α_ν is the linear attenuation coefficient at frequency ν. When plasmas are fully ionized there are no bound electrons left attached to the ions so free-free absorption is the only mechanism that needs to be considered (neglecting scattering which becomes important for high photon energies $> 100keV$). The fully ionized case is the limit of lowest opacity and the limit of highest opacity is known as the 'cold' opacity and is the value when there is no ionization (which is general true at lower temperatures) meaning bound electron interactions dominate. In HED plasmas the opacity of the system can take the value between the cold and free-free limit. Examples of the opacity predicted for a Silicon (Si) plasma at solid density, 2.33 g/cc, and 3 different temperatures (10 eV, 1 keV, and 10 keV) are shown in Fig. 3.2 (left). The core electrons of Si require energies of 2440 eV and

2670 eV to be liberated and the most weakly bound electrons require energies of 8.15 eV and 16.3 eV to be liberated meaning that, to a good approximation, at 10 eV Si has most of its electrons still bound (potentially singly ionized), at 1 keV Si is likely ionized all the way up to the K-shell (quantum number n=1 electrons) because the the highest ionization energy in the M-shell (n=2 electrons) is 523 eV meaning is has an ionization, $\bar{Z}$=12, and at 10 keV Si is likely fully ionized with $\bar{Z} = 14$.

In Fig. 3.2 (left) the 3 different curves show the cold opacity, the free-free opacity, and calculated opacity from astrophysical opacity tables (AOT) [83] that span the difference between the cold and free limits depending on the conditions. The feature in the cold and AOT opacities around 2 keV is the K-edge of Silicon, an absorption feature from the bound-free transition of the K-shell electrons which have a binding energy of 1.839 keV.

Using free-free opacity, a simple example of a solution to the radiation transfer equation is presented for the case of a uniform slab of material in steady state. Inspecting Eq. 3.5 this scenario eliminates the temporal derivative term on the left and ultimately results in a first order inhomogeneous ODE whose solution is:

$$I_\nu(x_0) = \int_0^{x_0} \rho(y)\kappa'_\nu(y)I_{BB}[T(y)]e^{-\int_y^{x_0} \rho(z)\kappa'_\nu(z)dz}dy + I_0 e^{-\int_0^{x_0} \rho(x)\kappa'_\nu(x)dx} \qquad (3.8)$$

where x is along the axis of interest through the slab and I_0 is the radiation incident on the slab, which we will take to be 0 for this example. The way Eq. 3.5 is cast emphasizes how I_ν reaches the equilibrium distribution, I_{BB}, and the results are shown in Fig. 3.2 (right). Here the solution, Eq. 3.9, is plotted for a slab of fully ionized hydrogen plasma at 1 keV with thickness 50μm for different densities (shown in the legend). The dotted line is the black-body distribution, which is nearly achieved for the highest density shown (1 kg/cc). As the density increases the equilibrium distribution is reached for progressively larger photon energies as
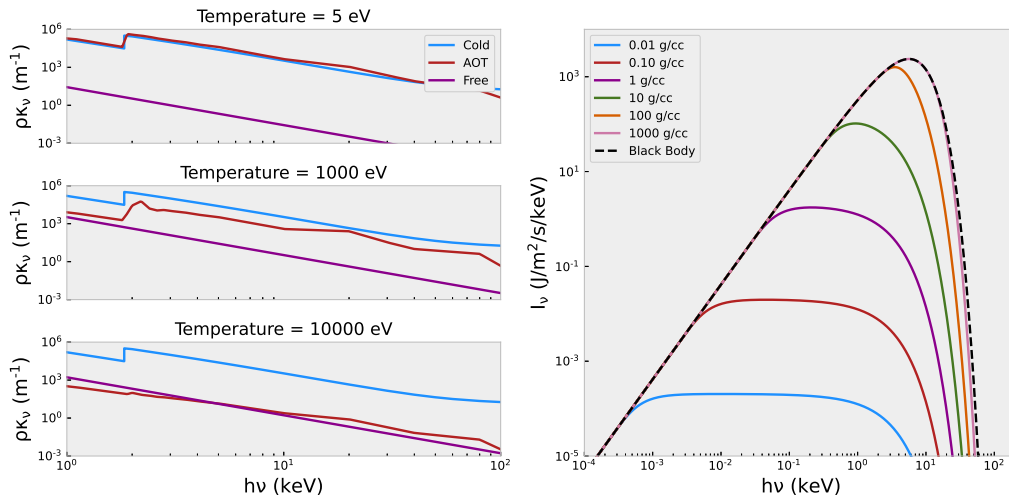
Figure 3.2: (let) A comparison of 3 different linear attenuation coefficients derived from the cold opacity (blue), Los Alamos astrophysical opacity (red), and free-free opacity (purple) for solid density Silicon at 3 different temperatures. At the lowest temperature (5 eV) Si is, at most, singly ionized making the astrophysical opacity very similar to the cold opacity, while at 1 keV Si has significant ionization but likely retains core electrons leading to an opacity between the cold and free-free limit, and at the highest temperature, 10 keV, Si is fully ionized leading the modeled opacity to match the free-free calculation. (right) The transition of a 50 μm thick slab of hydrogen plasma at fixed temperature (1 keV) from optically thin, at low densities, to optically thick at higher densities eventually converging towards the black body limit (dashed line) for spectral intensity.

the plasma becomes optically thick at those energies. At higher energies, and lower densities, the plasma is optically thin, meaning there is not significant absorption effects, meaning that I_ν takes on a temperature and density dependence associated with free-free emission

$$I_\nu \propto \rho^2 e^{-h\nu/kT}. \tag{3.9}$$

This result is heavily used in convergent HED studies where there is usually other absorbing material (namely remaining dense shell material) that limits measurements of x-rays to higher photon energies where the emitting plasma is optically thin.

3.2.2   Particle Emission

The extreme density and temperature environment produced in HED experiments can result in nuclear fusion reaction, depending on the chemical composition of the material. The fusion reactions serve as an indicator of environment from which they were produced. Commonly observed products from fusion reactions in HED experiments include neutrons and protons from the fusion reactions such as the Deuterium reactions D(d,p)T and D(d,n)³He and the deuterium-tritium reaction D(t,n)α, significant due to its high cross-section at conditions relevant for terrestrial fusion reactors. This work has focused exclusively on the D(d,n)³He deuterium-deuterium (DD) fusion reaction and one of its products, a neutron with 2.45 MeV of energy.

The nuclear production rate in a differential volume element, for a DD fusion reaction, is given by

$$\frac{d^2N}{dtdV} = \frac{1}{2}n_D^2 < \sigma v >_{DD}$$
(3.10)

where n_D is the number density of Deuterium ions, the factor of $\frac{1}{2}$ is to prevent double counting interactions between 2 deuterium ions, and $< \sigma v >_{DD}$ is the local thermal reactivity averaged over a Maxwellian ion velocity distribution with temperature T and can be calculated using the fusion reactivities from, for example, Bosch and Hale [84].

Assuming there is a volume of deuterium plasma with temperature T and density ρ sufficient to produce thermal DD fusion reactions the energy spectrum of the resulting particles will be influenced by the local thermodynamic conditions. In an isolated environment the spectrum of DD fusion neutrons would have a sharp peak located at $\approx 2.45 \ MeV$ but when born in a thermal bath the spectrum will be broadened proportional to the ion temperature, T_i, an effect that is well studied [85, 86] as a primary means of diagnosing ICF implosions [87] An example of a calculated neutron birth spectrum can be seen in Figure 3.3. Additional interesting
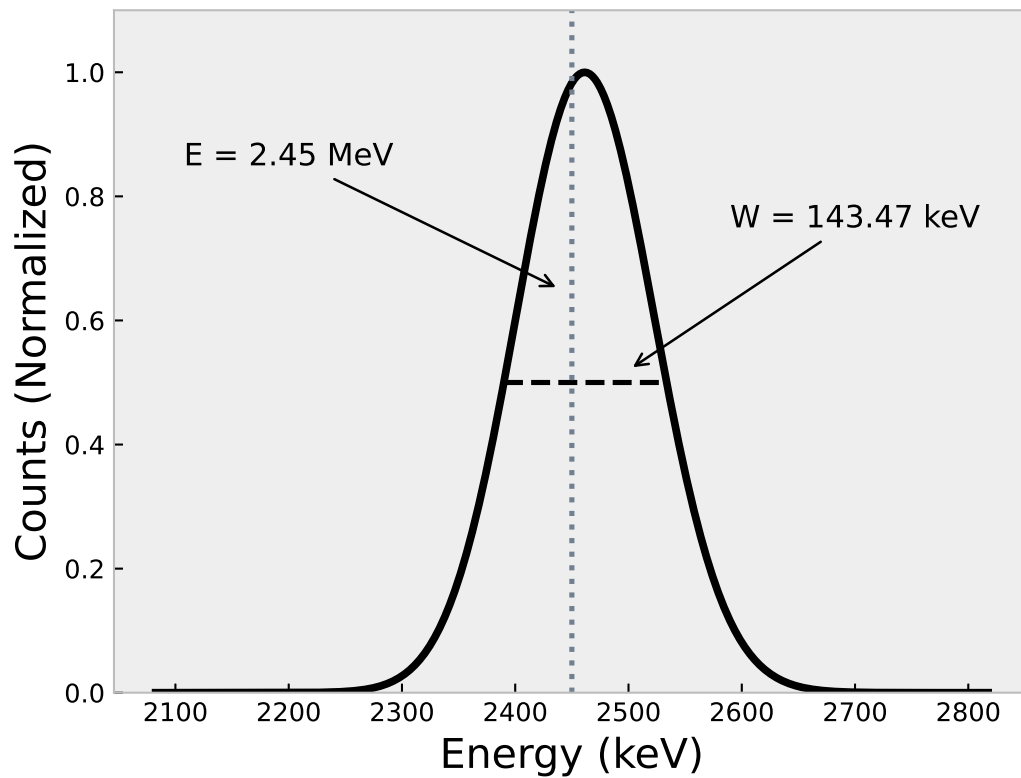
Figure 3.3: DD fusion neutron birth spectrum for a 3 keV deuterium plasma. The spectrum is both shifted and broadened due to the temperature. The mean energy is shifted up by $\approx 10 \; keV$. The full-width half-max, W, of the spectrum is 143.47 keV and is related to the ion temperature of the emitting plasma by Eq. 3.11. The vertical dotted line shows the nominal birth energy of the neutron in a non-thermal environment.

quantities follow from various integrals of Eq. 3.10, such as total neutron yield (given by the volume and time integral of equation 3.10) and the time dependent neutron production history (given by the volume integral of equation 3.10).

An example spectrum [86] of thermonuclear DD fusion neutrons is shown in Fig. 3.3 for a pure deuterium plasma with a mass density of 100 mg/cc and an ion temperature, $T_i = 3$ keV. The spectrum is upshifted in energy, with the peak at about 2.46 MeV rather than 2.45 MeV (shown by the vertical dotted line), and broadened with both effects due to the velocity distribution of the fusing ions. The width of the spectrum is often used as measure of integrated ion temperature[87] in ICF implosion the relationship of the full-width half-max, W, to T_i is given by [85]

$$W = \omega_0 (1 + \delta_\omega) \sqrt{T_i} \tag{3.11}$$

where ω_0 and δ_ω are fitting parameters given in [85] and take the values of $82.542\text{keV}^{1/2}$ and 0.005 for DD fusion at 3 keV. When $W = 143.47$ is plugged in from the generated spectrum the resulting ion temperature is 2.99 keV, consistent with the value used to generate the spectrum.

3.2.3 Types of Measurements

There are 3 primary axes upon which both the x-ray and particle emission can be scrutinized: spatial, temporal, and spectral. Measurements can be isolated to any individual axis or can be some combination of all 3. There are many advanced tools [37] that are routinely used to make measurements in these extreme environments. This section will provide a brief discussion of commonly used diagnostics but should not be considered a comprehensive survey of the field.

Imaging techniques of high energy[4] particles whether photons, neutrons, or

---

[4]The scale of energies in physics covers many orders of magnitude and the range of energy considered in this work to be high, in the keV to MeV range, is likely considered low to many researchers in high energy physics (particle physics) where particles routinely reach GeV and

charged particles are generally non-refractive, unlike most optics used in the visible and near visible spectral ranges, due to nature of the radiation. This requires either simple apertures, such as pinholes or slits, or diffractive optics, such as Kirkpatrick-Baez (KB) microscopes [88] or Fresnel Zone Plates (FZP) [5]. Here imaging will be discussed in terms of x-ray emission, which is a standard measurement in convergent HED experiments, but most techniques apply to high energy particle imaging as well. The simplest and most widely used imaging element is a pinhole, whose spatial resolution is roughly equivalent to the diameter of the pinhole [89] until the Fraunhofer limit is reached and diffractive effects, determined by the wavelength of the radiation being imaged, prevent further resolution.

The pinholes can routinely be manufactured to 5μm but the solid angle of acceptance scales as the diameter squared, meaning there is a trade-off between signal and resolution. Another aspect of pinholes that can be beneficial or detrimental, depending on the measurement, is that they are able to image broadband sources, such as a plasma emitting thermal free-free emission. Pinholes can be pushed to much larger solid angle and resolution by making use of penumbral imaging [90] although this introduces an additional step of having to reconstruct the source from imaged penumbra. Diffractive optics image monochromatically based on the characteristic length scale of the material used, whether it be naturally occurring crystals or manufactured patterns. These optics have the benefit of both larger solid angles and higher resolution, for example KB microscopes used on HED experiments have shown 5μm resolution [89] and FZPs have been demonstrated to have $\approx 1\mu$m resolution on HED experiments, limited by the detecting medium [5].

Detectors that provide temporal resolution broadly require 2 stages when measuring the radiation considered here: 1) a conversion from x-rays (or nuclear products) to electrons, either directly or by first converting to near visible light 2) the

---

greater energies.

electrons are then focused to different spatial location via a time-varying voltage mapping temporal information to a spatial dimension within the detector. This process primarily used streak cameras [91] to attain temporal resolutions as low as 10 ps. There are numerous detectors that operate on these principles across HEDP [92–95].

Spectral discrimination works differently between particle and photon detection in large part due to the difference in time-of-flight (tof) between the types of radiation. Experiments happen within a vacuum chamber where the x-rays that are detected all propagate at the speed of light while the particles that are detected travel with some velocity that depends on their energy. Particle spectra leverage this difference in velocity by placing detectors far away from the source ($\approx$ meters) and detecting when particles arrive which then informs the energy of the particles [37, 87, 96].

The spectral discrimination of x-rays makes use of Bragg's law [97] $2dsin(\theta) = n\lambda$ which relates the spacing of some grating, d, and the angle of diffraction, θ, to the order of diffraction, n, and the wavelength of the light that is diffracted λ. Making use of diffraction x-rays can be spectrally dispersed by using gratings with appropriate spacings; for the x-rays under consideration here the gratings take the form of crystals with various d-spacings within the lattice depending on the specific range of x-ray energies being investigated. Another way to achieve spectral discrimination, in both x-rays and particles, is by using transmission filters to allow only radiation of a certain energy to get through. This can be done with simple thresholding [98] or by using different k-edges to create Ross-pairs [99] to allow only a particular range of energies through.

Finally different combinations of these detection schemes can be used in conjunction to get temporally resolved images or spectra by coupling an imaging slit or a crystal spectrometer to a streak camera, spectrally dispersed imaging by coupling a slit to a crystal spectrometer or using a series of different filters on a

pinhole, and more. This work makes great use of a temporally gated pinhole imager called an x-ray framing camera (XRFC) [38, 100] which uses similar principles to a streak camera to record pinhole images at snapshots in time.

Chapter 4

Thin Shell Experiments

Portions of this chapter are reproduced from [**J.J. Ruby**, J.R. Rygg, D.A. Chin, J.A. Gaffney, P.J. Adrian, D. Bishel, C.J. Forrest, V.Yu. Glebov, N.V. Kabadi, P.M. Nilson, Y. Ping, C. Stoeckl, and G.W. Collins. Constraining physical models at gigabar pressures. *Physical Review E*, 102(5):53210, 2020] and [**J.J. Ruby**, J.R. Rygg, D.A. Chin, J.A. Gaffney, P.J. Adrian, C.J. Forrest, V.Yu. Glebov, N.V. Kabadi, P.M. Nilson, Y. Ping, C. Stoeckl, and G.W. Collins. Energy Flow in Thin Shell Implosions and Explosions. *Physical Review Letters*, 125(21):215001, 2020] Copyright (2020) by the American Physical Society

The first experimental system used to demonstarate Bayesian infrence in implosion experiments is a shock driven system, as discussed in Sec. 3.1, where a strong shock wave is driven in a gas density target with a thin outer shell. This particular experiment was performed on the 60-beam OMEGA Laser System [31] at the Laboratory for Laser Energetics. A sketch of the experimental setup is shown in Fig. 4.1 (a) where the target is an 879-μm SiO_2 glass shell with $3 - \mu$m-thick walls. The shell was filled with 18.9 atm of deuterium gas. The target was illuminated with 60 spherically configured UV laser beams containing 230 J per beam in a 600-ps super-Gaussian square pulse. The beams were configured with SG-5 distributed phase plates [101], resulting in a super-Gaussian spatial profile with diameter of about 850 μm.
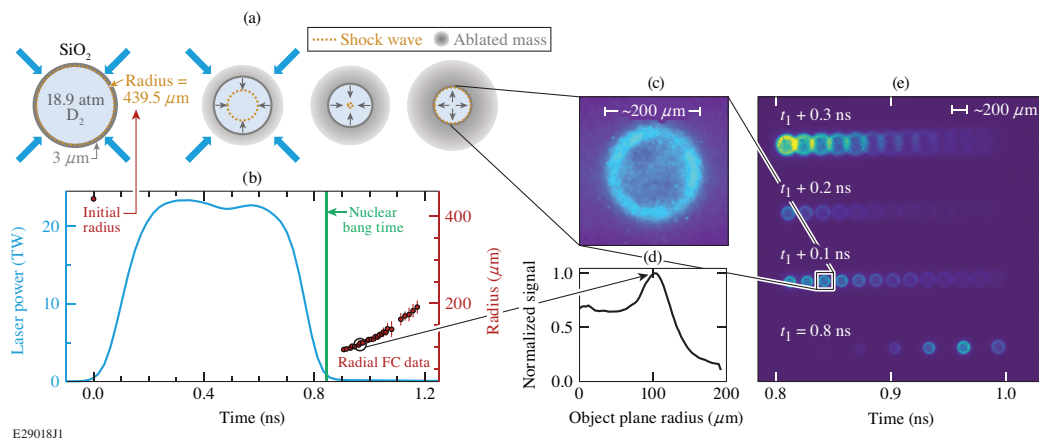
Figure 4.1: (a) Schematic of the experimental setup, showing a 3-μm SiO$_2$ shell filled with 18.9 atm of D$_2$ gas. Symmetric laser illumination drives a shock wave (dashed gold curve) through the shell into the gas and the shell continues to converge. The shock wave reaches the center of the target and then returns moving outward and eventually interacts with the shell a second time. (b) The time history of the laser drive and measurements along with the time that the shock reaches the center of the target given by the nuclear bang time (vertical green line), a measurement of thermonuclear fusion products due to the extreme temperatures and densities created by the converging shock wave. When the rebounding shock wave interacts with the shell, the conditions generate the x-rays (e) measured in the roughly 30-ps snapshots. (d) The peak of the radially averaged lineouts corresponds to the ring of emission in the (c) individual snapshot and the red data points shown in (b). Originally published in reference [3].

4.1   Self-Emission Measurements of Exploding Shell

When the laser drive hits the shell a strong spherically converging shock wave is launched via mass ablation [80], first into the glass shell, transiting the shell and breaking out into the deuterium gas, eventually reaching the center of the target. Once at the center, the shock is strong enough to generate deuterium-deuterium fusion reactions and a nuclear particle yield is measured. The shock then moves back outward through the deuterium gas and eventually interacts with the glass shell that was set on a converging trajectory by the first shock interaction. Once the rebound shock hits the shell, the material becomes hot enough to have significant ionization and produces bremsstrahlung x-ray emission. This emission is measured using a pinhole array that projects 2-D images onto an x-ray framing camera that uses a voltage sweep to temporally gate the images [38]. This gives a series of snapshots of the emitting shell projected onto the 2-D camera as shown in Fig. 4.1 (e). The center of each snapshot [Fig. 4.1 (c)] is found, and a radially averaged measurement of the x-ray emission is taken, shown in Fig. 4.1 (d). Since the shell emission is localized in space, this measurement gives the trajectory of the shell, which will be the focus of the Bayesian methods implemented here. The trajectory is shown in Fig. 4.1(b) along with the initial radius, laser pulse, and nuclear bang time. The errors on the trajectory points are determined from the experimental uncertainty in magnification and from the variation in the radially averaged location of the peak emission.

4.2   Modeling Efforts

This work makes use of 2 distinct types of models: 1) The reduced models designed to extract information from measurements and 2) integrated physics models that are used as a surrogate for experiments to test analysis methods including the

reduced models. A key aspect of this work is that the integrated physics models are not used to interpret experimental data (however tempting that may be) the reason being that these models are over-parameterized and under-constrained by the measurements available oftentimes making the interpretations unclear in difficult to quantify ways.

There are three key details that determine the efficacy of this process: (1) The full-physics model being used (in this case a 1-D radiation-hydrodynamics code) is believed to reasonably represent the experimental system; (2) The reduced-physics model accurately represents quantities of interest from the full physics model; and (3) the reduced-physics model can be constrained by the available measurements.

4.2.1 Mechanical Model of Shell

The reduced model used to describe the thin shell experiment uses ten total parameters. There are three parameters that describe the shell, M_f, R_f and v_f which are the mass of the shell, radius of the shell, and velocity of the shell, respectively. The second-order ordinary differential equation (ODE),

$$\frac{\mathrm{d}^2 R}{\mathrm{dt}^2} = \mathrm{a},\tag{4.1}$$

where R is the radial location of the shell and a is the acceleration of the shell. The acceleration takes the form

$$\mathrm{a(t)} = \begin{cases} 0 & \mathrm{t} < \mathrm{t_a} \\ \frac{4\pi R^2 P}{M} - \frac{\dot{M} v_e}{M} & \mathrm{t_a} \leq \mathrm{t} < \mathrm{t_l} \\ \frac{4\pi R^2 P}{M} & \mathrm{t} \geq \mathrm{t_l} \end{cases}\tag{4.2}$$

where P is the pressure pushing outward on the shell due to the fuel inside and M is the mass of the shell both of which (along with the radius, R) are time-dependent quantities, while the ablation rate, $\dot{M}$, and exhaust velocity, v_e, are

both time independent. The acceleration starts when $t \geq t_a$, interpreted as the time ablation starts. At this point there is an outward force from the fuel inside the shell and an inward force from the rocket effect of the ablated mass. Once the laser turns off at t_l the force from mass ablation stops and only the outward force from the fuel remains. The pressure profile from the fuel is given by

$$P(t) = \begin{cases} (P_{rs})e^{-\gamma_g(t_s - t)} & t \leq t_s \\ (P_{rs})e^{-\gamma_d(t - t_s)} & t \geq t_s. \end{cases} \tag{4.3}$$

with exponentially growing term with growth rate, γ_g, for times before t_s and an independent exponentially decaying profile with decay rate, γ_d, for times after t_s. The peak pressure reached is given by P_{rs}, which is interpreted at the pressure of the rebounding shock wave.

The mass of the shell is given by

$$M(t) = \begin{cases} M_0 - \dot{M}(t - t_a) & t \leq \min[t_s, t_M] \\ M_{\min} + \dot{M}(t - \min[t_s, t_M]) & t > \min[t_s, t_M] \end{cases} \tag{4.4}$$

where t_M is the time it takes to lose all of the mass of the shell and $M_{\min}$ is the minimum mass the shell achieves. The shell continually loses mass to ablation at a constant rate while the laser is on and to material release after the laser stops until the shell trajectory reaches its minimum. At this point the shell starts moving outward and regains the released mass as it moves out.

4.2.2   1-D hydrodynamics simulation for synthetic data

Addressing whether this model has a physically relevant parameterization and can be constrained given a particular measurement must be addressed before using the model to extract information from the experimental data. This is done by using a synthetic experiment, in this case generated by using the 1-D Lagrangian

hydrodynamics code *LILAC* [75] and producing synthetic experimental data which is then fit by the model. The underlying physics in the simulation can then be scrutinized to see how well the model parameterization compares. The ability to simulate both physical systems of interest and detectors used to measure those systems is a critical aspect of Bayesian inference and provides great insight into not only analysis, but also the design of experiments.

The *LILAC* simulation was run using experimental spatial and temporal laser beam profiles, a flux-limited thermal-transport model with flux limiter $= 0.12$, a 3μm SiO$_2$ shell using *SESAME* equation of state 7380 [102] (for reference more recent tables include *SESAME* 7360 and 7361), and 436.5 μm of deuterium gas at initial density $= 10.4$ mg/cm^3 (pressure $= 18.9$ atm) using *SESAME* equation of state 5262 [102]. The simulation outputs were post-processed to calculate the x-ray emission in each zone by calculating the bremsstrahlung emissivity (Eq. 3.1) given by

$$J_\nu = \frac{\sqrt{2^{11}\pi^3}}{3}\frac{(\frac{e^2}{4\pi\epsilon_0})^3\bar{Z}^2 n_{\mathrm{e}}^2}{m_{\mathrm{e}}^2 c^3 \bar{Z}\sqrt{3kT_{\mathrm{e}}/m_{\mathrm{e}}}}e^{-\frac{h\nu}{kT_{\mathrm{e}}}}\quad \left[Js^{-1}\mathrm{m}^{-3}\mathrm{Hz}^{-1}\right] \qquad (4.5)$$

here $\bar{Z} = 1$ for deuterium and $\bar{Z} = 10$ for SiO$_2$. The emissivity of each zone is then multiplied by the zone volume, integrated over 30 ps, and integrated for photon energies above 5 keV. The temporal and spectral integrations both are meant to roughly represent the temporal and spectral response of the framing camera used in the experiment. The result of this is a series of radial lineouts of x-ray emission from the simulation, which are then Abel transformed in order to replicate the signal of the projected 2-D image measured in the experiment.

The posterior distributions were sampled using a sequential Monte Carlo (SMC), discussed in Sec. 2.2.3, from the PyMC3 [52] library. A sampling for the simulated data, $\vec{Y}_{\mathrm{sim}}$ was done using Gaussian likelihood function and assuming 3 μm error on each of the points.

The choice of priors is one way that additional information, outside of measured

data, can be used to constrain an otherwise underdescribed model. In this case there are ten parameters in the model in total but five of the parameters have strong priors due to physical limitations or measurement. These five parameters are R_0, M_0, t_a, t_l, and t_s. The first two are target parameters that are metrologized prior to the experiment so they take the form of normal distributions around the central values with uncertainty given metrology limitations. The last three parameters all coincide with temporal events observed in the experiment, such as the laser turning on and off, and the onset of shell emission corresponding to shock heating. Additionally, physical considerations such as the mass, radius, and pressure all being strictly positive provide constraint. The other parameters, which are not as well constrained *a priori*, receive broad normal priors that are mostly uninformed with the exception of physical of bounds such as for the ablation rate and exhaust velocity both of which must be strictly positive quantities. The Bayesian framework allows all of this information to be explicitly imposed and uses them to further constrain the system.

Once the posterior distributions of the model parameters are constructed (through the SMC sampling) values can be drawn from the distributions and passed through the model to generate posterior predictive distributions (PPD) for the shell trajectory and pressure profile. The PPD gives a prediction for what additional measurements would provide, based on the given model. In this case for a given time there is a probability distribution for the radius and the pressure and by sampling the PDD at many times a probabilistic band of trajectories and pressures profiles can be constructed.

Since there is not a unique model to describe the system. It is important to consider a range of models and quantify how they compare. Differences in model can come in the form of different functional forms, $F(\vec{\theta})$, or simply a different choice of priors on models that otherwise have the same expressions. Here, an example of a comparison between two different models with different functional

forms is given. M_1 is the model previously described, and model M_2, has identical parameters except for the pressure profile, which has an additional parameter changing the amplitude before and after t_s,

$$P(t) = \begin{cases} (P_0)e^{-\gamma_g(t_s-t)} & t \leq t_s \\ (P_1)e^{-\gamma_d(t-t_s)} & t \geq t_s. \end{cases} \qquad (4.6)$$

This profile is meant to represent the jump in pressure due to the shock front hitting the shell. Although it may seem obvious that a model with a pressure jump would be more appropriate, there is no guarantee that the measurements, which happen in trajectory space and after the shock hits the shell, have leverage on the pressure profile earlier in time. This coupled with the additional parameter for pressure means the M_2, while physically motivated, may not be preferred over M_1 based on the data.

Model comparison is standard practice in Bayesian inference, and there are many methods that can be used. In this case three different methods were compared: widely applicable information criteria (WAIC)[54, 103], leave one out cross validation (LOO)[54, 103], and Bayes factor[104, 105] calculations.

Unlike model comparisons based on point estimates of parameters, such as likelihood ratios or F-test metrics, Bayesian model comparisons account for the full posterior distribution of parameters. This means that the uncertainty in parameter estimates is also part of the calculation[54]. The Bayesian information criteria (WAIC and LOO) attempt to quantify the predictive capability of the model to unobserved data, while comparing Bayes factors amounts to a more-generalized form of a likelihood ratio test that includes marginalizing over the posterior distributions of each parameter, therefore not relying on a point estimate.

All three metrics agree when comparing M_1 and M_2, showing a slight favor for M_1. A benefit of Bayesian model comparison is that it provides a weighting

E29106J1
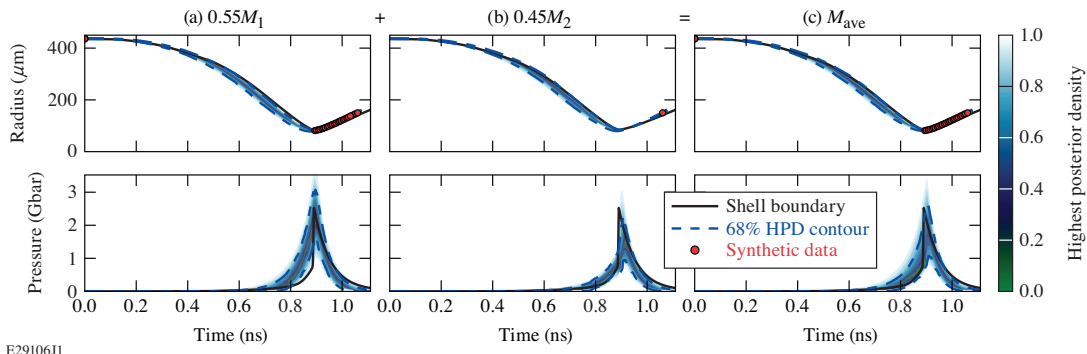
Figure 4.2: PPD for the trajectory and pressure profiles for (a) M_1, (b) M_2, and (c) the averaged model based on weightings from the WAIC. The weights for M_1 and M_2 are given above the images and are 55% and 45%, respectively. The averaged model is constructed by taking the samples from each model based on the relative weightings. The combined model shows improved agreement with the with simulation trajectory falling within the 68.3% HPD interval at all times and better agreement in both the pre-shock pressure profile than M_1 and around the time of peak pressure than M_2. Originally published in reference [2].

to average the models together. In this case PPD samples of the trajectory and pressure profiles are sampled based on the weights assigned by the information criteria, resulting in PPD's for the trajectory and pressure profile based on both models. An example composite model is shown in Fig. 4.2 (c), where the trajectory and pressure profile shown in (c) are composed of a weighted sampling of the model, M_1 and M_2, shown in (a) and (b), respectively. In this case, the weighting was established by using the WAIC information criteria, but LOO and the Bayes factors gave very similar weightings.

Since the synthetic data were generated from a hydrodynamics code, the trajectory of the shell and pressure profile is known for all times. In this case comparison is made to the innermost zone of SiO_2 in the code, which is the zone that borders the fuel. The trajectory and pressure in this zone are shown as solid black lines in Fig. 4.2. Intervals of increasing probability for the PPD are shown by the colorscale. The model displays good predictive capability across all times, with the "true" values from the code usually falling inside the 68.3% confidence interval (dotted-dashed blue lines). This demonstrates that the model has predictive

capability outside of the regions where data are directly measured.

4.3   Results

After testing the utility of the reduced model using a synthetic experiment, the same process can be applied to experimental data. M_1 and M_2 were sampled the same way as the synthetic experiment, but now using the real experimental data, $\vec{y}_{\mathrm{exp}}$. The models were then averaged the same way, with relative weightings of 0.54 and 0.46 respectively (given by WAIC).

The posterior distributions of the parameters give important insight into how well constrained the models are by the data. Figure 4.3 shows the posterior distributions for the nine parameters that are common to both M_1 and M_2. Among these, most have similar distributions except for $\dot{M}$ and v_{e}. The difference in these distributions, specifically the fact the they are more peaked for the M_2 case, is due to how the pressure profile is treated early in time. The posteriors for the peak pressures, which are not common between the two models, are shown in Fig. 4.4.

Figure 4.5, displaying pair-wise correlations between parameters, shows a strong correlation between $\dot{M}$, v_{e}, and γ_{g}, which is physically intuitive because the trajectory of the shell is set by a balance between the outward pressure from the gas (determined by γ_{g}) and the ablation pressure (determined by a combination of $\dot{M}$ and v_{e}). It was shown in Fig. 4.2 that M_2 is better at constraining the early-time pressure profiles and therefore would have less uncertainty in the correlated parameters, $\dot{M}$ and v_{e}, leading to more peaked distributions.

Another benefit of constructing the full-posteriors and examining pair-wise correlations is the opportunity to identify methods of constraining otherwise difficult to measure variables [56]. Since $\dot{M}$ and v_{e} are tightly correlated, the measurement of either the mass ablation rate or the exhaust velocity of the ablated material would tightly constrain the other value. Likewise, a measurement of either of these

would also be very constraining of the pressure exerted on the shell by the fuel
or, conversely, a measurement of the pressure exerted on the shell would be very
constraining on the mass ablation rate and exhaust velocity. Examining one self-
consistent model of the entire experimental system provides insights that would
otherwise be difficult to identify (although in retrospect seem obvious).

Given the full parameter distributions from the sampling the PPDs for the
derived quantities such as pressure and trajectory can be constructed. The exper-
imentally inferred shell trajectory and temporal pressure profile at the fuel shell
interface and ablation front, Figs. 4.6(a), 4.6(b) and Figs. 4.6(c), are a direct
result of the model inference. The trajectory (a) and ablation pressure (c) are
both tightly constrained, at the 5% and 10% levels respectively. Pressure is a
key quantity that characterizes an HED system (as it is the measure of energy
density), and specifically the ablation pressure is a measure of how efficiently laser
energy couples into the converging shell. Ablation pressure is usually measured
in either planar geometry [106] or inferred from hydrodynamics codes in spherical
geometry [107], in both cases the utility for testing the coupling models for implo-
sions is limited. These particular measurements are but one example of the utility
provided by the richness and complexity of the results derived from this analysis
method.

The pressure profile in Fig. 4.6(b) shows a peak pressure of $2.2^{+0.7}_{-1.0}$ Gbar cor-
responding to the outgoing shock wave hitting the shell. The pressures measured
here exceeds the energy density defined by binding energy of core electrons and
the volume of their orbitals (≈ 500 Mbar for Si), meaning if there are still bound
electrons (very likely prior to the return shock hitting the shell), their orbitals
will be highly perturbed by neighboring atoms leading to complex collective be-
havior [108]. Beyond the direct pressure effects that may occur, measuring the
pressure profile at the fuel shell interface, and specifically the pressure when the
shock reaches the interface, is interesting for two reasons: (1) The direct mea-
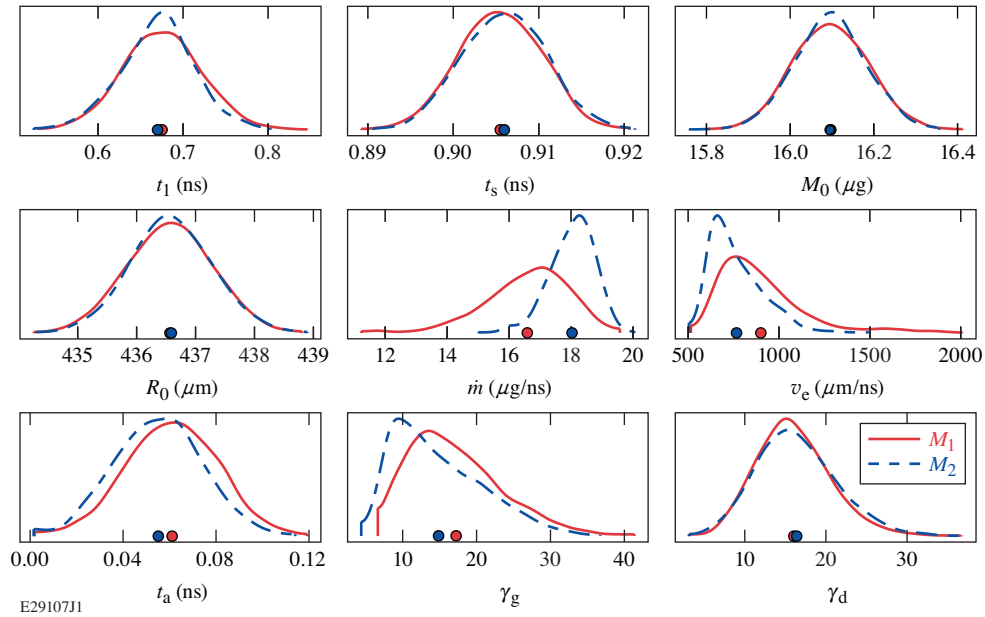
Figure 4.3: The posterior probability density distributions resulting from the MCMC sampling for the nine parameters that are common to both model M_1 (red) and M_2 (blue). The mean values of each distribution are given by the points on the bottom axis. The only parameters with a significant deviation are $\dot{M}$ and v_e, due to how they are related to the different pressure profiles used between the models. Originally published in reference [2].
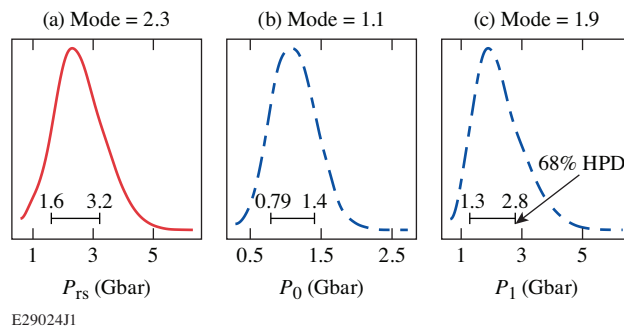
Figure 4.4: The posterior probability density distributions resulting from the MCMC sampling for the three different pressure parameters, P_{rs} of M_1 (red curve) and P_0 and P_1 of M_2 (blue curve). Also shown are the 68% HPD intervals which denote the shortest interval that contains 68.3% of the probability in the distribution and the values of the mode (peak) of the distributions. The values of P_{rs} and P_1 can both be interpreted as the pressure of the shock wave when it interacts with the shell material and P_0 can be interpreted as the pressure just before the shock reaches the shell in the two-pressure model (M_2). Originally published in reference [2].

E29025J1
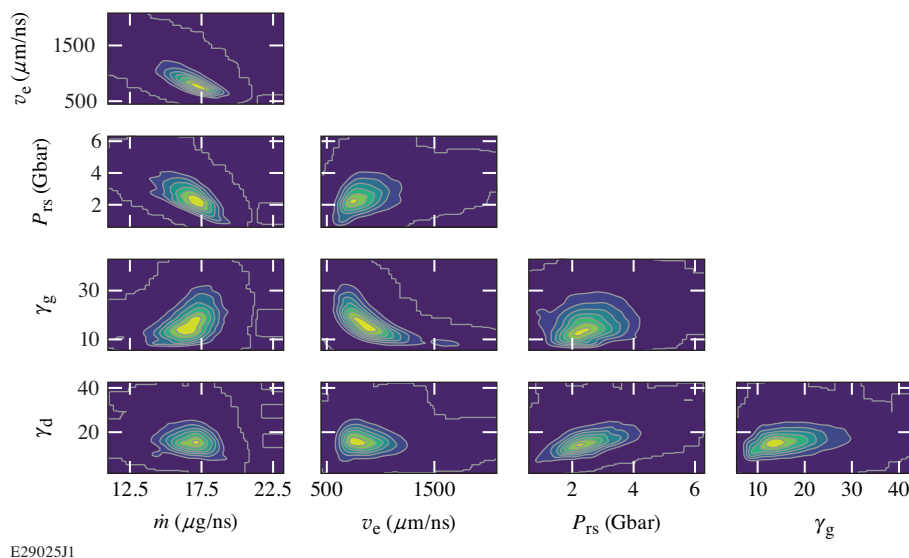
Figure 4.5:   Kernel density estimate of the pair-wise posterior distributions of parameters without strong prior information. Only the pressure parameter from M_1 is shown, P_{rs}, as the information is redundant for the other pressure parameters. Pair-wise correlations give insight into physical connections between variables and show how one variable can be constrained through measurement of another. An example is the negative correlation between $\dot{M}$ and v_e, meaning that a constraint of the exhaust velocity would greatly constrain the mass ablation rate in a laser-driven shell experiment. These types of connections can offer insight into how to constrain otherwise difficult to measure quantities. Originally published in reference [2].

surement of pressure is one of the most challenging aspects of making an absolute equation-of-state measurement, especially at gigabar conditions, and (2) in traditional (compressive) ICF implosions, the fuel is generally regarded as isobaric, so a measurement of the pressure at the fuel shell interface gives the pressure of the entire fuel.

In addition to the pressure profiles, the use of a self-consistent mechanical model for the shell gives insight into how energy is partitioned throughout the experiment. The kinetic energy of the imploding shell follows from the velocity of the shell [calculated when solving Eq. 4.1] and the mass of the shell, $KE = 0.5Mv^2$, and the work done on the fuel by the shell follows from the trajectory of the shell and the pressure profile at the interface. The work, dW, at a given time is equal to the change in volume, dV, of the fuel (given by the position of the shell) multiplied
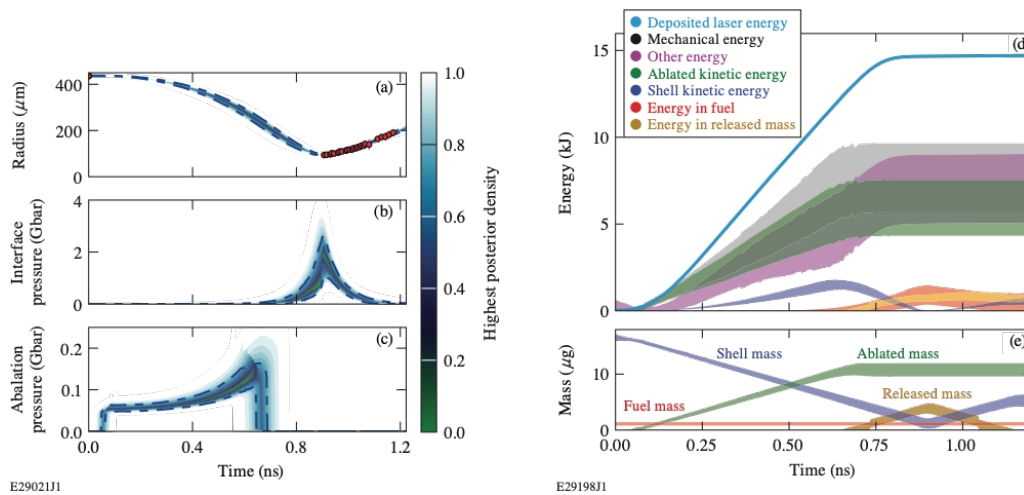
Figure 4.6: The inferred (a) shell trajectory, (b) pressure at fuel shell interface, and (c) ablation pressure resulting from Bayesian parameter estimation based on the experimentally measured data (red points on the left). Color bar shows highest posterior density intervals (HPD's) for each quantity with the 68.3% credible interval given by the dashed line in each. On the right, (a) 68.3% credible intervals for the different energy components within the model. The energy components include shell kinetic energy (dark blue shading), total fuel energy (red shading), shell kinetic energy that does not shading), and ablated kinetic energy (green shading). Also shown is the total mechanical energy in the model (gray shading), the laser energy deposited (light blue shading), and the difference (magenta shading) being a measure of non-mechanical energy in the system including internal energy of the corona and shell, radiation losses, and uncoupled laser energy. The mechanical energy of the system accounts for approximately half of the total incident laser energy, but of that only about 10% contributes to doing work on the fuel. (b) Mass credible intervals from the model including the shell mass (dark blue shading), ablated mass (green shading), the released mass (gold shading), and the fuel mass (red shading) as a function of time. Originally published in reference [3].

by the pressure, P, at the boundary,

$$dW = PdV. \tag{4.7}$$

the total work done on the fuel and, assuming adiabatic compression, the total energy of the fuel, follows from integrating the work. There are additional forms of mechanical energy modeled and there are additional forms of energy not accounted for by the model, all of which are presented in Fig. 4.6(d). The solid blue line is the laser energy as a function of time, from integrating the measured on-shot power. The shaded regions represent the highest posterior density intervals with 68.3% of the probability for each of the energy components. Components constrained in the model include the shell kinetic energy (dark blue shading), the energy in the fuel (red shading), the kinetic energy of the ablated mass (green), and the kinetic energy of the shell which does not do work on the fuel due to material release (gold shading). The sum of these components (gray shading) represent the total mechanical energy in the system. The remaining difference between the mechanical energy and the total laser energy (magenta shading) represents all of the different energy sinks that are not captured in the model. These components include internal energy of the corona and shell, radiation losses, and uncoupled laser energy.

The mechanical energy of the system plateaus prior to the laser energy, showing the time when the shell decouples from the ablation surface. At this point, additional laser energy does not increase the kinetic energy of the shell and does not contribute to adding energy to the fuel. This point coincides with the peak of the kinetic energy of the shell, which is an important metric for the performance of ICF implosions, although it is rarely directly measured [109, 110]. Additional laser energy deposited after this point likely stays in the already ablated mass in the form of thermal energy. Although about half of the incident laser energy goes

into mechanical energy of the system, only about 10% of this energy ends up in the fuel. All of the shell mass does not contribute to doing work on fuel [111], demonstrated in Fig. 4.6(e) where the different mass components are shown as a function of time.

The mass that does work on the fuel is the shell mass, about 60% of which is ablated by the time the laser turns off, after which the mass from the shell begins to release. This released mass also does not do work on the fuel. Ultimately the shell changes direction when the pressure from the fuel is sufficiently high, at which point released mass is recaptured as the shell moves out.

Previous measurements of mechanical energy and mass remaining in implosion experiments rely on backlit radiography techniques [110, 112], which are perturbative to the system and require the removal of drive beams reducing symmetry. They also often make use of hydrodynamics codes to infer system quantities making uncertainty analysis challenging [56, 73, 109, 113]. The method developed here provides the peak kinetic energy of the shell, the complete time history of the kinetic energy of the shell, and the work done on the fuel in a non-perturbative, in-situ measurement. The analysis technique provides a method for gaining quantitative insight from integrated HED measurements that was previously not possible.

To provide perspective, Fig. 4.7 shows a temperature-density diagram and a series of isobars (curves of constant pressure) corresponding to other relevant HED regimes such as 1 Mbar, the top pressure achieved in static compression experiments (with some exceptions)[114]; 50 Mbar, the top pressures measured in planar dynamic experiments [33];2.2 Gbar, the highest pressure measured in this experiment; and 300 Gbar, the pressure predicted to be in the core of the sun [115] and the highest predicted pressures in HED experiments [109, 116]. The orange-yellow color map shows the modeled temperature and density states as functions of radius within the solar interior [115]. The green-yellow colormap shows the
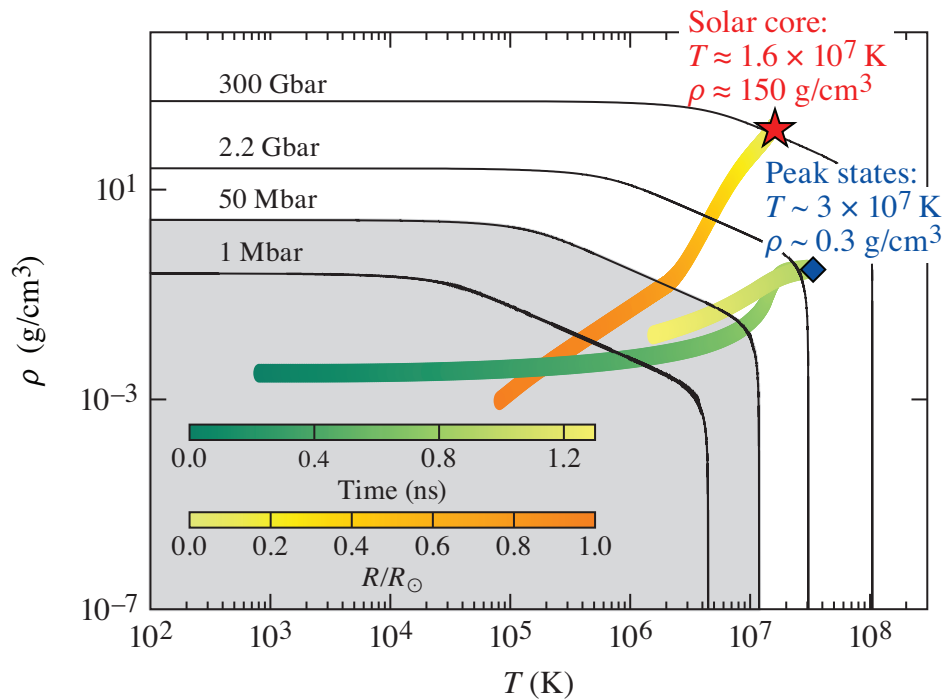
E29199J1

Figure 4.7: A temperature-density diagram showing four isobars (black curves), predicted states found in the solar interior as a function of solar radius (orange color scale) and the states found in the fuel during the experiment presented here assuming an ideal equation of state. The gray shaded region is where most HED experimental measurements are historically made, generally below 50 Mbar. Originally published in reference [3].

temperature and density states of the fuel in this experiment as functions of time derived from assuming a fully ionized ideal equation of state and conservation of mass using the trajectory of shell to determine fuel volume and the pressure at the interface, treating the fuel as isobaric, a reasonable approximation (due to the high temperatures, $> 10^6$ K, leading to high sound speeds) despite the spatial gradients likely within the temperature and density. This provides a useful illustration of the average temperature and density states within the fuel given the measured energy deposited within the fuel. Generally, as seen here, convergent HED systems reach pressures relevant to solar interiors but through higher temperatures and lower densities, although experimental designs can be tuned to achieve densities more relevant to stellar interiors.

In summary, the interaction of a laser-driven glass shell with a gigabar rebounding shock wave was studied using Bayesian inference and *in-situ* x-ray self-emission imaging. The peak pressure achieved by the shock wave was $2.2^{+0.7}_{-1.0}$ Gbar, higher than any previous mechanical measurement of a shock wave strength. The measurement of ablation pressure and shell trajectory can both be used to test key physics used in implosion modeling and the full temporal history of the kinetic energy of the shell provides insight into both the efficiency of laser conversion into mechanical energy and ultimately into the work done on the fuel. The implications of these measurements are far reaching; the possibility of absolute equation-of-state measurements using a mechanical measurement of pressure [68], diagnosing the conditions within implosions for studies of atomic spectroscopy [78], fundamental nuclear science under extreme thermodynamic conditions [117], and more robust methods for quantifying the performance of ICF implosions [56, 73, 109, 113]. The numerous results presented here demonstrate the richness of information that is available from Bayesian inference of integrated data from convergent HED experiments.

Chapter 5

Thick Shell Modelling

Portions of this chapter are reproduced from [**J.J. Ruby**, J.A. Gaffney, J.R. Rygg, Y. Ping, and G.W. Collins. High-energy-density-physics measurements in implosions using Bayesian inference. *Physics of Plasmas*, 032703(28), 2021], with the permission of AIP Publishing.

As stated in the previous chapter conducting synthetic experiments is not only valuable for *post fact* analysis development but also for pre-experimental design and decision making. There is a strong argument to be made that performing synthetic experiments and developing an analysis process before conducting an experiment is the most valuable application of these tools because of the insight it provides in identifying which quantities from an experiment are informed by which measurements and whether those measurements are feasible. This chapter presents an example of this process for a thick-shell compressive target as described in chapter 3.

Targets with significant compression from the inertia of the shell material are well studied [57, 80], primarily due to efforts made in ICF and in particular, producing experiments that generate significant amounts of fusion energy [69, 74, 118]. In this work, a subset of compressive implosions is considered, specifically with the goal of being as robust against 3-D effects as possible and therefore explicable through the lens of a radially symmetric 1-D model. The highest-performing ICF implosions require high implosion velocities and low shell masses,
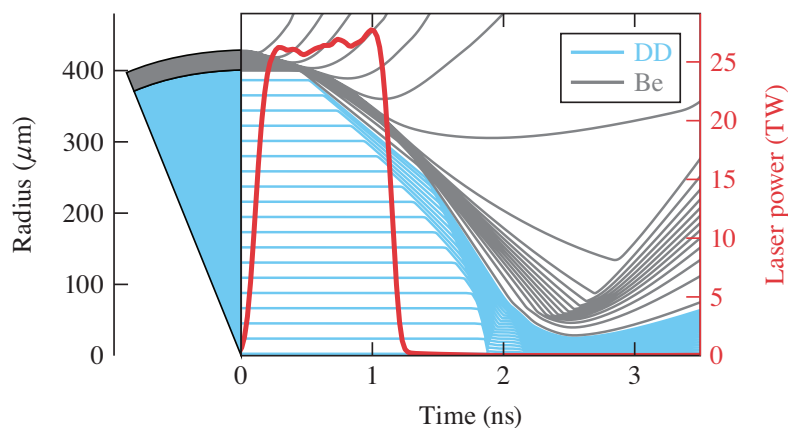
E29455J1

Figure 5.1:   Lagrangian particle trajectories for the shell material (grey) and gas (blue) in the simulated target. Also shown is the laser pulse (red) used to drive the target. On the left a wedge of the target is shown for context. Originally published in reference [4].

leading to high convergence and significant perturbation growth [119], while the implosions discussed here use thicker shells and lower implosion velocities and higher entropy states (driven by a single strong shock) in order to emphasize the 1-D symmetry of the system.

The primary mode of energy transfer into the fuel in these experiments comes from kinetic energy transfer from the high inertia shell as it slows down and compresses the fuel. Unlike the shock systems, where the states are established by an evolving converging and diverging shock wave, the dynamics of energy transfer in the compressive regime make electronic thermal conductivity and radiative energy losses important factors in the overall evolution of the states that are created [57, 72, 73, 80, 120] implying that the measurements from implosion platforms are sensitive to the details of thermal conductivity and radiative properties. Although the targets discussed here firmly exist in either the shock or compression-dominated regime there is no binary transition between the two but rather a spectrum of targets that share the qualities (and complexities) of both types of targets.

Here the 1-D Lagrangian hydrodynamics code $LILAC$ [75] is again used as the

more complete physics model to produce the synthetic experiment. The simulated system includes a $30 - \mu$m beryllium shell filled with 15 atm. of D_2 gas and has an outer diameter of $860 - \mu$m. This target is driven with 27 kJ of UV laser light in a 1-ns square pulse. The laser pulse and target are shown in Fig. 5.1 along with Lagrangian zone trajectories for the fuel and shell. The details of this target were chosen to promote as uniform an implosion as possible. A thick shell driven with a single strong shock is a "high-adiabat" [72, 80, 116] implosion, robust to hydrodynamic perturbations.

5.1   Synthetic Measurements

The simulation output includes the thermodynamic states (temperature, density, pressure, etc.) in each zone, and these are used to calculate the amount of x-ray self-emission (Eq. 3.1) and neutron self-emission (Eq. 3.10 with the reactivity from [84]). These quantities are then used to produce synthetic measurements based on typical implosion diagnostics, in particular time-gated radial x-ray profile measurements (such as would be measured by an x-ray framing camera [38]), time-resolved x-ray emission with multiple different spectral channels (as would be measure by multiple diagnostics [95, 121, 122]), the temporal history of the neutron production, neutron spectrum, and neutron yield, all of which are standard measurements in ICF experiments [87, 96]. These are "idealized" synthetic data, meaning an attempt was made to account for the instrument response functions for each measurement and typical uncertainties were used for each but no attempt was made at simulating typical background signals or other noise sources associated with each measurement. Additionally, the spectral and temporal channels were chosen such that sources of emission other than the hot spot, such as xrays from the shell material either during the laser drive or when the hot spot is assembled, are ignored. This is a plausible set of measurements, but care must be taken
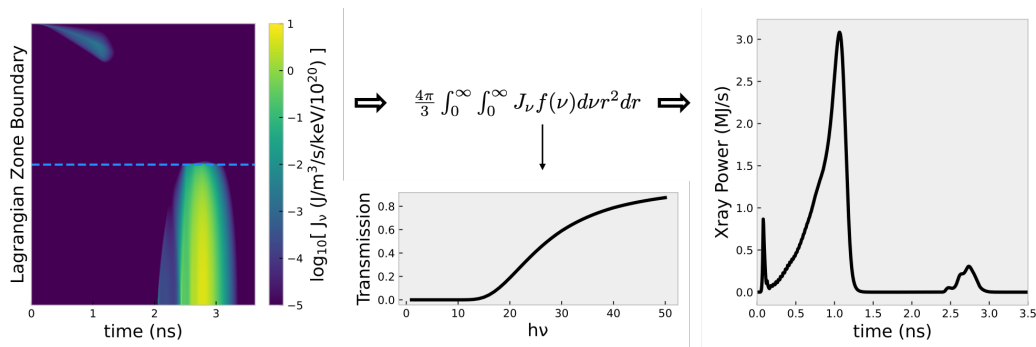
Figure 5.2: An example of producing synthetic measurements showing the (left) emission in each zone calculated from the hydrocode output at a particular wavelength, (middle) the integral used to calculate the spectrally integrated x-ray power through a particular spectral filter with transmission given below, and (right) the resulting x-ray power as a function of time. There is a large peak in the x-ray power in early time corresponding to emission from the hot plasma created While the laser is on and a peak later in time corresponding to the hot-spot emission of interest.

to determine the exact photometrics of these measurements prior to performing an experiment.

Figure 5.2 shows an example of calculating synthetic data from the *LILAC* output for the time resolved x-ray emission. In this case the x-ray emission generated in each Lagrangian zone is calculated and then integrated over the volume and spectrum to produce the x-ray power as a function of time. The integral over the spectrum includes a transmission function corresponding to the spectral response of the detector. Not shown in the figure is a final step of convolving the output with the temporal response of a particular detector to mimic the final measured signal.

The synthetic data (the right most plot in Fig. 5.2) shows a large peak early in time that corresponds to coronal emission from when the laser is incident on the target and a smaller peak later in time corresponding to the hot-spot emission of interest. These correspond to the signals seen in the left most plot in Fig. 5.2 in the top left and bottom right respectively. The hot-spot emission is much greater per unit volume but is a much smaller volume than the coronal emission meaning

that in terms of total x-ray energy emitted the corona is a few times brighter, meaning the diagnostics used to measure the hot-spot emission must be able to distinguish between these two signals temporally, spatially, or spectrally. This is an important finding that needs to be accounted for during the execution of an experiment.

5.2   Hot Spot Model

The reduced model used to describe the system is heavily influenced by previous work[57, 72, 73, 80, 120], the thermodynamic states of the hot spot are established through energy balance and conservation equations starting with a time-dependent parameterization of the hot spot energy, given by a Gaussian function

$$E(t) = E_0 e^{\frac{-(t-t_E)^2}{2\sigma_E^2}} \tag{5.1}$$

where E_0, t_E, and σ_E are the peak internal energy, time of peak energy, and width of the temporal energy profile, respectively. Each of these is a free parameter of the model.

The radial extent of the hot spot, R, is defined by a trajectory of constant acceleration,

$$R(t) = R_0 + \text{v}_0 t + \frac{1}{2} a_0 t^2 \tag{5.2}$$

and defines a time dependent hot spot volume

$$V(t) = \frac{4}{3} \pi R(t)^3. \tag{5.3}$$

The energy and volume then give the pressure

$$P(t) = \frac{E(t)}{c_V V(t)}, \tag{5.4}$$

assuming an ideal gas equation of state with a specific heat at constant volume, c_V.

A two-temperature fluid is assumed, with the electron temperature, T_e, and ion temperature T_i both having the same self-similar temperature profiles given by

$$T_{e,i}(r,t) = T_{e,i}^0 T_r(r/R_{HS}) \tag{5.5}$$

where $T_{e,i}^0$ is the (electron,ion) temperature at $r = 0$ and R_{HS} is the boundary of the hot spot. Following from conservation of mass and an ideal gas equation of state we get the relationship

$$\frac{\dot{M}}{M} = \frac{\dot{E}}{E} - \frac{\dot{T^0}}{T^0}, \tag{5.6}$$

where $T^0 = \bar{Z}T_e^0 + T_i^0$ and $\bar{Z}$ is the average ionization state, $Z = 1$ in this case considering fully ionized hydrogen. Since the hot spot is defined by the fuel it is fixed mass so $\dot{M} = 0$ and

$$\frac{\dot{E}}{E} = \frac{\dot{T^0}}{T^0}. \tag{5.7}$$

Integrating Eq. (5.7), with the initial condition $T^0(t = t_0) = T^{00}$ gives $T^0(t) = \bar{Z}T_e^0(t) + T_i^0(t)$ but the individual central temperatures for electrons and ions are still unknown. The ideal equation of state allows the radial density distribution to be constructed from the radial temperature distributions,

$$\rho(r) = \frac{\bar{A}P}{N_A} \frac{1}{\bar{Z}T_e(r) + T_i(r)} \tag{5.8}$$

where $\bar{A}$ is the average atomic mass and N_A is Avogadro's number. The radial temperature profiles $T_{e,i}(r)$ follow from solving the two temperature heat conduction equation,

$$\frac{c_P P}{\bar{Z}T_e + T_i} \left(\bar{Z}\frac{\partial T_e}{\partial t} + \frac{\partial T_i}{\partial t} \right) = \frac{1}{r^2}\frac{\partial}{\partial r}\kappa_e r^2 \frac{\partial T_e}{\partial r} + \frac{1}{r^2}\frac{\partial}{\partial r}\kappa_i r^2 \frac{\partial T_i}{\partial r} \tag{5.9}$$

where $\kappa_{e,i}$ is the (electron,ion) thermal conductivity which combine to give the total conductivity,κ_0 as

$$\kappa = \bar{Z}\kappa_e + \kappa_i \tag{5.10}$$

and the total conductivity is assumed to be of the form

$$\kappa = \kappa_0 \left(\frac{\rho}{\rho_0}\right)^a \left(\frac{T}{T_0}\right)^b \tag{5.11}$$

where a and b are the conductivity exponents as established in Spitzer[11]. Combining Eqs. (5.8) - (5.10) and separating the temporal and spatial components leads to a coupled equation for the radial temperature profile, T_r, and the central temperatures, T_e^0 and T_i^0,

$$\frac{\partial}{\partial t}\left(\bar{Z}T_e^0 + T_i^0\right) =$$

$$\frac{\lambda}{1+\bar{Z}}\frac{\kappa_0}{\rho_0^a T_0^b \gamma}\left(\frac{\bar{A}}{N_A c_V}\right)^a \left(\frac{E}{V}\right)^{a-1}\frac{\bar{Z}(T_e^0)^{1+b} + (T_i^0)^{1+b}}{(\bar{Z}T_e^0 + T_i^0)^{a-1}} \tag{5.12}$$

with

$$\lambda = \frac{1}{r^2}\frac{\partial}{\partial r}r^2 T_r^{b-a}\frac{\partial T_r}{\partial r}. \tag{5.13}$$

Using the boundary conditions $T_r(r = 0) = 1$ and $T_r(r = R_{HS}) = \eta$ $(\eta < 1)$ the radial profile can be found as

$$T_r = \left[1 - \left(\frac{r}{R_{HS}}\right)^2\left(1 - \eta^{1+b-a}\right)\right]^{\frac{1}{1+b-a}}. \tag{5.14}$$

Now since $T^0(t)$ is known along with the radial terms for $T_{e,i}(r,t)$ all that remains is a relationship between T_i^0 and T_e^0 to close the system. This relationship can take any form, including the simplest case where $T_e^0 = T_i^0$, here the relationship

$$T_e^0 = T_i^0 - De^{-t/\tau} \tag{5.15}$$

is used, where D and τ are parameters of the model relating to the initial difference in the electron and ion temperatures and the rate at which they equilibrate, related to but not equal to the electron-ion coupling time scale [11, 80, 123].

At this point all of the thermodynamic variables can be constructed in space and time giving $P(t)$, $V(t)$, $T_e(r,t)$, $T_i(r,t)$, and $\rho(r,t)$. The quantities required to close the model are $E(t)$, $R_{HS}(t)$, T^{00}, $\eta(t)$, a, b, c_V, D, and τ. It should be noted that the boundary temperature $\eta(t)$ can be independent for both the electrons and ions, but in this work will be taken as the same value for the electrons and ions.

An obvious extension of this model is the inclusion of parameters that describe the shell, which would have kinetic energy related to the internal energy of the hot spot changing the parameterization of the trajectory of the hot spot size and which would contribute to the hotpot mass through conductive ablation, an important mechanism in ignition-scale implosions [72, 120]. In this case the situation is simplified by considering the hot spot as an independent system that is not necessarily closed, i.e. energy need not be conserved within the system.

5.3   Results of Bayesian Inference

The parameters of the reduced model are inferred using the synthetic data according to the same prescription in chapter 4, in particular using a gaussian likelihood function and an SMC sampler. Figure 5.3 shows the predicted distributions for a set of the simulated measurements based on a Monte Carlo sampling of the reduced model. The model is able to reproduce all of the measurements shown within the 68.7% credible intervals (shown by the blue dashed-dotted lines). The profiles that result from the sampling shown in Fig. 5.3 are shown in Fig. 5.4 along with the underlying simulation profiles. The predicted profiles from the reduced model show excellent agreement with the "true" profiles that from the underlying
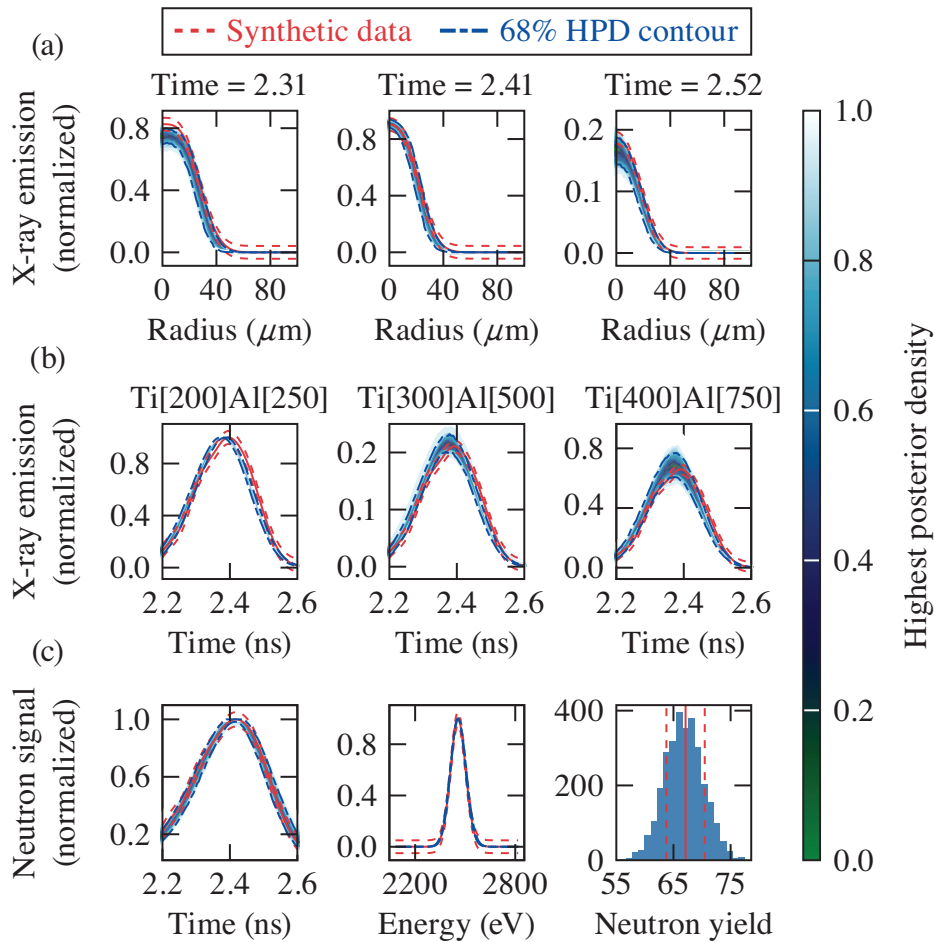
Figure 5.3:   A comparison of the predicted distributions (color map) for observations from Bayesian inference and the synthetic data generated (red solid) with normally distributed errors (dashed shows 1-σ), for (a) radial x-ray profiles at 3 (out of 16) times, (b) x-ray temporal histories in 3 different spectral channels, and (c) the neutron burn rate, spectrum, and yield (left to right). The inferred quantities are shown with a highest posterior density on the color scale. The inferred distributions from the model are able to reasonably reproduce the data across all measurements. Originally published in reference [4].
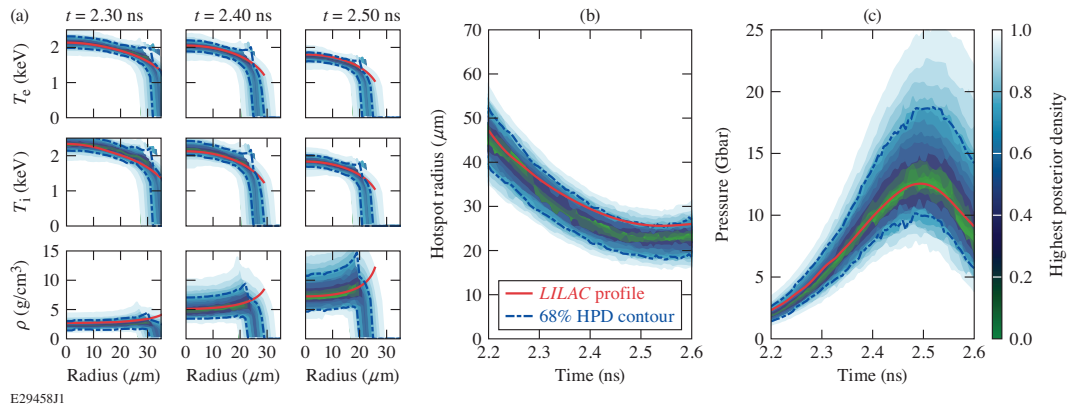
Figure 5.4:   A comparison between the inferred profiles from the reduced model, again showing highest posterior densities in the color map with green representing the most likely (median) prediction, and underlying profiles from the simulation (red) for (a) the radial dependence of electron temperature, ion temperature, and density at 3 different times, (b) the temporal history of the hot spot radius, and (c) the temporal profile of the hot spot pressure. The inferred quantities do an excellent job recovering the underlying profiles with the exception of the hot spot radius, which is under predicted throughout, leading to the truncation of the radial profiles in (a). Originally published in reference [4].

simulation for the electron and ion temperatures, density, and pressure in space and time. The exception is the hot-spot radius as a function of time, which is under-predicted for all times. This leads the the truncation of the radial profiles seen in Fig. 5.4(a). It is clear that, with respect to the third point above, the set of synthetic measurements presented here is enough to constrain the reduced model and reproduce the underlying profiles of interest.

An interesting next step is to investigate how the predictions vary with or without different measurements. This is presented in Fig. 5.5, where the results for the central electron and ion temperatures, central density, and hot-spot pressure are compared to the underlying simulation (red points) for three different times. Each box represents a different data set used, including the full data (green), excluding the neutron spectrum (cyan), excluding the spatial x-rays (blue), excluding the temporal x-rays (navy), and using a known hot spot radius for all times (purple). Leaving out the neutron spectrum has a minimal impact on the inferred profiles, meaning that the information contained in the neutron spectrum (in this

particular simulated implosion) is redundant with the other measurements. The neutron spectrum is generally considered constraining on the ion-temperature of the system [124, 125] but the information is likely redundant with the neutron yield (which is very sensitive to ion temperature through the reactivity) and the x-ray spectral information contained in the temporal x-ray history. Additionally the neutron spectrum is integrated over space and time leaving only a single integrated measurement of the temperature that is not very constraining of the temporal and spatial evolution of the temperatures. Conversely excluding either x-ray measurement results in a significant increase in uncertainty for the profiles, beyond the point of usefulness in most cases. The radial information contained in synthetic framing camera data is critical to setting the states within the hot spot and the temporal x-ray history helps break the degeneracy that exists within the neutron dataset. Finally, a dataset with a known hot spot radius significantly reduces the uncertainty on the inferred densities and pressures, with a much more modest reduction in uncertainty on the temperatures, although it does rectify the early truncation of the profiles seen in Fig. 5.4.

To demonstrate the degeneracy that arises in model parameters when a measurement is excluded, Fig. 5.6 (b) and (c) shows the pairwise posterior distributions for the time of peak energy, t_E and the hot spot radius at t_E, given by the trajectory parameters R_0, v_0, and a_0 along with histograms of the parameter values in Fig. 5.6 (a) and (d). The red distribution in (b) includes all of the measurements and the blue distribution in (c) excludes the framing camera measurements. The distribution without the framing camera shows that the these two parameters are strongly correlated, with a positive correlation coefficient, leading to very broad posterior distributions for both parameters in (a) and (d). The framing camera breaks this degeneracy resulting in a distributions with minimal correlations and much more narrow posterior distributions.

This result may be somewhat surprising because even without the framing

E29459J1
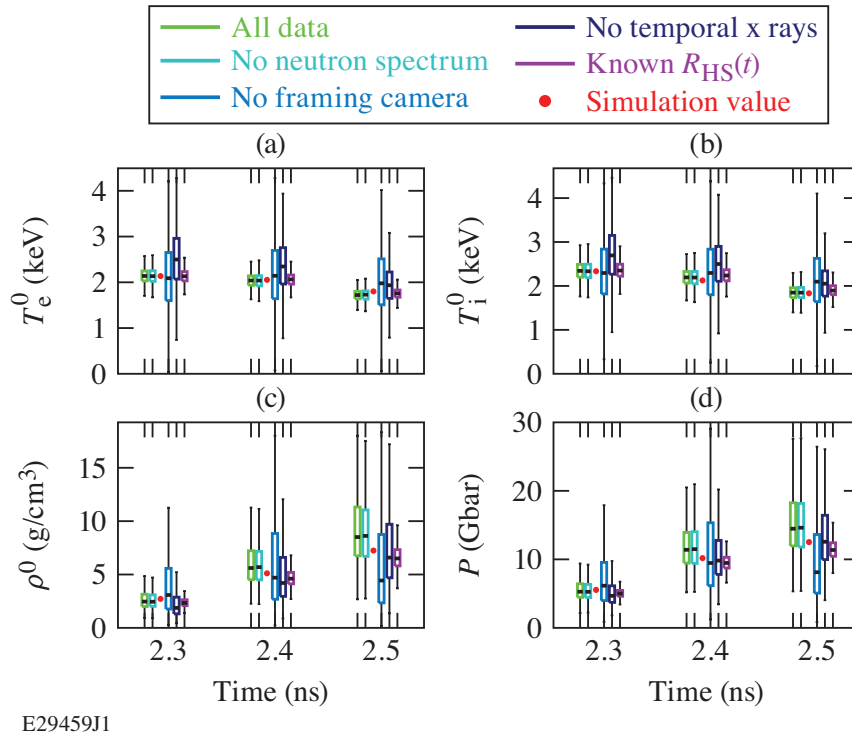
Figure 5.5:   A boxplot comparing the inferred thermodynamic parameters from the reduced model and the underlying values from the simulation (red) for (a) the central electron temperature, (b) central ion temperature, (c) central density, and (d) pressure at 3 different times. The different color boxes represent the results inferred using different datasets including the full data (green), excluding the neutron spectrum (cyan), excluding the x-ray radial data (blue), excluding the x-ray temporal data (navy), and using a known hot spot radius for all times (purple). The boxes represent the upper and lower quartiles of the inferred distributions and the bars show the full extent of the distributions. Originally published in reference [4].
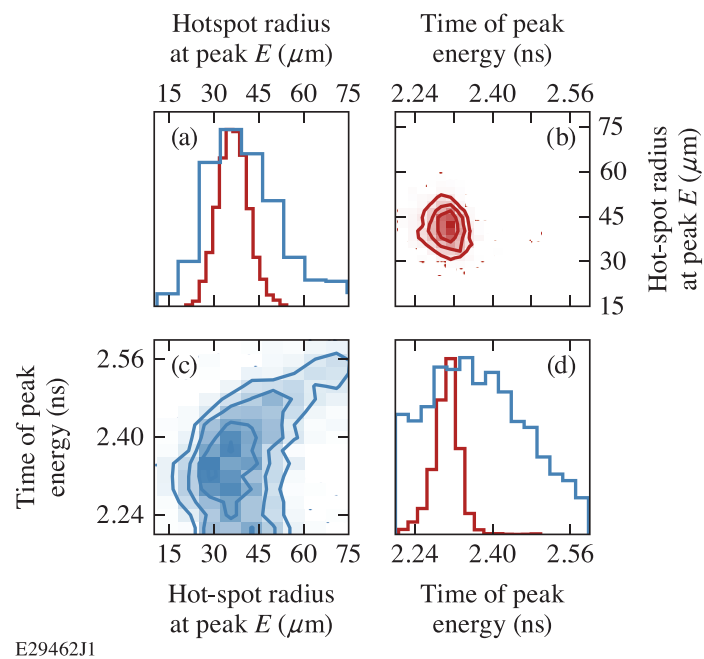
Figure 5.6:   Pairwise distribution for the time of peak energy, t_E, and hot spot radius at time of peak energy, $R_{HS}(t_E)$, showing (c) their strong correlation without the framing camera data and (b) how the degeneracy is broken when all of the measurements are used. The projected histograms for (a) the radius and (d) the time both show the effect of the using all the data (red) in narrowing the distributions from the case without the framing camera (blue). Note the axes in (b) are transposed from those in (c). Originally published in reference [4].

camera measurements there is still neutron and x-ray temporal measurements that may be expected to constrain the temporal history of the fuel internal energy, but seemingly do not. The degeneracy exists because both the x-ray and neutron yields depend on the energy of the hot spot and the volume of the hot spot (the energy density) meaning that the peak in emission does correspond to the peak in internal energy, but rather the peak in energy density which depends on the radius and energy and the degeneracy is broken with the time-gated radial measurements of emission from the framing camera.

Finally the ability to extract information about the thermal conductivity is presented in Fig. 5.7 which shows a boxplot, similar to Fig. 5.5, but for the conductivity exponent which depends on a combination of the temperature and density dependencies, b and a, respectively, following from Eq. 5.14. Since the temperature profile depends on this combination of parameters, and the emission profiles depend on the temperature profile, it is this quantity that is constrained. The underlying simulation made use of Spitzer conductivities [11], which have $a = 0$ and $b = 2.5$ so the quantity $(1 + b - a)^{-1} = 0.286$, shown with the red point in the figure. The conductivity exponent has a modest effect on the temperature profile, and this can be seen here where, despite the temperature profiles being well constrain by the measurements as shown in Fig. 5.4, the conductivity exponent has a fairly broad distribution in the best case resulting in $0.25\pm^{0.08}_{0.1}$ (median $\pm 68.7\%$ highest posterior density interval). The conductivity exponent under these conditions can be constrained at the few tens of percent level, future work is needed to investigate the necessary precision to distinguish between conductivity models and what, if any, additional measurements can produce a tighter constraint on the conductivity.
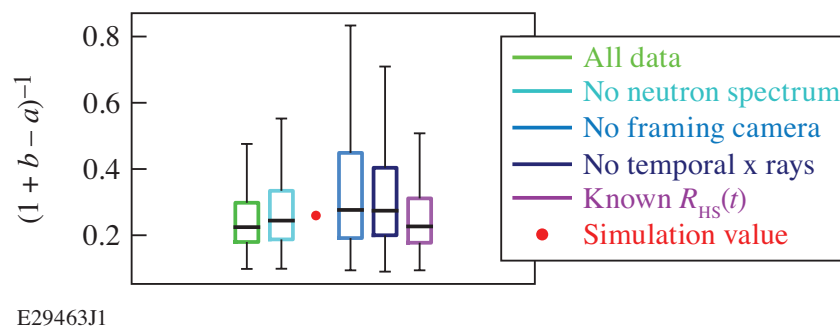
E29463J1

Figure 5.7:   A boxplot comparing the inferred conductivity exponent from the same data sets in Fig. 5.5 and the true exponent form the conductivity model used in the *LILAC* simulations (0.286 for $a = 0$ and $b = 2.5$) [11]. Even the models using the most data could only constrain the conductivity profile to within 10s of percent due them measurements being derived form the temperature profiles and the profiles' weak dependence on the conductivity exponent. Originally published in reference [4].

Chapter 6

Conclusions

Laser-driven implosion experiments can reach a wide variety of interesting high-energy-density conditions and there is great opportunity for discovery in these systems. Basic target design with a simple laser pulse shape is able to transition between interesting energy regimes — shock dominated and compression dominated — and within those regimes different types of transport physics as able to be emphasized depending on the initial conditions. There are a standard set of measurements able to be made in laser driven implosions and the understanding how the measurements are sensitive to different physical mechanisms is key to understanding the physics and measurements. Reduced models coupled with Bayesian inference give a straightforward way to explicitly state the assumptions of a particular analysis, and understand how the measurements are able to constrain the model of the system. Two examples of this process have been presented here, one in the shock dominated regime and one in the compression dominated regime.

In the shock dominated regime shows how a seemingly isolated measurement, a trajectory of a decompressing shell, can be used to characterize the energy balance of the implosion through out its entire history. This is a powerful result showing how integrated these implosion experiments are and how every stage of an implosion can potentially be leveraged to constrain relevant physics. Beyond the general premise, the mechanical measurement of a 2.2 Gbar shock wave in the absence of

assumptions about thermodynamic path or equation of state is an exciting step towards an absolute and path independent equation of state measurement at Gbar pressures.

The example using a thick shell implosion driven with a square pulse, shows that the thermodynamic profiles (temperature, density, pressure) of the assembled hot spot can be reconstructed in space and time using standard self-emission measurements of x-rays and neutrons. In addition it is shown that the neutron spectrum does not have much leverage on the spatial and temporal profiles of temperature, but time-gated spatial resolved x-rays measurements in combination with time-resolved and spectrally gated x-ray measurements are very constraining when used with neutron burn rate and yield measurements. This demonstrates the information contained in currently performed measurements and will hopefully inform the analysis and interpretation of future implosion experiments to include a self-consistent picture of all measurements.

This process presents a new modality for experimental design that allows an analysis pipeline to be built and tested prior to an experiment informing both experimental design and diagnostic decisions for the experiment. This process can be expanded to any number of systems and used both in the pursuit of inertial fusion ignition and understanding of fundamental HED physics.

Bibliography

[1] **J.J. Ruby**, J.R. Rygg, J.A. Gaffney, B. Bachmann, and G.W. Collins. A boundary condition for Guderley's converging shock problem. *Physics of Fluids*, 31(12), 2019.

[2] **J.J. Ruby**, J.R. Rygg, D.A. Chin, J.A. Gaffney, P.J. Adrian, D. Bishel, C.J. Forrest, V.Yu. Glebov, N.V. Kabadi, P.M. Nilson, Y. Ping, C. Stoeckl, and G.W. Collins. Constraining physical models at gigabar pressures. *Physical Review E*, 102(5):53210, 2020.

[3] **J.J. Ruby**, J.R. Rygg, D.A. Chin, J.A. Gaffney, P.J. Adrian, C.J. Forrest, V.Yu. Glebov, N.V. Kabadi, P.M. Nilson, Y. Ping, C. Stoeckl, and G.W. Collins. Energy Flow in Thin Shell Implosions and Explosions. *Physical Review Letters*, 125(21):215001, 2020.

[4] **J.J. Ruby**, J.A. Gaffney, J.R. Rygg, Y. Ping, and G.W. Collins. High-energy-density-physics measurements in implosions using Bayesian inference. *Physics of Plasmas*, 032703(28), 2021.

[5] F.J. Marshall, S.T. Ivancic, C. Mileham, P.M. Nilson, **J.J. Ruby**, C. Stoeckl, B.S. Scheiner, and M.J. Schmitt. High-Resolution X-Ray Radiography with Fresnel Zone Plates on the University of Rochester's OMEGA Laser Systems. *Review of Scientific Instruments*, 033701(92), 2021.

[6] B.J. Henderson, M.C. Marshall, T.R. Boehly, R. Paul, C.A. McCoy, S.X. Hu, D.N. Polsin, L.E. Crandall, M.F. Huff, D.A. Chin, **J.J. Ruby**, X. Gong, D.E. Fratanduono, J.H. Eggert, J.R. Rygg, and G.W. Collins. Shock-compressed silicon: Hugoniot and sound speed up to 2100 gpa. *Phys. Rev. B*, 103:094115, 2021.

[7] P. Hatfield, J.A. Gaffney, G.J. Anderson, S. Ali, L. Antonelli, S. Basegmez-du Pree, J. Cintrin, M. Fajardo, P. Knapp, B. Kettle, B. Kostowski, M. Macdonald, D. Mariscal, M. Matin, T. Nagayama, C. Palmer, J.L. Peterson, S. Rose, **J.J. Ruby**, C. Schneider, M. Streeter, W. Trickey, and B. Williams. The data-driven future of high energy density physics. *Nature*, in press, 2021.

[8] Omega laser facility, 2020.

[9] S. Gibson, D.D. Hickstein, M. Yurchak, R.; Ryazanov, D. Das, and G. Shih. Pyabel readme, 2019.

[10] C. E. Shannon. A Mathematical Theory of Communication. *Bell System Technical Journal*, 27(4):623–656, 1948.

[11] Lyman Spitzer. *Physics of fully ionized gases; 1st ed.* Internat. Sci. Tracts Phys. Astron. Interscience, New York, NY, 1956.

[12] Gilbert W. Collins. Matter at extreme energy density: Exotic solids to inertial fusion. APS-DPP, November 2018.

[13] National Research Council. *Frontiers in High Energy Density Physics: The X-Games of Contemporary Science.* The National Academies Press, Washington, DC, 2003.

[14] D. G. Hicks, T. R. Boehly, J. H. Eggert, J. E. Miller, P. M. Celliers, and G. W. Collins. Dissociation of liquid silica at high pressures and temperatures. *Physical Review Letters*, 97(2):3–6, 2006.

[15] D. N. Polsin, D. E. Fratanduono, J. R. Rygg, A. Lazicki, R. F. Smith, J. H. Eggert, M. C. Gregor, B. H. Henderson, J. A. Delettrez, R. G. Kraus, P. M. Celliers, F. Coppari, D. C. Swift, C. A. McCoy, C. T. Seagle, J. P. Davis, S. J. Burns, G. W. Collins, and T. R. Boehly. Measurement of Body-Centered-Cubic Aluminum at 475 GPa. *Physical Review Letters*, 119(17):1–5, 2017.

[16] S. X. Hu, V. V. Karasiev, V. Recoules, P. M. Nilson, N. Brouwer, and M. Torrent. Interspecies radiative transition in warm and superdense plasma mixtures. *Nature Communications*, 11(1):1–8, 2020.

[17] S. X. Hu, L. A. Collins, J. P. Colgan, V. N. Goncharov, and D. P. Kilcrease. Optical properties of highly compressed polystyrene: An ab initio study. *Physical Review B*, 96(14):1–11, 2017.

[18] A. S. Eddington. The internal constitution of the stars. *Nature*, 106(2653):14–20, 1920.

[19] Subrahmanyan Chandrasekhar. *An introduction to the study of stellar structure.* 1939.

[20] L. Meitner and O.R. Frisch. Disintegration of Uranium by Neutrons: a New Type of Nuclear Reaction. *Nature*, 143:239–240, 1939.

[21] O.R. Frisch. Physical Evidence for the Division of Heavy Nuclei under Neutron Bombardment. *Nature*, 143:276, 1939.

[22] H. Von Halban, F. Joliot, and L. Kowarski. Number of neutrons liberated in the nuclear fission of uranium, 1939.

[23] Richard Rhodes. *The making of the atomic bomb.* Simon and Schuster, New York, 1995.

[24] Yuri P Raizer and Yakov Boris Zel'dovich. *Physics of shock waves and high-temperature hydrodynamic phenomena.* Academic Press, New York, NY, 1967. Trans. from the Russian.

[25] John Nuckolls, Lowell Wood, Albert Thiessen, and George Zimmerman. Laser compression of matter to super-high densities: Thermonuclear (CTR) applications. *Nature*, 239(5368):139–142, 1972.

[26] Ho Kwang Mao, Xiao Jia Chen, Yang Ding, Bing Li, and Lin Wang. Solids, liquids, and gases under high pressure. *Reviews of Modern Physics*, 90(1):15007, 2018.

[27] Percy W. Bridgman. General survey of certain results in the field of high-pressure physics. *Nobel Lecture*, 1946.

[28] R. Paul Drake. High-energy-density physics. *Physics Today*, 63(6):28–33, 2010.

[29] Francis Birch. Elasticity and constitution of the Earth's interior. *Journal of Geophysical Research*, 57(2), 1952.

[30] D. D. Meyerhofer, J. Bromage, C. Dorrer, J. H. Kelly, B. E. Kruschwitz, S. J. Loucks, R. L. McCrory, S. F.B. Morse, J. F. Myatt, P. M. Nilson, J. Qiao, T. C. Sangster, C. Stoeckl, L. J. Waxer, and J. D. Zuegel. Performance of and initial results from the OMEGA EP Laser System. *Journal of Physics: Conference Series*, 244(PART 3), 2010.

[31] T. R. Boehly, D. L. Brown, R. S. Craxton, R. L. Keck, J. P. Knauer, J. H. Kelly, T. J. Kessler, S. A. Kumpan, S. J. Loucks, S. A. Letzring, F. J. Marshall, R. L. McCrory, S. F.B. Morse, W. Seka, J. M. Soures, and C. P. Verdon. Initial performance results of the OMEGA laser system. *Optics Communications*, 133(1-6):495–506, 1997.

[32] G. W. Collins, L. B. Da Silva, P. Celliers, D. M. Gold, M. E. Foord, R. J. Wallace, A. Ng, S. V. Weber, K. S. Budil, and R. Cauble. Measurements of the equation of state of deuterium at the fluid insulator-metal transition. *Science*, 281(5380):1178–1181, 1998.

[33] M. C. Marshall, A. E. Lazicki, D. Erskine, R. A. London, D. E. Fratanduono, P. M. Celliers, J. H. Eggert, F. Coppari, D. C. Swift, P. A. Sterne, H. D. Whitley, and J. Nilsen. Developing quartz and molybdenum as impedance-matching standards in the 100-Mbar regime. *Physical Review B*, 99(17):174101, 2019.

[34] P. M. Celliers, D. K. Bradley, G. W. Collins, D. G. Hicks, T. R. Boehly, and W. J. Armstrong. Line-imaging velocimeter for shock diagnostics at the OMEGA laser facility. *Review of Scientific Instruments*, 75(11):4916–4929, 2004.

[35] J. E. Miller, T. R. Boehly, A. Melchior, D. D. Meyerhofer, P. M. Celliers, J. H. Eggert, D. G. Hicks, C. M. Sorce, J. A. Oertel, and P. M. Emmel. Streaked optical pyrometer system for laser-driven shock-wave experiments on OMEGA. *Review of Scientific Instruments*, 78(3), 2007.

[36] Brian D. Ramsey, Robert A. Austin, and Rudolf Decher. Instrumentation for x-ray astronomy. *Space Science Reviews*, 69:139–204, 1994.

[37] J. D. Kilkenny, P. M. Bell, D. K. Bradley, D. L. Bleuel, J. A. Caggiano, E. L. Dewald, W. W. Hsing, D. H. Kalantar, R. L. Kauffman, D. J. Larson, J. D. Moody, D. H. Schneider, M. B. Schneider, D. A. Shaughnessy, R. T. Shelton, W. Stoeffl, K. Widmann, C. B. Yeamans, S. H. Batha, G. P. Grim, H. W. Herrmann, F. E. Merrill, R. J. Leeper, J. A. Oertel, T. C. Sangster, D. H. Edgell, M. Hohenberger, V. Yu Glebov, S. P. Regan, J. A. Frenje, M. Gatu-Johnson, R. D. Petrasso, H. G. Rinderknecht, A. B. Zylstra, G. W. Cooper, and C. Ruiz. The national ignition facility diagnostic set at the completion of the national ignition campaign, September 2012. *Fusion Science and Technology*, 69(1):420–451, 2016.

[38] J. D. Kilkenny. High speed proximity focused x-ray cameras. *Laser and Particle Beams*, 9(1):49–69, 1991.

[39] J. R. Rygg, J. H. Eggert, A. E. Lazicki, F. Coppari, J. A. Hawreliak, D. G. Hicks, R. F. Smith, C. M. Sorce, T. M. Uphaus, B. Yaakobi, and G. W. Collins. Powder diffraction from solids in the terapascal regime. *Review of Scientific Instruments*, 83(11), 2012.

[40] Marius Millot, Federica Coppari, J. Ryan Rygg, Antonio Correa Barrios, Sebastien Hamel, Damian C. Swift, and Jon H. Eggert. Nanosecond X-ray diffraction of shock-compressed superionic water ice. *Nature*, 569(7755):251–255, 2019.

[41] M. F. Kasim, T. P. Galligan, J. Topp-Mugglestone, G. Gregori, and S. M. Vinko. Inverse problem instabilities in large-scale modeling of matter in extreme conditions. *Physics of Plasmas*, 26(11), 2019.

[42] Simon R Arridge and John C Schotland. Optical tomography: forward and inverse problems. *Inverse Problems*, 25(12):123010, dec 2009.

[43] D. G. Hicks, B. K. Spears, D. G. Braun, R. E. Olson, C. M. Sorce, P. M. Celliers, G. W. Collins, and O. L. Landen. Streaked radiography measurements of convergent ablator performance. *Review of Scientific Instruments*, 81(10), 2010.

[44] D. G. Hicks, B. K. Spears, D. G. Braun, R. E. Olson, C. M. Sorce, P. M. Celliers, G. W. Collins, and O. L. Landen. Convergent ablator performance measurements. *Physics of Plasmas*, 17(10), 2010.

[45] A. F. T. Leong, E. Asare, R. Rex, X. H. Xiao, K. T. Ramesh, and T. C. Hufnagel. Determination of size distributions of non-spherical pores or particles from single x-ray phase contrast images. *Optics Express*, 27(12):17322, 2019.

[46] Damian C. Swift, Andrea L. Kritcher, James A. Hawreliak, Amy Lazicki, Andrew Macphee, Benjamin Bachmann, Tilo Döppner, Joseph Nilsen, Gilbert W. Collins, Siegfried Glenzer, Stephen D. Rothman, Dominik Kraus, and Roger W. Falcone. Absolute Hugoniot measurements from a spherically convergent shock using x-ray radiography. *Review of Scientific Instruments*, 89(5), 2018.

[47] Udo Von Toussaint. Bayesian inference in physics. *Reviews of Modern Physics*, 83(3):943–999, 2011.

[48] Roberto Trotta. Bayes in the sky: Bayesian inference and model selection in cosmology. *Contemporary Physics*, 49(2):71–104, 2008.

[49] D S Sivia and John Skilling. *Data analysis: a Bayesian tutorial. For Scientists and Engineers; 2nd ed.* Oxford science publications. Oxford Univ. Press, Oxford, 2006.

[50] E. T. Jaynes. *Probability theory: The logic of science.* Cambridge University Press, Cambridge, 2003.

[51] Arnaud Doucet, Nando de Freitas, and Neil Gordon. *An Introduction to Sequential Monte Carlo Methods*, pages 3–14. Springer New York, New York, NY, 2001.

[52] John Salvatier, Thomas V. Wiecki, and Christopher Fonnesbeck. Probabilistic programming in python using PyMC3. *PeerJ Computer Science*, 2:e55, apr 2016.

[53] Robert E. Kass and Adrian E. Raftery. Bayes factors. *Journal of the American Statistical Association*, 90(430):773–795, 1995.

[54] Andrew Gelman, Jessica Hwang, and Aki Vehtari. Understanding predictive information criteria for Bayesian models. *Statistics and Computing*, 24(6):997–1016, 2014.

[55] K D Humbird, J L Peterson, B K Spears, and R G Mcclarren. Fusion Experiments. 48(1):61–70, 2020.

[56] Jim A. Gaffney, Scott T. Brandon, Kelli D. Humbird, Michael K.G. Kruse, Ryan C. Nora, J. Luc Peterson, and Brian K. Spears. Making inertial confinement fusion models more predictive. *Physics of Plasmas*, 26(8), 2019.

[57] John D. Lindl, Peter Amendt, Richard L. Berger, S. Gail Glendinning, Siegfried H. Glenzer, Steven W. Haan, Robert L. Kauffman, Otto L. Landen, and Laurence J. Suter. The physics basis for ignition using indirect-drive

targets on the National Ignition Facility. *Physics of Plasmas*, 11(2):339–491, 2004.

[58] J. R. Rygg, F. H. Séguin, C. K. Li, J. A. Frenje, M. J.E. Manuel, R. D. Petrasso, R. Betti, J. A. Delettrez, O. V. Gotchev, J. P. Knauer, D. D. Meyerhofer, F. J. Marshall, C. Stoeckl, and W. Theobald. Proton radiography of inertial fusion implosions. *Science*, 319(5867):1223–1225, 2008.

[59] Charles B Yeamans and Brent E Blue. National Ignition Facility Neutron Sources. *Llnl-Conf-739397*, pages 1–4, 2018.

[60] Barukh Yaakobi, Frederic J. Marshall, Thomas R. Boehly, Richard P. J. Town, and David D. Meyerhofer. Extended x-ray absorption fine-structure experiments with a laser-imploded target as a radiation source. *Journal of the Optical Society of America B*, 20(1):238, 2003.

[61] B. R. Maddox, H. S. Park, B. A. Remington, C. Chen, S. Chen, S. T. Prisbrey, A. Comley, C. A. Back, C. Szabo, J. F. Seely, U. Feldman, L. T. Hudson, S. Seltzer, M. J. Haugh, and Z. Ali. Absolute measurements of x-ray backlighter sources at energies above 10 keV. *Physics of Plasmas*, 18(5), 2011.

[62] F. Coppari, D. B. Thorn, G. E. Kemp, R. S. Craxton, E. M. Garcia, Y. Ping, J. H. Eggert, and M. B. Schneider. X-ray source development for EXAFS measurements on the National Ignition Facility. *Review of Scientific Instruments*, 88(8), 2017.

[63] A. Krygier, F. Coppari, G. E. Kemp, D. B. Thorn, R. S. Craxton, J. H. Eggert, E. M. Garcia, J. M. McNaney, H. S. Park, Y. Ping, B. A. Remington, and M. B. Schneider. Developing a high-flux, high-energy continuum backlighter for extended x-ray absorption fine structure measurements at the National Ignition Facility. *Review of Scientific Instruments*, 89(10), 2018.

[64] Yun Hu, Shaoen Jiang, Jiyan Zhang, Quanxi Xue, Zhebin Wang, and Qing Ye. X-ray source improvements for EXAFS measurement on SGIII prototype facility. *AIP Advances*, 10(5), 2020.

[65] Y. P. Opachich, R. F. Heeter, M. A. Barrios, E. M. Garcia, R. S. Craxton, J. A. King, D. A. Liedahl, P. W. McKenty, M. B. Schneider, M. J. May, R. Zhang, P. W. Ross, J. L. Kline, A. S. Moore, J. L. Weaver, K. A. Flippo, and T. S. Perry. Capsule implosions for continuum x-ray backlighting of opacity samples at the National Ignition Facility. *Physics of Plasmas*, 24(6), 2017.

[66] A. L. Kritcher, T. Döppner, D. Swift, J. Hawreliak, G. Collins, J. Nilsen, B. Bachmann, E. Dewald, D. Strozzi, S. Felker, O. L. Landen, O. Jones, C. Thomas, J. Hammer, C. Keane, H. J. Lee, S. H. Glenzer, S. Rothman, D. Chapman, D. Kraus, P. Neumayer, and R. W. Falcone. Probing matter

at Gbar pressures at the NIF. *High Energy Density Physics*, 10(1):27–34, 2014.

[67] Andrea L. Kritcher, Damian C. Swift, Tilo Döppner, Benjamin Bachmann, Lorin X. Benedict, Gilbert W. Collins, Jonathan L. DuBois, Fred Elsner, Gilles Fontaine, Jim A. Gaffney, Sebastien Hamel, Amy Lazicki, Walter R. Johnson, Natalie Kostinski, Dominik Kraus, Michael J. MacDonald, Brian Maddox, Madison E. Martin, Paul Neumayer, Abbas Nikroo, Joseph Nilsen, Bruce A. Remington, Didier Saumon, Phillip A. Sterne, Wendi Sweet, Alfredo A. Correa, Heather D. Whitley, Roger W. Falcone, and Siegfried H. Glenzer. A measurement of the equation of state of carbon envelopes of white dwarfs. *Nature*, 584(7819):51–54, 2020.

[68] T. Döppner, D. C. Swift, A. L. Kritcher, B. Bachmann, G. W. Collins, D. A. Chapman, J. Hawreliak, D. Kraus, J. Nilsen, S. Rothman, L. X. Benedict, E. Dewald, D. E. Fratanduono, J. A. Gaffney, S. H. Glenzer, S. Hamel, O. L. Landen, H. J. Lee, S. Lepape, T. Ma, M. J. Macdonald, A. G. Macphee, D. Milathianaki, M. Millot, P. Neumayer, P. A. Sterne, R. Tommasini, and R. W. Falcone. Absolute Equation-of-State Measurement for Polystyrene from 25 to 60 Mbar Using a Spherically Converging Shock Wave. *Physical Review Letters*, 121(2):25001, 2018.

[69] R. S. Craxton, K. S. Anderson, T. R. Boehly, V. N. Goncharov, D. R. Harding, J. P. Knauer, R. L. McCrory, P. W. McKenty, D. D. Meyerhofer, J. F. Myatt, A. J. Schmitt, J. D. Sethian, R. W. Short, S. Skupsky, W. Theobald, W. L. Kruer, K. Tanaka, R. Betti, T. J.B. Collins, J. A. Delettrez, S. X. Hu, J. A. Marozas, A. V. Maximov, D. T. Michel, P. B. Radha, S. P. Regan, T. C. Sangster, W. Seka, A. A. Solodov, J. M. Soures, C. Stoeckl, and J. D. Zuegel. Direct-drive inertial confinement fusion: A review. *Physics of Plasmas*, 22(11):0–153, 2015.

[70] V. Gopalaswamy, R. Betti, J. P. Knauer, N. Luciani, D. Patel, K. M. Woo, A. Bose, I. V. Igumenshchev, E. M. Campbell, K. S. Anderson, K. A. Bauer, M. J. Bonino, D. Cao, A. R. Christopherson, G. W. Collins, T. J.B. Collins, J. R. Davies, J. A. Delettrez, D. H. Edgell, R. Epstein, C. J. Forrest, D. H. Froula, V. Y. Glebov, V. N. Goncharov, D. R. Harding, S. X. Hu, D. W. Jacobs-Perkins, R. T. Janezic, J. H. Kelly, O. M. Mannion, A. Maximov, F. J. Marshall, D. T. Michel, S. Miller, S. F.B. Morse, J. Palastro, J. Peebles, P. B. Radha, S. P. Regan, S. Sampat, T. C. Sangster, A. B. Sefkow, W. Seka, R. C. Shah, W. T. Shmyada, A. Shvydky, C. Stoeckl, A. A. Solodov, W. Theobald, J. D. Zuegel, M. Gatu Johnson, R. D. Petrasso, C. K. Li, and J. A. Frenje. Tripled yield in direct-drive laser fusion through statistical modelling. *Nature*, 565(7741):581–586, 2019.

[71] G. Guderley. Starke kugelige und zylindrische verdichtungsstobe in der nahe des kugelmittelpunktes bzw. der zylinderachse. *Luftfahrtforschung*, (19), 1942.

[72] R. Betti, K. Anderson, V. N. Goncharov, R. L. McCrory, D. D. Meyerhofer, S. Skupsky, and R. P.J. Town. Deceleration phase of inertial confinement fusion implosions. *Physics of Plasmas*, 9(5):2277–2286, 2002.

[73] Charles Cerjan, Paul T. Springer, and Scott M. Sepke. Integrated diagnostic analysis of inertial confinement fusion capsule performance. *Physics of Plasmas*, 20(5), 2013.

[74] P. K. Patel, P. T. Springer, C. R. Weber, L. C. Jarrott, O. A. Hurricane, B. Bachmann, K. L. Baker, L. F. Berzak Hopkins, D. A. Callahan, D. T. Casey, C. J. Cerjan, D. S. Clark, E. L. Dewald, L. Divol, T. Döppner, J. E. Field, D. Fittinghoff, J. Gaffney, V. Geppert-Kleinrath, G. P. Grim, E. P. Hartouni, R. Hatarik, D. E. Hinkel, M. Hohenberger, K. Humbird, N. Izumi, O. S. Jones, S. F. Khan, A. L. Kritcher, M. Kruse, O. L. Landen, S. Le Pape, T. Ma, S. A. MacLaren, A. G. MacPhee, L. P. Masse, N. B. Meezan, J. L. Milovich, R. Nora, A. Pak, J. L. Peterson, J. Ralph, H. F. Robey, J. D. Salmonson, V. A. Smalyuk, B. K. Spears, C. A. Thomas, P. L. Volegov, A. Zylstra, and M. J. Edwards. Hotspot conditions achieved in inertial confinement fusion experiments on the National Ignition Facility. *Physics of Plasmas*, 27(5), 2020.

[75] J. Delettrez, R. Epstein, M. C. Richardson, P. A. Jaanimagi, and B. L. Henke. Effect of laser illumination nonuniformity on the analysis of time-resolved x-ray measurements in uv spherical transport experiments. *Physical Review A*, 36(8):3926–3934, 1987.

[76] P.T Spring, D.J. Fields, B.G. Wilson, J.K. Nash, W.H. Goldstein, C.A. Iglesias, F.J. Rogers, J.K. Swenson, M.H. Chen, A. Bar-Shalo, and R.E. Stewart. Spectroscopic Absorption Measurements of an Iron Plasma. *Physical Review Letters*, 69(26):3735, 1992.

[77] S. J. Rose, P. A.M. Van Hoof, V. Jonauskas, F. P. Keenan, R. Kisielius, C. Ramsbottom, M. E. Foord, R. F. Heeter, and P. T. Springer. Calculation of photoionized plasmas with an average-atom model. *Journal of Physics B: Atomic, Molecular and Optical Physics*, 37(17), 2004.

[78] J. E. Bailey, T. Nagayama, G. P. Loisel, G. A. Rochau, C. Blancard, J. Colgan, Ph Cosse, G. Faussurier, C. J. Fontes, F. Gilleron, I. Golovkin, S. B. Hansen, C. A. Iglesias, D. P. Kilcrease, J. J. MacFarlane, R. C. Mancini, S. N. Nahar, C. Orban, J. C. Pain, A. K. Pradhan, M. Sherrill, and B. G. Wilson. A higher-than-predicted measurement of iron opacity at solar interior temperatures. *Nature*, 517(7532):56–59, 2015.

[79] A. Krygier, G. E. Kemp, F. Coppari, D. B. Thorn, D. Bradley, A. Do, J. H. Eggert, W. Hsing, S. F. Khan, C. Krauland, O. L. Landen, M. J. Macdonald, J. M. McNaney, H. S. Park, B. A. Remington, M. Rubery, M. B. Schneider, H. Sio, and Y. Ping. Optimized continuum x-ray emission from laser-generated plasma. *Applied Physics Letters*, 117(25), 2020.

[80] Stefano Atzeni and JÃijrgen Meyer-Ter-Vehn. *The physics of inertial fusion: beam plasma interaction, hydrodynamics, hot dense matter*. Internat. Mono. Phys. Clarendon Press, Oxford, 2004.

[81] Jeff Colvin and Jon Larsen. *Extreme Physics: Properties and Behavior of Matter at Extreme Conditions*. Cambridge University Press, 2013.

[82] Dimitri Mihalas. *Stellar Atmospheres*. W. H. Freeman, San Francisco, CA, 1978.

[83] J. Colgan, D. P. Kilcrease, N. H. Magee, M. E. Sherrill, J. Abdallah Jr., P. Hakel, C. J. Fontes, J. A. Guzik, and K. A. Mussack. a New Generation of Los Alamos Opacity Tables. *The Astrophysical Journal*, 817(2):116, 2016.

[84] H. S. Bosch and G. M. Hale. Improved formulas for fusion cross-sections and thermal reactivities. *Nuclear Fusion*, 32(4):611–631, 1992.

[85] L. Ballabio, G. Gorini, and J. Kallne. Energy spectrum of thermonuclear neutrons. *Review of Scientific Instruments*, 68(1):585–588, 1997.

[86] L. Ballabio, J. Källne, and G. Gorini. Relativistic calculation of fusion product spectra for thermonuclear plasmas. *Nuclear Fusion*, 38(11):1723–1735, 1998.

[87] V. Yu Glebov, T. C. Sangster, C. Stoeckl, J. P. Knauer, W. Theobald, K. L. Marshall, M. J. Shoup, T. Buczek, M. Cruz, T. Duffy, M. Romanofsky, M. Fox, A. Pruyne, M. J. Moran, R. A. Lerche, J. McNaney, J. D. Kilkenny, M. J. Eckart, D. Schneider, D. Munro, W. Stoeffl, R. Zacharias, J. J. Haslam, T. Clancy, M. Yeoman, D. Warwas, C. J. Horsfield, J. L. Bourgade, O. Landoas, L. Disdier, G. A. Chandler, and R. J. Leeper. The National Ignition Facility neutron time-of-flight system and its initial performance (invited). *Review of Scientific Instruments*, 81(10), 2010.

[88] P. KIRKPATRICK and A. V. BAEZ. Formation of optical images by X-rays. *Journal of the Optical Society of America*, 38(9):766–774, 1948.

[89] Jeffrey A. Koch, Otto L. Landen, Troy W. Barbee, Peter Celliers, Luiz B. Da Silva, Sharon G. Glendinning, Bruce A. Hammel, Dan H. Kalantar, Charles Brown, John Seely, Guy R. Bennett, and Warren Hsing. High-energy x-ray microscopy techniques for laser-fusion plasma research at the National Ignition Facility. *Applied Optics*, 37(10):1784, 1998.

[90] Benjamin Bachmann, T Hilsabeck Ga, J Field, A Macphee, N Masters, C Reed Ga, and T Pardini. on the NIF. 2015.

[91] Paul A. Jaanimagi, Robert Boni, D. Butler, S. Ghosh, William R. Donaldson, and Robert L. Keck. The streak camera development program at LLE. *26th International Congress on High-Speed Photography and Photonics*, 5580:408, 2005.

[92] R. A. Lerche, D. W. Phillion, and G. L. Tietbohl. 25 ps neutron detector for measuring ICF-target burn history. *Review of Scientific Instruments*, 66(1):933–935, 1995.

[93] J. A. Frenje, C. K. Li, F. H. Séguin, J. Deciantis, S. Kurebayashi, J. R. Rygg, R. D. Petrasso, J. Delettrez, V. Yu Glebov, C. Stoeckl, F. J. Marshall, D. D. Meyerhofer, T. C. Sangster, V. A. Smalyuk, and J. M. Soures. Measuring shock-bang timing and ρR evolution of D3He implosions at OMEGA. *Physics of Plasmas*, 11(5 PART 2):2798–2805, 2004.

[94] C. Stoeckl, V. Yu Glebov, S. Roberts, T. C. Sangster, R. A. Lerche, R. L. Griffith, and C. Sorce. Ten-inch manipulator-based neutron temporal diagnostic for cryogenic experiments on OMEGA. *Review of Scientific Instruments*, 74(3 II):1713–1716, 2003.

[95] H. Sio, J. A. Frenje, J. Katz, C. Stoeckl, D. Weiner, M. Bedzyk, V. Glebov, C. Sorce, M. Gatu Johnson, H. G. Rinderknecht, A. B. Zylstra, T. C. Sangster, S. P. Regan, T. Kwan, A. Le, A. N. Simakov, W. T. Taitano, L. Chacòn, B. Keenan, R. Shah, G. Sutcliffe, and R. D. Petrasso. A Particle X-ray Temporal Diagnostic (PXTD) for studies of kinetic, multi-ion effects, and ion-electron equilibration rates in Inertial Confinement Fusion plasmas at OMEGA (invited). *Review of Scientific Instruments*, 87(11), 2016.

[96] V. Yu Glebov, C. Stoeckl, T. C. Sangster, S. Roberts, G. J. Schmid, R. A. Lerche, and M. J. Moran. Prototypes of national ignition facility neutron time-of-flight detectors tested on OMEGA. *Review of Scientific Instruments*, 75(10 II):3559–3562, 2004.

[97] W.L. Bragg. The Analysis of Crystals by the X-ray Spectrometer. *Proceedings of the Royal Society A*, 89(November):767–788, 1914.

[98] A. A. Solodov, B. Yaakobi, D. H. Edgell, R. K. Follett, J. F. Myatt, C. Sorce, and D. H. Froula. Measurements of hot-electron temperature in laser-irradiated plasmas. *Physics of Plasmas*, 23(10), 2016.

[99] T. Ma, N. Izumi, R. Tommasini, D. K. Bradley, P. Bell, C. J. Cerjan, S. Dixit, T. Döppner, O. Jones, J. L. Kline, G. Kyrala, O. L. Landen, S. Lepape, A. J. MacKinnon, H. S. Park, P. K. Patel, R. R. Prasad, J. Ralph, S. P. Regan, V. A. Smalyuk, P. T. Springer, L. Suter, R. P.J. Town, S. V. Weber, and S. H. Glenzer. Imaging of high-energy x-ray emission from cryogenic thermonuclear fuel implosions on the NIF. *Review of Scientific Instruments*, 83(10), 2012.

[100] L. R. Benedetti, J. P. Holder, M. Perkins, C. G. Brown, C. S. Anderson, F. V. Allen, R. B. Petre, D. Hargrove, S. M. Glenn, N. Simanovskaia, D. K. Bradley, and P. Bell. Advances in X-ray framing cameras at the National Ignition Facility to improve quantitative precision in X-ray imaging. *Review of Scientific Instruments*, 87(2), 2016.

[101] Terrance J. Kessler, Ying Lin, J. Joseph Armstrong, and Belimar Velazquez. <title>Phase conversion of lasers with low-loss distributed phase plates</title>. *Laser Coherence Control: Technology and Applications*, 1870(May 1993):95–104, 1993.

[102] BI Bennett, JD Johnson, GI Kerley, and GT Rood. Sesame: the Los Alamos National Laboratory equation of state database. *Los Alamos National Laboratory, Los Alamos, NM, LA- . . .*, page 43, 1992.

[103] Aki Vehtari, Andrew Gelman, and Jonah Gabry. Practical Bayesian model evaluation using leave-one-out cross-validation and WAIC. *Statistics and Computing*, 27(5):1413–1432, 2017.

[104] H. Jeffreys. Oxford, England.

[105] David J. Spiegelhalter, Nicola G. Best, Bradley P. Carlin, and Angelika Van Der Linde. Bayesian measures of model complexity and fit. *Journal of the Royal Statistical Society. Series B: Statistical Methodology*, 64(4):583–616, 2002.

[106] D. E. Fratanduono, R. F. Smith, D. G. Braun, J. R. Patterson, R. G. Kraus, T. S. Perry, A. Arsenlis, G. W. Collins, and J. H. Eggert. The effect of nearly steady shock waves in ramp compression experiments. *Journal of Applied Physics*, 117(24), 2015.

[107] R. Nora, W. Theobald, R. Betti, F. J. Marshall, D. T. Michel, W. Seka, B. Yaakobi, M. Lafon, C. Stoeckl, J. Delettrez, A. A. Solodov, A. Casner, C. Reverdin, X. Ribeyre, A. Vallet, J. Peebles, F. N. Beg, and M. S. Wei. Gigabar spherical shock generation on the OMEGA laser. *Physical Review Letters*, 114(4):1–5, 2015.

[108] S. X. Hu. Continuum Lowering and Fermi-Surface Rising in Strongly Coupled and Degenerate Plasmas. *Physical Review Letters*, 119(6):1–6, 2017.

[109] S. Le Pape, L. F. Berzak Hopkins, L. Divol, A. Pak, E. L. Dewald, S. Bhandarkar, L. R. Bennedetti, T. Bunn, J. Biener, J. Crippen, D. Casey, D. Edgell, D. N. Fittinghoff, M. Gatu-Johnson, C. Goyon, S. Haan, R. Hatarik, M. Havre, D. D.M. Ho, N. Izumi, J. Jaquez, S. F. Khan, G. A. Kyrala, T. Ma, A. J. Mackinnon, A. G. Macphee, B. J. Macgowan, N. B. Meezan, J. Milovich, M. Millot, P. Michel, S. R. Nagel, A. Nikroo, P. Patel, J. Ralph, J. S. Ross, N. G. Rice, D. Strozzi, M. Stadermann, P. Volegov, C. Yeamans, C. Weber, C. Wild, D. Callahan, and O. A. Hurricane. Fusion Energy Output Greater than the Kinetic Energy of an Imploding Shell at the National Ignition Facility. *Physical Review Letters*, 120(24), 2018.

[110] D. G. Hicks, N. B. Meezan, E. L. Dewald, A. J. MacKinnon, R. E. Olson, D. A. Callahan, T. Döppner, L. R. Benedetti, D. K. Bradley, P. M. Celliers, D. S. Clark, P. Di Nicola, S. N. Dixit, E. G. Dzenitis, J. E. Eggert, D. R. Farley, J. A. Frenje, S. M. Glenn, S. H. Glenzer, A. V. Hamza, R. F. Heeter,

J. P. Holder, N. Izumi, D. H. Kalantar, S. F. Khan, J. L. Kline, J. J. Kroll, G. A. Kyrala, T. Ma, A. G. MacPhee, J. M. McNaney, J. D. Moody, M. J. Moran, B. R. Nathan, A. Nikroo, Y. P. Opachich, R. D. Petrasso, R. R. Prasad, J. E. Ralph, H. F. Robey, H. G. Rinderknecht, J. R. Rygg, J. D. Salmonson, M. B. Schneider, N. Simanovskaia, B. K. Spears, R. Tommasini, K. Widmann, A. B. Zylstra, G. W. Collins, O. L. Landen, J. D. Kilkenny, W. W. Hsing, B. J. MacGowan, L. J. Atherton, and M. J. Edwards. Implosion dynamics measurements at the National Ignition Facility. *Physics of Plasmas*, 19(12), 2012.

[111] V. N. Goncharov, T. C. Sangster, R. Betti, T. R. Boehly, M. J. Bonino, T. J.B. Collins, R. S. Craxton, J. A. Delettrez, D. H. Edgell, R. Epstein, R. K. Follett, C. J. Forrest, D. H. Froula, V. Yu. Glebov, D. R. Harding, R. J. Henchen, S. X. Hu, I. V. Igumenshchev, R. Janezic, J. H. Kelly, T. J. Kessler, T. Z. Kosc, S. J. Loucks, J. A. Marozas, F. J. Marshall, A. V. Maximov, R. L. McCrory, P. W. McKenty, D. D. Meyerhofer, D. T. Michel, J. F. Myatt, R. Nora, P. B. Radha, S. P. Regan, W. Seka, W. T. Shmayda, R. W. Short, A. Shvydky, S. Skupsky, C. Stoeckl, B. Yaakobi, J. A. Frenje, M. Gatu-Johnson, R. D. Petrasso, and D. T. Casey. Improving the hot-spot pressure and demonstrating ignition hydrodynamic equivalence in cryogenic deuterium-tritium implosions on OMEGA. *Physics of Plasmas*, 21(5), 2014.

[112] J. R. Rygg, O. S. Jones, J. E. Field, M. A. Barrios, L. R. Benedetti, G. W. Collins, D. C. Eder, M. J. Edwards, J. L. Kline, J. J. Kroll, O. L. Landen, T. Ma, A. Pak, J. L. Peterson, K. Raman, R. P.J. Town, and D. K. Bradley. 2D X-ray radiography of imploding capsules at the national ignition facility. *Physical Review Letters*, 112(19):1–5, 2014.

[113] J. A. Gaffney, D. Clark, V. Sonnad, and S. B. Libby. Development of a Bayesian method for the analysis of inertial confinement fusion experiments on the NIF. *Nuclear Fusion*, 53(7), 2013.

[114] Zs Jenei, E. F. O'Bannon, S. T. Weir, H. Cynn, M. J. Lipp, and W. J. Evans. Single crystal toroidal diamond anvils for high pressure experiments beyond 5 megabar. *Nature Communications*, 9(1):1–6, 2018.

[115] John N. Bahcall, Aldo M. Serenelli, and Sarbani Basu. New Solar Opacities, Abundances, Helioseismology, and Neutrino Fluxes. *The Astrophysical Journal*, 621(1):L85–L88, 2005.

[116] O. A. Hurricane, D. A. Callahan, D. T. Casey, P. M. Celliers, C. Cerjan, E. L. Dewald, T. R. Dittrich, T. Döppner, D. E. Hinkel, L. F.Berzak Hopkins, J. L. Kline, S. Le Pape, T. Ma, A. G. Macphee, J. L. Milovich, A. Pak, H. S. Park, P. K. Patel, B. A. Remington, J. D. Salmonson, P. T. Springer, and R. Tommasini. Fuel gain exceeding unity in an inertially confined fusion implosion. *Nature*, 506(7488):343–347, 2014.

[117] D. T. Casey, D. B. Sayre, C. R. Brune, V. A. Smalyuk, C. R. Weber, R. E. Tipton, J. E. Pino, G. P. Grim, B. A. Remington, D. Dearborn, L. R. Benedetti, J. A. Frenje, M. Gatu-Johnson, R. Hatarik, N. Izumi, J. M. Mc-Naney, T. Ma, G. A. Kyrala, S. Maclaren, J. Salmonson, S. F. Khan, A. Pak, L. Berzak Hopkins, S. Lepape, B. K. Spears, N. B. Meezan, L. Divol, C. B. Yeamans, J. A. Caggiano, D. P. McNabb, D. M. Holunga, M. Chiarappa-Zucca, T. R. Kohut, and T. G. Parham. Thermonuclear reactions probed at stellar-core conditions with laser-based inertial-confinement fusion. *Nature Physics*, 13(12):1227–1231, 2017.

[118] R. Betti and O. A. Hurricane. Inertial-Confinement fusion with lasers. *Nature Physics*, 12(5):445–448, 2016.

[119] D. S. Clark, D. E. Hinkel, D. C. Eder, O. S. Jones, S. W. Haan, B. A. Hammel, M. M. Marinak, J. L. Milovich, H. F. Robey, L. J. Suter, and R. P.J. Town. Detailed implosion modeling of deuterium-tritium layered experiments on the National Ignition Facility. *Physics of Plasmas*, 20(5), 2013.

[120] P. T. Springer, O. A. Hurricane, J. H. Hammer, R. Betti, D. A. Callahan, E. M. Campbell, D. T. Casey, C. J. Cerjan, D. Cao, E. Dewald, L. Divol, T. Doeppner, M. J. Edwards, J. E. Field, C. Forrest, J. Frenje, J. A. Gaffney, M. Gatu-Johnson, V. Glebov, V. N. Goncharov, G. P. Grim, E. Hartouni, R. Hatarik, D. E. Hinkel, L. Berzak Hopkins, I. Igumenshchev, P. Knapp, J. P. Knauer, A. L. Kritcher, O. Landen, A. Pak, S. Le Pape, T. Ma, A. G. Macphee, D. H. Munro, R. C. Nora, P. K. Patel, L. Peterson, P. B. Radha, S. P. Regan, H. Rinderknecht, C. Sangster, B. K. Spears, and C. Stoeckl. A 3D dynamic model to assess the impacts of low-mode asymmetry, aneurysms and mix-induced radiative loss on capsule performance across inertial confinement fusion platforms. *Nuclear Fusion*, 59(3), 2019.

[121] C. Sorce, J. Schein, F. Weber, K. Widmann, K. Campbell, E. Dewald, R. Turner, O. Landen, K. Jacoby, P. Torres, and D. Pellinen. Soft x-ray power diagnostic improvements at the Omega Laser Facility. *Review of Scientific Instruments*, 77(10), 2006.

[122] S. F. Khan, L. C. Jarrott, P. K. Patel, N. Izumi, T. Ma, A. G. Macphee, B. Hatch, O. L. Landen, J. Heinmiller, J. D. Kilkenny, and D. K. Bradley. Implementing time resolved electron temperature capability at the NIF using a streak camera. *Review of Scientific Instruments*, 89(10), 2018.

[123] J. R. Rygg, J. A. Frenje, C. K. Li, F. H. Séguin, R. D. Petrasso, D. D. Meyerhofer, and C. Stoeckl. Electron-ion thermal equilibration after spherical shock collapse. *Physical Review E - Statistical, Nonlinear, and Soft Matter Physics*, 80(2):1–8, 2009.

[124] H. Brysk. Fusion neutron energies and spectra. *Plasma Physics*, 15(7):611–617, 1973.

[125] David H. Munro. Interpreting inertial fusion neutron spectra. *Nuclear Fusion*, 56(3), 2016.